Fractional Quantum Hall Effect: Non-Abelian Quasiholes and Fractional Chern Insulators

Yangle Wu

A Dissertation
Presented to the Faculty
of Princeton University
in Candidacy for the Degree
of Doctor of Philosophy

Recommended for Acceptance
by the Department of
Physics
Adviser: B. Andrei Bernevig

September 2014

Abstract

This dissertation investigates two aspects of the fractional quantum Hall effect.

First, I study the quasiholes in certain fractional quantum Hall states that are promising candidates for the experimental realization of non-Abelian anyons. I apply the newly developed matrix product state technique to examine these exotic excitations, and determine the correlation lengths associated with the exponential convergence of the braiding statistics. This provides the first microscopic verification for the Fibonacci nature of the $\mathbb{Z}_3$ Read-Rezayi quasiholes. I also present evidence for the failure of plasma screening in the non-unitary Gaffnian wave function.

Second, I discuss the so-called fractional Chern insulators. These strongly-correlated phases are stabilized by repulsive interactions between electrons in a topological Bloch band. They exhibit fractional quantum Hall effect at zero magnetic field, but also display features fundamentally distinct from their continuum counterparts. I will construct model wave functions for these lattice states, and explain their difference from the continuum analogues as a specially crafted set of boundary conditions.

Acknowledgements

First and foremost I would like to thank my advisor Andrei Bernevig for guidance and support. I have benefited enormously from his insatiable curiosity, sharp intuition, and tenacious perseverance. His incredibly high productivity has been my constant source of motivation. And thanks to his generous support and encouragement, I have had great opportunities to interact with many physicists over the world.

I am also greatly indebted to Nicolas Regnault. Working with him on the past five papers has been absolutely amazing. He showed me how to do numerics right, and I cannot possibly thank him enough for his great patience during the countless hours of discussions, and for his tremendous help during my job search and talk preparations.

In the past five years, I have had the unbelievable fortune to learn from many brilliant physicists. I am grateful for the interesting conversations I have had with Dan Arovas, Jérôme Dubail, Liang Fu, Taylor Hughes, Milica Milovanovic, Ganpathy Murthy, Xiao-Liang Qi, Ramamurti Shankar, and Ronny Thomale, among many others. And I want to thank Duncan Haldane, Titus Neupert, YeJe Park, Ying-Hai Wu, and Bo Yang for the illuminating discussions on the fractional quantum Hall effect, and Benoit Estienne, Victor Mikhaylov, Sasha Polyakov, and Grisha Tarnopolsky for patiently answering my naïve questions about conformal field theory. I thank Curtis Callan for his help and interest in my work, and I thank Yi Deng and Joshua Shaevitz for guidance on my experimental project. I would also like to thank my fellow travelers Aris Alexandradinata, Chen Fang, Jian Li, Yi Li, Zhao Liu, and Cécile Repellin for the many refreshing exchanges. Finally, I thank Taylor Hughes for the much needed encouragement last winter.

I am grateful to my host family at Princeton, Jane and Al Vogel, for their hospitality and kindness. And I thank my fellow graduate students for making my life colorful. In particular, I would like to thank Bin Xu, Liangsheng Zhang, and Bo Zhao for the delightful digressions at lunch. And I would like to express my gratitude

to Ilya Belopolski, YeJe Park, and Jun Xiong for the many late-night chats in the lounge.

Lastly, I thank my mother and father for their unconditional love during all these years. To them I dedicate this dissertation.

Publications and presentations associated with this dissertation

Materials from this dissertation have been published in the following papers:

1. Yang-Le Wu, B. Andrei Bernevig, and N. Regnault, "Zoology of fractional Chern insulators", *Physical Review B*, **85**(7):075116, 2012.

2. Yang-Le Wu, N. Regnault, and B. Andrei Bernevig, "Gauge-fixed Wannier wave functions for fractional topological insulators", *Physical Review B*, **86**(8):085129, 2012.

3. Yang-Le Wu, N. Regnault, and B. Andrei Bernevig, "Bloch model wave functions and pseudopotentials for all fractional Chern insulators", *Physical Review Letters*, **110**(10):106802, 2013.

4. Yang-Le Wu, N. Regnault, and B. Andrei Bernevig, "Haldane statistics for fractional Chern insulators with an arbitrary Chern number", *Physical Review B*, **89**(15):155113, 2014.

5. Yang-Le Wu, B. Estienne, N. Regnault, and B. Andrei Bernevig, "Braiding non-Abelian quasiholes in fractional quantum Hall states", arXiv:1405.1720, 2014.

Materials from this dissertation have been presented at the following conferences:

1. American Physical Society March Meeting 2012, Boston, Massachusetts.

2. American Physical Society March Meeting 2013, Baltimore, Maryland.

3. American Physical Society March Meeting 2014, Denver, Colorado.

Contents

Chapter 1

Introduction

Fractional quantum Hall effect [92] is the prototype system for the emergence of topological order in condensed matter. It features an extremely rich interplay between nontrivial topology and strong correlations. Despite thirty years of intense research, this model system is still of immense interest. In this dissertation, we present two recent developments. First, we provide a microscopic characterization of the non-Abelian nature of quasiholes in certain exotic quantum Hall states. Second, we examine the fractionalized phases of interacting electrons in a partially filled topological flat band.

1.1 Non-Abelian quasiholes

Non-Abelian anyons [63] are among the most striking manifestations of topological order. They are localized quasiparticles with two defining properties. First, multiple non-Abelian anyons at fixed positions span a quasi-degenerate Hilbert space, and this quasi-degeneracy is stable against local perturbations. Second, braiding quasiparticles implements unitary transformations over the degenerate Hilbert space. These transformations depends only on the topology of the braids rather than the actual trajectories, and different braiding matrices do not commute. This makes it pos-

sible to construct topologically fault-tolerant quantum computers from these exotic excitations [47].

In this context, of particular importance are the Fibonacci anyons. They provide a representation of the braiding group rich enough to carry out universal quantum computations [30, 31, 44], which cannot be achieved with simpler non-Abelian anyons such as the Majorana fermions. It has long been conjectured that the quasiholes in the $\mathbb{Z}_3$ Read-Rezayi state [73], which may describe the filling $\nu = 12/5$ fractional quantum Hall plateau [103], are Fibonacci anyons when sufficiently separated. However, this conjecture has not been supported by any microscopic evidence, due to the sheer complexity of the $\mathbb{Z}_3$ Read-Rezayi quasihole wave functions. In fact, beyond the conjectured universal topological properties, very little is known about these elusive excitations.

In Chapter 2 of this thesis, we settle this long-standing problem and explicitly demonstrate the Fibonacci nature of the $\mathbb{Z}_3$ Read-Rezayi quasiholes. Through a numerical study of the model wave functions, we establish the exponential convergence of the braiding matrices with increasing quasihole separations, and we extract the associated length scales as well as the quasihole radii. This puts an upper bound on the desirable quasihole density in interferometer devices: at a higher density, the $\mathbb{Z}_3$ Read-Rezayi quasiholes exhibit clear non-universal deviations from the Fibonacci anyons.

In addition, we also provide a microscopic diagnosis for the pathology of the Gaffnian wave function [81], which is conjectured not to give rise to sensible braiding statistics due to its root in non-unitary conformal field theories [72]. We explicitly demonstrate that the non-universal, path-dependent contributions to the braiding matrices follow a power-law rather than exponential decay when quasihole separations increase. This signals the failure of plasma screening and highlights the gapless nature of the Gaffnian. Our results largely rule out the possibility of salvaging this

pathological wave function as the description of a gapped phase with topological order.

The above progress is enabled by the recent development [24, 107, 26, 27] of the exact matrix product states [29, 78] for fractional quantum Hall effect. Essentially, the matrix product state is a tensor factorization of the many-body wave function. This factorization makes it possible to exploit the entanglement area law [25] and to store quantum information compactly, and it also greatly facilitates the calculation of physical observables.

1.2 Fractional Chern insulators

The fractional quantum Hall effect was originally discovered in two-dimensional electron gas subject to a strong perpendicular magnetic field [92, 52]. Recently, it was demonstrated numerically that these strongly-correlated phases also exist in a partially filled topological band, even in the absence of a magnetic field. Chapters 3 to 5 of this thesis are devoted to the study of these so-called fractional Chern insulators.

The Chern insulator [40] is the first and simplest example of a topological insulator. It is defined by a non-zero Chern number of the occupied bands. It exhibits an integer Hall conductance similar to the integer quantum Hall effect, but at zero overall magnetic field. Recent developments have shown that strong electronic interactions open up interesting new possibilities [80, 65, 74].

In Chapter 3, using exact diagonalization, we demonstrate numerically the existence of fractionalized phases in an array of Chern insulator lattice models with Chern number $C = 1$. These phases include the zero-magnetic-field counterparts of both Abelian and non-Abelian quantum Hall states. We identify them from finite-size numerics using a combination of probes in the energy and the entanglement spectra.

We also find a correlation between the stability of the strongly-correlated phase and the uniformity of the Berry curvature in the band structure.

In Chapter 4, we construct many-body trial wave functions for the fractionalized phases of a partially filled $C = 1$ band, by transcribing quantum Hall states on a continuum torus to the lattice. This is achieved through a one-body mapping between the Landau orbitals in the continuum Landau level and the localized hybrid Wannier orbitals in a $C = 1$ Chern band [71]. We pinpoint a previously overlooked gauge freedom in this mapping, and provide an explicit prescription for gauge fixing. We find that the exact ground states at $\nu = 1/3$ filling of the fractional Chern insulators studied in Chapter 3 are well captured by the lattice states constructed from the Laughlin wave function.

The discussion so far has been limited to a topological band with Chern number $C = 1$, which is essentially the same as the continuum fractional quantum Hall effect in a periodic potential [50]. The strongly-correlated physics in a $C > 1$ Chern band [90, 104, 95] turned out to be much richer than the conventional fractional quantum Hall effect, due to the interplay between topological order and lattice structure [7, 55, 84]. Barkeshli and Qi [7] mapped a $C > 1$ Chern band to a C-component lowest Landau level using hybrid Wannier states [71], and suggested the possibility to realize multicomponent FQH states in a single Chern band. Numerical studies [95, 55, 84, 36] indeed found clear signature of such states, including the color SU(C) version of the Halperin [41] and the non-Abelian spin-singlet states [4], but also identified qualitative deviations from these states, [84, 55] implying a more complex structure than proposed in Ref. [7].

In Chapter 5, we argue that these new features can be understood as the consequences of a special set of boundary conditions associated with the mapping to the lowest Landau level. In the simplest case, this alternative boundary condition can be understood as a color-dependent magnetic flux insertion. We demonstrated

that the multicomponent Landau level in a new Bloch basis can be seen as a single manifold with constant Berry curvature and Chern number C. Using pseudopotential Hamiltonians, we constructed model states for fractional Chern insulators with an arbitrary Chern number, and found high overlaps with the exact ground states. Crucially, our model states correctly capture the anomalous features in the particle entanglement spectrum of the $C > 1$ fractional Chern insulators. This makes our states distinct from the conventional multicomponent fractional quantum Hall states. Finally, we analyze the thin-torus limit of the pseudopotential Hamiltonians, and extract counting rules for the degeneracy of its zero modes in each Bloch momentum sector.

Chapter 2

Braiding non-Abelian quasiholes

Non-Abelian anyons have been the focus of much theoretical and experimental interest due to the exciting prospect of topologically fault-tolerant quantum computing [47, 30, 31, 44, 63]. As noted by Kitaev [47], the topological degeneracy of these exotic excitations allows non-local storage of quantum information, while adiabatic braiding implements unitary quantum gates.

Candidates [22, 85, 19] for their physical realization are the quasiholes in certain fractional quantum Hall states [92], in particular, those around the plateaus at fillings $\nu = 5/2$ and $12/5$ [97, 66, 103]. Their model wave functions, namely the Moore-Read [60] (MR) and the $\mathbb{Z}_3$ Read-Rezayi [73] (RR) states, enjoy an elegant first-quantized rewriting [32, 60] in terms of conformal field theory [8, 61, 23] (CFT) correlators, from which many physical properties can be predicted. The strengths of this approach rest on a crucial *conjecture* [60]: quasihole braiding statistics can be directly read off from the monodromy of the CFT correlators. Under this conjecture, the MR quasiholes are Ising anyons, while the $\mathbb{Z}_3$ RR ones are Fibonacci anyons. But the proof of the conjecture itself is lacking.

The relation between statistics and monodromy was originally established for the Laughlin state [52] through the plasma analogy [5]. Assuming sufficient quasihole

separations, the statistics-monodromy equivalence holds true when the plasma is in the screening phase. With considerable effort, this line of argument was recently extended to the MR state [37, 72, 18], in agreement with finite-size numerics [91, 70, 6]. More complicated states like the $\mathbb{Z}_3$ RR still remain uncharted territory for both analytics and numerics, despite their capacity for universal quantum computation [30, 31, 44]. Moreover, wave functions constructed from non-unitary field theories (such as the Gaffnian [81]) are conjectured not to give rise to sensible statistics [72], yet the microscopic symptom of such pathology is still far from clear.

In this chapter, we aim to settle the aforementioned issues through numerical studies of model wave functions [98]. Until very recently, this was a daunting task due to the exponentially large Hilbert space, and in many cases, the absence of a convenient analytical form of the quasihole wave functions. In fact, so far only the Laughlin and the MR quasiholes have been tested directly, with various degrees of success, using exact diagonalization and Monte Carlo techniques [91, 70, 6]. A similar check on the Gaffnian and the $\mathbb{Z}_3$ RR states proves extremely challenging due to the combinatorial complexity of their analytical expressions. These difficulties are partially solved by the recent development [24, 107, 26, 27] of exact matrix product states [29, 78] (MPS) for the CFT-derived wave functions [32, 60]. The MPS formalism provides a faithful and efficient representation of quantum Hall model states, and greatly facilitates the calculation of physical observables. We generalize this novel technique to non-Abelian quasiholes.

2.1 Conformal correlators as matrix product states

Before discussing the physical results, we first set the stage for the construction of the quantum Hall matrix product states (MPS). The discussion in this section is partly based on Refs. [24, 107, 26, 27].

We consider model wave functions in the lowest Landau level constructed from chiral conformal correlators [32, 60]. In the field correlation function, an electron at position z is represented by an insertion $\mathcal{V}(z)$ in the tensor product form

$$\mathcal{V}(z) = \psi(z) \otimes :e^{i\sqrt{q}\phi(z)}: . \tag{2.1}$$

Here, ψ is a primary field in the so-called neutral CFT, whereas the normal-ordered $:e^{i\sqrt{q}\phi}:$ is a vertex operator associated with a free boson field ϕ, with $q = 1/\nu$ being the inverse filling fraction. Then, the conformal correlator

$$\langle\langle \mathcal{V}(z_1)\mathcal{V}(z_2)\cdots\mathcal{V}(z_n)\rangle\rangle \tag{2.2}$$

can be viewed as a many-body wave function $\Psi(z_1, z_2, \ldots, z_n)$. Here and hereafter, the double brackets denote correlators in the tensor-product CFT, in contrast to the states of physical electrons.

We work on a cylinder geometry with finite perimeter L_y.[1] The complex coordinate $z = x + iy$ has x running along the cylinder axis and y running around the cylinder perimeter. To reduce clutter, in this section we adopt the unit system where the magnetic length $\ell_0 = 1$. For later convenience, we define the inverse radius γ

$$\gamma = \frac{2\pi}{L_y}. \tag{2.3}$$

[1] Due to the entanglement area law, this choice is more preferable to the disk or the sphere geometry.

The many-body wave function $\Psi(z_1, z_2, \ldots, z_n)$ is given by the conformal correlator in Eq. (2.2) evaluated on the cylinder geometry, which can be "exploded" into the usual planar geometry using the conformal transformation $z \to e^{\gamma z}$.

2.1.1 Background charge and gauge choice

The MPS is a tensor factorization of the second-quantized amplitudes of the many-body wave function $\Psi(z_1, z_2, \ldots, z_N)$. The first step is thus to obtain Ψ in the occupation-number basis. We pick the Landau gauge for the magnetic field, and work with the Landau orbitals labeled by the wave number $j \in \mathbb{Z}$:

$$\psi_j(x, y) = \frac{1}{(\sqrt{\pi} L_y)^{\frac{1}{2}}} e^{i\gamma j y} e^{-\frac{1}{2}(x-\gamma j)^2} = \frac{e^{-\frac{1}{2}\gamma^2 j^2}}{(\sqrt{\pi} L_y)^{\frac{1}{2}}} e^{i\gamma j z} e^{-\frac{1}{2}x^2}. \tag{2.4}$$

These one-body orbitals take the form of a holomorphic function in z times a Gaussian in x. Due to the chirality of the electron operators $\mathcal{V}(z)$, the conformal correlator in Eq. (2.2) does not have the (non-holomorphic) Gaussian factor, and thus does not yet qualify as a many-body wave function in the lowest Landau level. Fortunately, the Gaussian factor can be generated naturally by spreading the neutralizing background charge for the boson field ϕ *uniformly* [60] on the cylinder. This amounts to inserting another (non-primary) operator $:e^{-i\frac{1}{2\pi\sqrt{q}}\int \mathrm{d}^2 z\, \phi(z)}:$ into the conformal correlator, representing the background charge. Here, the normal ordering removes self interactions between background charges at different locations. However, as discussed in Ref. [60], this extra insertion has a side effect: in addition to the desirable Gaussian factor, it also introduces a non-holomorphic gauge factor. Taken altogether, the cylinder many-body wave function in the Landau gauge is given by

$$\Psi(z_1, z_2, \ldots, z_n) = e^{i\sum_i x_i y_i} \left\langle\!\!\left\langle \mathcal{V}(z_1) \cdots \mathcal{V}(z_n) :e^{-i\frac{1}{2\pi\sqrt{q}}\int \mathrm{d}^2 z\, \phi(z)}: \right\rangle\!\!\right\rangle, \tag{2.5}$$

with $z_i = x_i + i y_i$.

2.1.2 Occupation-number basis

We now try to expand the above wave function in the occupation-number basis. Since each Landau orbital is a momentum eigenstate, we can extract the second-quantized amplitudes through a Fourier transform in the y direction. Notice that the one-body wave function ψ_j reduces to a simple plane wave along the orbital center $x = \gamma j$,

$$\psi_j(\gamma j, y) = \frac{1}{(\sqrt{\pi} L_y)^{\frac{1}{2}}} e^{i\gamma j y}. \tag{2.6}$$

To take advantage of this, we follow Ref. [107] and place the Fourier integration contours along the orbital centers. Then, we can express the amplitude associated with occupied orbitals $\{j_1, j_2, \cdots, j_n\}$ as

$$\begin{aligned} \Psi_{j_1,j_2,\ldots,j_n} &= \prod_i \int_0^{L_y} \frac{\mathrm{d}y_i}{L_y} \, e^{-i\gamma j_i y_i} \, \Psi(\gamma j_1 + i y_1, \ldots, \gamma j_n + i y_n) \\ &= \prod_i \int_0^{L_y} \frac{\mathrm{d}y_i}{L_y} \left\langle\!\!\left\langle \mathcal{V}(\gamma j_1 + i y_1) \cdots \mathcal{V}(\gamma j_n + i y_n) \, {:}e^{-i\frac{1}{2\pi\sqrt{q}} \int \mathrm{d}^2 z \, \phi(z)}{:} \right\rangle\!\!\right\rangle, \end{aligned} \tag{2.7}$$

up to a constant normalization factor. Notice that at $x_i = \gamma j_i$, the gauge transformation $e^{i x_i y_i}$ in Eq. (2.5) cancels the Fourier factor $e^{-i\gamma j_i y_i}$.

The next step is to rewrite the above expression in terms of the occupation numbers $m_j = 0, 1$ of each Landau orbital j. We work in the operator formalism of the CFT, and interpret the x direction along the cylinder axis as the imaginary time and the perpendicular y direction as the space direction. For simplicity, we first consider only the electron operators, and postpone the treatment of the background charge operator. We are free to pick the index ordering of the occupied orbitals. Choosing $j_1 > j_2 > \cdots > j_n$ ensures the time-ordering of electron operators and allows us to convert the correlator into an operator expression

$$\langle\!\langle \mathcal{V}(\gamma j_1 + i y_1) \cdots \mathcal{V}(\gamma j_n + i y_n) \rangle\!\rangle = \langle\!\langle \mathrm{out} | \hat{\mathcal{V}}(\gamma j_1 + i y_1) \cdots \hat{\mathcal{V}}(\gamma j_n + i y_n) | \mathrm{in} \rangle\!\rangle. \tag{2.8}$$

On the right-hand side, the over-hats highlight the operator nature of the insertions, and the choice of the in- and the out-states will be discussed later.

Thanks to the conformal invariance, the x-dependence of the primary field insertion $\mathcal{V}(x+iy)$ can be extracted as an imaginary-time evolution,

$$\hat{\mathcal{V}}(x+iy) = e^{x\gamma\hat{L}_0}\hat{\mathcal{V}}(iy)e^{-x\gamma\hat{L}_0}. \tag{2.9}$$

Here, the $\hat{L}_0$ operator is the Virasoro generator for dilations, and $\gamma\hat{L}_0$ serves as the CFT Hamiltonian on the cylinder. We define the zero-mode of the electron operator

$$\hat{\mathcal{V}}_0 = \int_0^{L_y} \frac{\mathrm{d}y}{L_y}\,\hat{\mathcal{V}}(iy). \tag{2.10}$$

Without worrying about the background charge for now, we can now rewrite Eq. (2.7) as

$$\langle\langle \mathrm{out}|\,\hat{\mathcal{V}}_0\, e^{-(j_1-j_2)\gamma^2\hat{L}_0}\,\hat{\mathcal{V}}_0\, e^{-(j_2-j_3)\gamma^2\hat{L}_0}\cdots e^{-(j_{n-1}-j_n)\gamma^2\hat{L}_0}\,\hat{\mathcal{V}}_0\,|\mathrm{in}\rangle\rangle, \tag{2.11}$$

up to factors that depend only on the energy of the in- and the out-state boundaries. The above expression is an imaginary time evolution along the cylinder axis, punctured by the electron zero-mode operators at the center of each occupied orbital. To assign the time evolution to individual orbitals, we define $\hat{U}_\delta = e^{-\gamma\hat{L}_0\delta}$, which advances in imaginary time any state in the conformal Hilbert space at a given time slice by δ along the cylinder. Finally, we can write the second-quantized amplitude $\Psi_{\{m\}}$ associated with the occupation numbers $\{m\} \equiv [m_0, m_1, m_2, \ldots]$ of the Landau orbitals as

$$\Psi_{\{m\}} \equiv \langle\{m\}|\Psi\rangle = \langle\langle \mathrm{out}|\cdots\hat{B}^{m_2}\hat{B}^{m_1}\hat{B}^{m_0}|\mathrm{in}\rangle\rangle, \tag{2.12}$$

with the $\hat{B}^m$ operators given by

$$\hat{B}^0 = \hat{U}_\gamma, \quad \hat{B}^1 = \hat{U}_\gamma\,\hat{\mathcal{V}}_0. \tag{2.13}$$

2.1.3 Cylinder evolution operator

We now go back to the issue of the uniform background charge. We would like to treat it in the same way as the electron operator. To this end, we first split the

two-dimensional integral into small patches,

$$:e^{-i\frac{1}{2\pi\sqrt{q}}\int \mathrm{d}x\mathrm{d}y\,\hat{\phi}(x+iy)}: \sim \prod_{x,y} :e^{-i\frac{1}{2\pi\sqrt{q}}\mathrm{d}x\mathrm{d}y\,\hat{\phi}(x+iy)}:, \tag{2.14}$$

where the product over patches (x, y) is time ordered, and $q = 1/\nu$ is the inverse filling fraction. Evidently this operation introduces unwanted self interactions between background charges at different locations. Fortunately, this only leads to an overall constant factor that does not depend on the electron position. Notice that each factor $:e^{-i\frac{1}{2\pi\sqrt{q}}\mathrm{d}x\mathrm{d}y\,\hat{\phi}(x+iy)}:$ is now a primary field, for which Eq. (2.9) applies:

$$:e^{-i\frac{1}{2\pi\sqrt{q}}\mathrm{d}x\mathrm{d}y\,\hat{\phi}(x+iy)}: = e^{x\gamma\hat{L}_0}\,:e^{-i\frac{1}{2\pi\sqrt{q}}\mathrm{d}x\mathrm{d}y\,\hat{\phi}(iy)}:\,e^{-x\gamma\hat{L}_0}. \tag{2.15}$$

Thanks to the time ordering, we can recombine the patches at the same x, leading to

$$:e^{-i\frac{1}{2\pi\sqrt{q}}\int \mathrm{d}x\mathrm{d}y\,\hat{\phi}(x+iy)}: \sim \prod_{x} e^{x\gamma\hat{L}_0}e^{-i\frac{1}{\sqrt{q}}\frac{\mathrm{d}x}{\gamma}\,\hat{\phi}_0}e^{-x\gamma\hat{L}_0}, \tag{2.16}$$

where the product over time slices x is still time ordered, and the zero-mode $\hat{\phi}_0$ of the boson field is defined by

$$\hat{\phi}_0 = \int_0^{L_y} \frac{\mathrm{d}y}{L_y}\hat{\phi}(iy). \tag{2.17}$$

Therefore, up to an inconsequential overall constant, the uniform background charge operator amounts to adding an exponentiated boson zero-mode insertion at each time slice. We can combine this with the time evolution, and redefine $\hat{U}_\delta$ as the path-ordered exponential

$$\hat{U}_\delta = \mathcal{P}\exp\left[-\int_0^\delta \mathrm{d}x\left(\gamma\hat{L}_0 + i\frac{1}{\gamma\sqrt{q}}\hat{\phi}_0\right)\right]. \tag{2.18}$$

This modification is enough to capture the effect of the uniform background charge operator, up to an overall constant. The path-ordered exponential can be further simplified as

$$\hat{U}_\delta = \exp\left(-i\frac{\delta}{\gamma\sqrt{q}}\,\hat{\phi}_0\right)\exp\left(-\delta\gamma\hat{L}_0\right)\exp\left[-\frac{1}{2}\delta\gamma\left(\hat{a}_0^2 + \frac{\delta}{\gamma\sqrt{q}}\hat{a}_0 + \frac{\delta^2}{3\gamma^2 q}\right)\right], \tag{2.19}$$

where $\hat{a}_0$ is the zero-mode of the U(1) current, which is the canonical conjugate to $\hat{\phi}_0$: $[\hat{\phi}_0, \hat{a}_0] = i$.

2.1.4 Matrix product factorization

The second-quantized amplitude in Eq. (2.12) can be readily converted into a matrix product state. Between each pair of adjacent $\hat{B}^m$ operators, we can insert a unit resolution into a complete set of states over the conformal Hilbert space,

$$\mathbb{1} = \sum_{\alpha} |\alpha\rangle\rangle\langle\langle\alpha|, \tag{2.20}$$

the orthonormal basis states $|\alpha\rangle\rangle$ can be constructed from the Virasoro descendants through the Gram-Schmidt process [26]. Due to the $e^{-\gamma^2 \hat{L}_0}$ factor introduced by the cylinder evolution $\hat{U}_\gamma$ in the $\hat{B}^m$ operators, the CFT states with higher energy (measured by $\gamma \hat{L}_0$) are exponentially suppressed at finite cylinder perimeter. This allows us to truncate the conformal Hilbert space, and keep only the lowest few levels of descendants. This then yields a matrix product state for the CFT-derived model wave function,

$$|\Psi\rangle = \sum_{\{m\}} [\cdots B^{m_2} B^{m_1} B^{m_0}]_{\text{out,in}} \; |\cdots, m_2, m_1, m_0\rangle. \tag{2.21}$$

Here, each orbital is represented by a B^m matrix, which is essentially a CFT three-point function, and $|\cdots, m_2, m_1, m_0\rangle$ is the Slater-determinant basis states constructed from Landau orbitals with occupation numbers $\{m\}$. The matrix elements $[B^m]_{\alpha\beta} = \langle\alpha|\hat{B}^m|\beta\rangle$ can be constructed iteratively from the Virasoro algebra. The details of the numerical algorithm can be found in Ref. [27].

2.1.5 Conformal blocks for non-Abelian quasiholes

In the CFT formalism, similar to the electrons, a localized quasihole at position η is represented by the insertion of a primary field $\mathcal{Q}(\eta)$ into the conformal correlator. The

simplest example is the so-called Abelian quasihole, which is simply a U(1) primary field $:e^{i\frac{1}{\sqrt{q}}\phi(\eta)}:$. In this chapter, we are interested in the so-called k-particle clustered states, for which the fundamental quasihole takes a tensor-product form

$$\mathcal{Q}(\eta) = \sigma(\eta) \otimes :e^{i\frac{1}{k\sqrt{q}}\phi(\eta)}: \ . \tag{2.22}$$

Here the integer k is the same as the subscript k as in $\mathbb{Z}_k$ Read-Rezayi (RR) states [73]. Therefore, for the Moore-Read [60] (MR) state we have $k = 2$, and for the $\mathbb{Z}_3$ Read-Rezayi state we have $k = 3$. The Gaffnian wave function [81] that we will discuss later is characterized by $k = 2$.

Compared with the case without quasiholes discussed earlier, the new challenge here stems from the nontrivial fusion of the neutral σ field of the non-Abelian quasiholes. Fixing all the pinned quasihole coordinates does not specify a single wave function. Rather, it defines a multi-dimensional vector space of degenerate states [60, 64]. The action of the quasihole operator $\hat{\mathcal{Q}}(\eta)$ on a CFT state $|\alpha\rangle\rangle$ does not in general yield a unique result. Instead, one could choose from the multiple Verma modules in the fusion result of σ and α. In the MPS construction, instead of inserting a unit resolution over the full CFT Hilbert space as in Eq. (2.20), we can pick a single Verma module Φ and insert a projector

$$\mathbb{1}_\Phi = \sum_\alpha^\Phi |\alpha\rangle\rangle\langle\langle\alpha|, \tag{2.23}$$

where $|\alpha\rangle\rangle$ spans an orthonormal basis in the Verma module Φ. This leads to the conformal-block [60] basis in the degenerate space of quasihole states, labeled by topological charges on fusion tree diagrams [61, 48].

We illustrate this procedure using the MR state [60]. Its neutral CFT is given by the holomorphic part of the Ising CFT, with primary fields $(\mathbb{1}, \psi, \sigma)$ and fusion rules

$$\psi \times \psi = \mathbb{1}, \ \ \psi \times \sigma = \sigma, \ \ \sigma \times \sigma = \mathbb{1} + \psi, \tag{2.24}$$

where ψ represents an electron and σ carries a quasihole. Since only $\sigma \times \sigma$ has multiple outcomes, to enumerate n-quasihole states, we only need to consider the fusion trees of n σ fields. For example, for an even number of electrons, there are two degenerate four-quasihole states,

$$|\Psi_a\rangle = \quad a = \mathbb{1} \text{ or } \psi. \tag{2.25}$$

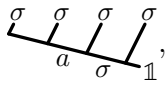

The $\mathbb{Z}_3$ Read-Rezayi state can be described by the $\mathbb{Z}_3$ parafermion conformal field theory [73, 3], also known as the minimal model $\mathcal{M}(5,6)$ [23], with central charge $c = \frac{4}{5}$. The primary fields of this CFT are $(\mathbb{1}, \psi_1, \psi_2, \varepsilon, \sigma_1, \sigma_2)$, with scaling dimensions $(0, \frac{2}{3}, \frac{2}{3}, \frac{2}{5}, \frac{1}{15}, \frac{1}{15})$. Electrons and quasiholes are represented by ψ_1 and σ_1 fields, resp. The fusion rules of these fields are

	$\mathbb{1}$	ψ_1	ψ_2	ε	σ_1	σ_2
ψ_1	ψ_1	ψ_2	$\mathbb{1}$	σ_2	ε	σ_1
σ_1	σ_1	ε	σ_2	$\psi_2 + \sigma_1$	$\psi_1 + \sigma_2$	$\mathbb{1} + \varepsilon$

There are again two four-quasihole states

$$|\Psi_a\rangle = \quad a = \psi_1 \text{ or } \sigma_2. \tag{2.26}$$

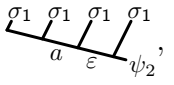

For each set of fusion tree labels, we can construct a MPS for the corresponding conformal-block wave function following the same steps as earlier. We use (χ, ζ) to denote the real and the imaginary parts of the quasihole coordinate $\eta = \chi + i\zeta$. In Eq. (2.8), we now have extra $\hat{\mathcal{Q}}(\chi_i + i\zeta_i)$ operators at positions determined by time ordering. Considering

$$\hat{\mathcal{Q}}(\chi + i\zeta) = e^{\chi\gamma\hat{L}_0}\hat{\mathcal{Q}}(i\zeta)e^{-\chi\gamma\hat{L}_0}, \tag{2.27}$$

the time evolution in Eq. (2.11) is further punctured by $\hat{\mathcal{Q}}(i\zeta_i)$ insertions at time slices χ_i. Recall that when we define the orbital $\hat{B}^m$ operators in Eq. (2.13), we cut the cylinder evolution into chunks of length γ and assigned them to individual orbitals. The time ordering now requires us to insert $\hat{\mathcal{Q}}(i\zeta)$ into the cylinder factor $\hat{U}_\gamma$ in the

$\hat{B}^m$ operator at the orbital adjacent to the quasihole. We define the fractional part (relative to orbital separation γ) of the χ coordinate as

$$\langle \chi \rangle = \chi - \gamma \, \lfloor \chi/\gamma \rfloor \,, \tag{2.28}$$

where the floor function $\lfloor x \rfloor \in \mathbb{Z}$ denotes the largest integer no greater than x. Then, without modifying the $\hat{B}^m$ operators, the quasihole insertion $\mathcal{Q}(\chi + i\zeta)$ is represented in Eq. (2.12) by the insertion of

$$\hat{B}_{\mathcal{Q}}(\chi + i\zeta) \equiv \hat{U}_{\langle \chi \rangle} \hat{\mathcal{Q}}(i\zeta) \hat{U}^{-1}_{\langle \chi \rangle} \tag{2.29}$$

between the $\hat{B}^m$ operators for orbitals $\lfloor \chi/\gamma \rfloor$ and $\lfloor \chi/\gamma \rfloor + 1$. The ambiguity in the action of $\hat{B}_{\mathcal{Q}}$ on a CFT state due to the nontrivial fusion rules is resolved according to the fusion tree diagram labeling.

There is one last issue that we glossed over in the earlier discussion. When we expand the CFT-derived wave function into Slater-determinant basis states in Eq. (2.7), we place the electron contours along the center of each occupied orbital. Therefore, for different Slater-determinant states, the placement of electrons in the x direction is different. This creates a problem when we also have fixed quasihole insertions in the conformal correlator: we need to commute the quasihole operators and the electron operators into time ordering.[2] Since the quasiholes are local with respect to the electrons, even in the non-Abelian case, the most we can get is a minus sign when we commute a quasihole across an electron. This mutual-statistics minus sign is not gauge invariant; it depends on the specific gauge choice for the holomorphic half of the CFT. Fortunately, this sign is very easy to determine using the MPS code, which is essentially a truncated CFT calculator.

Table 2.1: Numerical data for quasihole radii R and the correlation length associated with wave function orthogonality.

	ν	R/ℓ_0		$\xi_{\rm ortho}/\ell_0$
Laughlin	$\frac{1}{3}$	$\frac{e}{3}$: 2.6		-
Moore-Read	$\frac{1}{2}$	$\frac{e}{4}$: 2.8	$\frac{e}{2}$: 2.7	2.6
$\mathbb{Z}_3$ Read-Rezayi	$\frac{3}{5}$	$\frac{e}{5}$: 3.0	$\frac{3e}{5}$: 2.8	3.4

2.2 Physical results

We now move on to discuss the physical results obtained using the MPS technique. For the $\mathbb{Z}_{k\leq 3}$ RR states (including Laughlin and MR at $k = 1, 2$), as well as the Gaffnian wave function, we construct MPS for localized quasiholes, and estimate their radii from the electron density profile. From adiabatic transport, we obtain the braiding matrices, verify the link between statistics and monodromy for $\mathbb{Z}_{k\leq 3}$ RR at large quasihole separations, and determine the associated length scales. Numerical data are summarized in Table 2.1. Through these characterizations, we confirm the Fibonacci nature of the $\mathbb{Z}_3$ RR quasiholes, and we provide the first size estimate for these exotic excitations. Our results also give a microscopic diagnosis for the pathology of the Gaffnian.

2.2.1 Moore-Read and $\mathbb{Z}_3$ Read-Rezayi quasiholes

In this subsection we examine the $\mathbb{Z}_{k\leq 3}$ RR states at fillings $\nu = \frac{k}{k+2}$.

Before studying the braiding statistics, we first check whether the quasiholes are indeed localized excitations. We check the charge $\nu e = \frac{ke}{k+2}$ Abelian quasiholes, and for the $k > 1$ theories, also the fundamental $\frac{e}{k+2}$ non-Abelian quasiholes. In the electron density profile, we find a *localized* and *isotropic* reduction around quasihole centers, which does not depend on the presence of other quasiholes sufficiently far away. An example is given in Fig. 2.1 for the RR $\frac{e}{5}$, $\frac{2e}{5}$ (two $\frac{e}{5}$ fused in σ_2), and $\frac{3e}{5}$

[2]We do not have to worry about commuting the *fixed* quasiholes themselves.

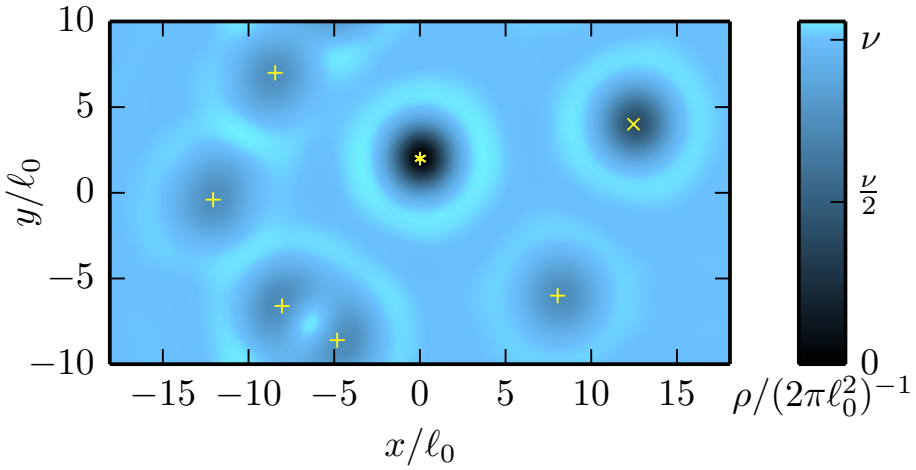

Figure 2.1: Electron density for $\mathbb{Z}_3$ RR $\frac{e}{5}(+)$, $\frac{2e}{5}(\times)$ and $\frac{3e}{5}(*)$ quasiholes on an infinite cylinder with perimeter $L_y = 20\ell_0$.

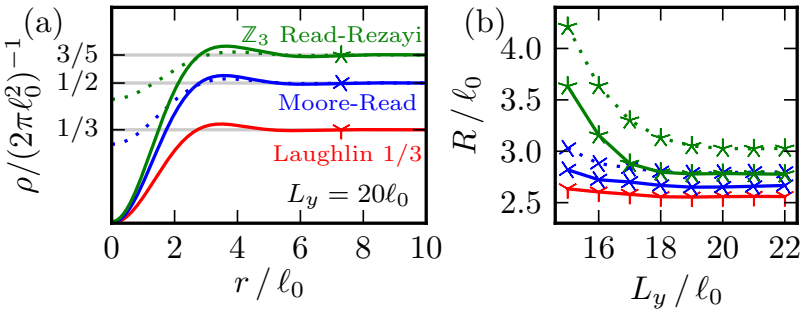

Figure 2.2: (a) shows the radial dependence of electron density ρ near a quasihole, at $L_y = 20\ell_0$. For $\mathbb{Z}_{k=2,3}$ RR, we study both the $\frac{e}{k+2}$ (dotted) and the $\frac{ke}{k+2}$ quasiholes (solid curves). (b) shows the quasihole radius R as a function of cylinder perimeter L_y, using the markers defined in (a).

quasiholes. The electron density displays small ripples in the periphery of a quasihole, as seen more clearly in the radial plots in Fig. 2.2(a). Following Ref. [46], we extract the quasihole radius R from the second moment of the charge excess distribution [3]. This definition is susceptible to the thin-cylinder density wave background [89], but it quickly converges as L_y increases [Fig. 2.2(b)]. We note that the quasihole size barely depends on k. For $k > 1$, the $\frac{e}{k+2}$ fundamental and the $\frac{ke}{k+2}$ Abelian quasiholes also have comparable sizes. Listed in Table 2.1, the numerical values are consistent with those previously reported for $\mathbb{Z}_{k=1,2}$ [46, 70, 86]. For the $\mathbb{Z}_3$ RR quasiholes, our calculation provides the first radius estimate, $R \sim 3.0\,\ell_0$. Strictly speaking this is a lower bound, as the quasiholes in the Coulomb ground state could be larger [46].

With the localized nature of the quasiholes established, we now examine their braiding statistics. For $\mathbb{Z}_{k=2,3}$ RR states, we consider the two braids $\{12\}$ and $\{23\}$ parametrized by the mobile quasihole η, as depicted in Fig. 2.3. We compute the Berry connection over each $\mathrm{d}\eta$ segment along the braid

$$\mathcal{A}_{ab}(\eta;\mathrm{d}\eta) \equiv e^{-i\mathrm{d}\eta A_{ab}(\eta)} \equiv \frac{\langle\Psi_a(\eta+\mathrm{d}\eta)|\Psi_b(\eta)\rangle}{\|\Psi_a(\eta+\mathrm{d}\eta)\|\cdot\|\Psi_b(\eta)\|}, \tag{2.30}$$

in the unnormalized $\{|\Psi_a\rangle\}$ basis from Eqs. (2.25, 2.26). Due to the nontrivial monodromy of the CFT correlator, $|\Psi_a(\eta)\rangle$ is multivalued in η. At each stationary quasihole, a branch cut runs vertically around the cylinder, generating singularities in the Berry connection. If we keep η and $\eta + \mathrm{d}\eta$ on opposite sides of the cut while letting $\mathrm{d}\eta \to 0$ [Fig. 2.3], the connection $\mathcal{A}(\eta;\mathrm{d}\eta)$ tends to a constant matrix $\mathcal{B}$ *not* equal to

[3] This definition of R is very sensitive to the tail of the charge excess distribution. It clearly distinguishes quasihole sizes in different theories, even though the extent of the quasihole seems comparable between different curves in Fig. 2.2(a) by direct inspection.

the identity:

$$\mathcal{B}_{\rm MR}^{\{12\}} = \begin{bmatrix} 1 & 0 \\ 0 & i \end{bmatrix}, \quad \mathcal{B}_{\rm RR}^{\{12\}} = \begin{bmatrix} e^{i3\pi/5} & 0 \\ 0 & 1 \end{bmatrix},$$
$$\mathcal{B}_{\rm MR}^{\{23\}} = \begin{bmatrix} 0.5005_5 + 0.5005_5 i & 0.4994_6 - 0.4994_6 i \\ 0.4994_6 - 0.4994_6 i & 0.5005_5 + 0.5005_5 i \end{bmatrix}, \tag{2.31}$$
$$\mathcal{B}_{\rm RR}^{\{23\}} = \begin{bmatrix} 0.50008_8 + 0.36333_6 i & 0.6357_4 - 0.4618_3 i \\ 0.63610_9 - 0.46215_7 i & 0.19101_2 + 0.58786_8 i \end{bmatrix}.$$

These matrices virtually coincide with the half-braid matrices [61] of the CFT correlators [18, 3], as in[4]

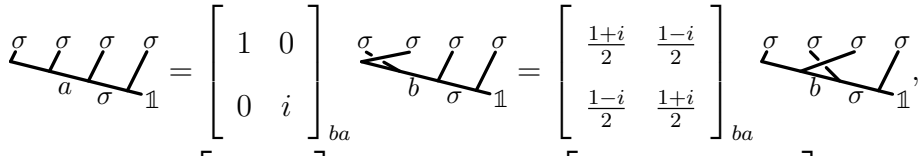

(2.32)

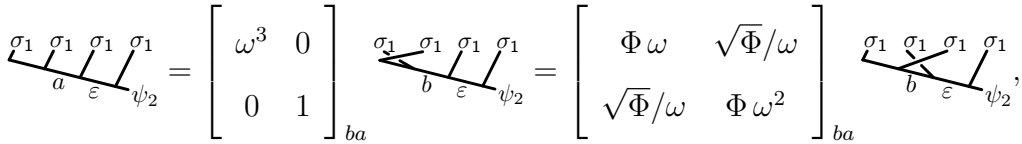

(2.33)

with $\omega = e^{i\pi/5}$ and $\Phi = \frac{\sqrt{5}-1}{2}$. The subscripts in Eq. (2.31) give the last-digit deviations from the exact values. The $\mathcal{B}^{\{12\}}$ are of machine precision at moderate L_y, because in the actual calculations we push the inert quasiholes outside of the braiding loop to infinity [see Eq. (2.35)], which essentially decouples the two conformal blocks for the $\{12\}$ braid.

The above half-braid $\mathcal{B}$ matrices, when squared, give the monodromy prediction for the braiding statistics, namely, Ising and Fibonacci for $\mathbb{Z}_{k=2,3}$ RR, resp. These matrices should come out exactly as the CFT prediction, since we are implementing exactly the conformal blocks up to CFT truncation [106]. The actual braiding matrices are determined by the Wilson loop, which, in addition to the $\mathcal{B}$ matrices, also

[4]The RR matrices here are unitarily similar to Ref. [3], due to their fusion tree choice versus our .

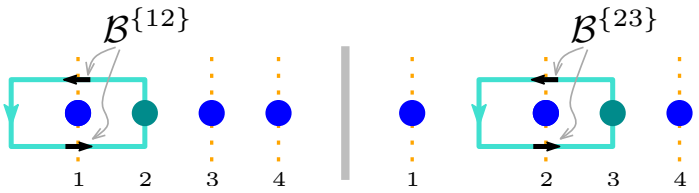

Figure 2.3: Two braids of four-quasihole states, $\{12\}$ and $\{23\}$. We draw in yellow the branch cuts passing through each quasihole, and mark the half-braid $\mathcal{B}$ matrices by black arrows.

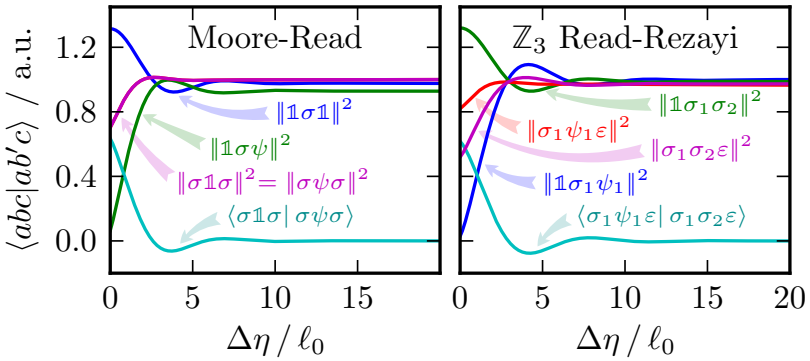

Figure 2.4: Dependence of the overlaps on the quasihole separation $\Delta\eta$ at $L_y = 20\ell_0$. $\|abc\|^2$ is shorthand for $\langle abc|abc\rangle$.

depends on the Berry connections away from the branch cuts. These non-singular contributions are responsible for the potential discrepancy between monodromy and statistics, and are related to the overlap matrix $\langle\Psi_a|\Psi_b\rangle$ with fixed quasihole positions. As detailed in Ref. [18], *if* at large quasihole separation $|\Delta\eta|$, the overlap converges exponentially fast to a constant diagonal matrix,

$$\langle\Psi_a|\Psi_b\rangle = C_a\delta_{ab} + \mathcal{O}(e^{-|\Delta\eta|/\xi_{ab}}), \text{ with } C_a \neq 0, \tag{2.34}$$

then, except for the branch cuts, the Berry connection vanishes up to an exponentially small correction $A_{ab}(\eta) \sim \mathcal{O}(e^{-|\Delta\eta|/\xi_{ab}})$ after subtracting the Aharonov-Bohm phase from the background magnetic field. Hence, Eq. (2.34) quantifies a sufficient condition for the equivalence between monodromy and statistics for well separated quasiholes. We now examine its validity for $\mathbb{Z}_{k=2,3}$ RR. To simplify the functional form, we keep only two quasiholes at a finite separation $\Delta\eta$ and push others to infinity. The resulting

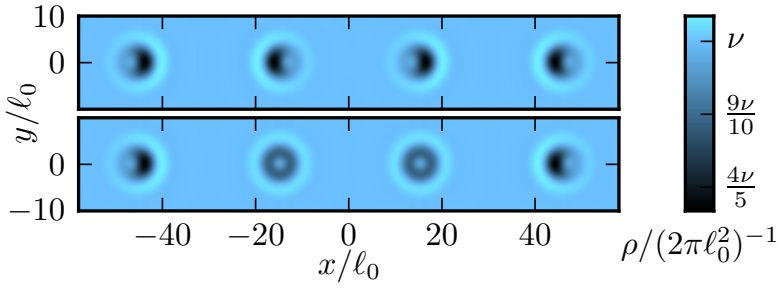

Figure 2.5: Electron density for Gaffnian $\frac{e}{5}$ quasiholes in pair fusion channel $\mathbb{1}$ (top) vs. φ (bottom) [Eq. (2.36)] at $L_y = 20\ell_0$.

states are labeled by fusion trees

$$|abc\rangle \equiv \begin{array}{ccccc} a & & \sigma & & \sigma \\ & \searrow & & \swarrow & \\ & & b & & \\ & & & \searrow & \\ & & & & c \end{array} \text{ (for MR) or } \begin{array}{ccccc} a & & \sigma_1 & & \sigma_1 \\ & \searrow & & \swarrow & \\ & & b & & \\ & & & \searrow & \\ & & & & c \end{array} \text{ ($\mathbb{Z}_3$ RR)}, \tag{2.35}$$

and implemented by setting the MPS boundary conditions to the leading eigenvectors of the MPS transfer matrix in topological sectors a and c [27]. Plotted in Fig. 2.4, $\langle abc|ab'c\rangle$ indeed has the exponential convergence form of Eq. (2.34) in all channels. The correlation lengths can be estimated by curve fitting, or more conveniently, extracted from the spectral gaps of the transfer matrix (Sec. 2.A). Here we focus on the length scale ξ_{ortho} associated with the decaying off-diagonal elements, characterizing the orthogonality between conformal blocks. The numerical values are catalogued in Table 2.1. For MR, our results agree with Ref. [6]. For $\mathbb{Z}_3$ RR, combined with the $\mathcal{B}$ matrices shown earlier, the finite correlation lengths establish the quasiholes as Fibonacci anyons. At the $\nu = 12/5$ plateau[103], with a magnetic field of 5.4 T, $\xi \sim 3.4\,\ell_0$ translates to 0.038 μm. To put this in perspective, the inter-quasihole spacing in an interferometer is on the order of 0.1 μm [76] – the quasiholes are not quite in the well-separated regime in this case.

2.2.2 Gaffnian quasiholes

Finally, we go beyond the $\mathbb{Z}_k$ RR series, and study the Gaffnian [81] wave function at filling $\nu = 2/5$. It is described [81] by the non-unitary generalization of the Ising

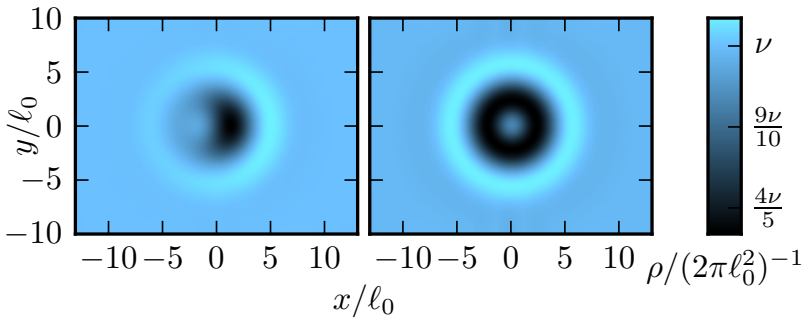

Figure 2.6: Electron density around a single Gaffnian $\frac{e}{5}$ quasihole in the $|\mathbb{1}\sigma\rangle$ (left panel) and the $|\sigma\varphi\rangle$ (right panel) channels, on an infinitely long cylinder with perimeter $L_y = 20\ell_0$.

CFT, namely the minimal model $\mathcal{M}(3,5)$ with central charge $c = -\frac{3}{5}$. The primary fields of this CFT are $(\mathbb{1}, \psi, \sigma, \varphi)$, with scaling dimensions $(0, \frac{3}{4}, -\frac{1}{20}, \frac{1}{5})$. The ψ (resp. σ) field represents an electron (resp. a quasihole), with fusion rules

	$\mathbb{1}$	ψ	σ	φ
ψ	ψ	$\mathbb{1}$	φ	σ
σ	σ	φ	$\mathbb{1}+\varphi$	$\psi+\sigma$

Due to the non-unitarity, the Gaffnian wave function is conjectured to describe a gapless state rather than a gapped topological phase [72].

There are two four-quasihole wave functions,

$$|\Psi_a\rangle = \quad a \quad , \quad a = \mathbb{1} \text{ or } \varphi. \tag{2.36}$$

Each fundamental quasihole has charge $e/5$. We start from the electron density profile of these states, as shown in Fig. 2.5. In contrast to the $\mathbb{Z}_k$ RR states, the density profile here exhibits a strong fusion-channel dependence, and also a dipole-like anisotropy for $|\Psi_{\mathbb{1}}\rangle$, despite the clear separation of quasiholes. To see such peculiarities more clearly, we push the quasihole separations to infinity, leaving only a single fully isolated quasihole. In this limit, the conformal blocks are labeled by fusion tree segments

$$|ab\rangle \equiv \quad a \quad b. \tag{2.37}$$

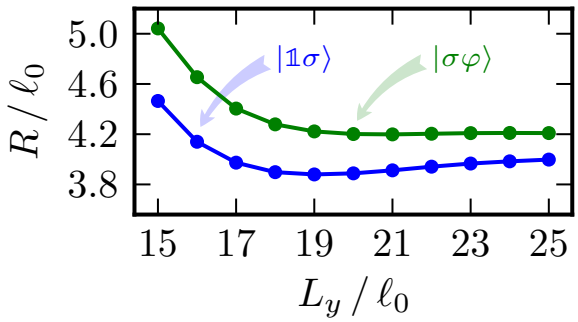

Figure 2.7: Radii of Gaffnian quasiholes in $|\mathbb{1}\sigma\rangle$ and $|\sigma\varphi\rangle$ channels, as a function of the cylinder perimeter L_y.

We only need to consider $|ab\rangle = |\mathbb{1}\sigma\rangle$ and $|\sigma\varphi\rangle$, since all the other possibilities can be obtained by either fusing (trivially) with ψ, or flipping the cylinder axis $x \to -x$. Fig. 2.6 shows the electron density profile for each case. The anisotropic dipole structure is clearly visible for $|\mathbb{1}\sigma\rangle$, in contrast to the isotropic $|\sigma\varphi\rangle$. We emphasize that the local distinguishability of different conformal blocks persists even when the quasiholes are *infinitely* separated. This casts doubt on their topological degeneracy, although it remains unclear whether the density peculiarities are genuine, or artifacts at finite cylinder perimeter L_y.[5]

Similar to the $\mathbb{Z}_{k\leq 3}$ Read-Rezayi quasiholes analyzed in previous subsection, we estimate the quasihole radius from the second moment of the charge excess distribution [Fig. 2.7]. We have also examined the Abelian charge $\frac{2e}{5}$ quasihole obtained by fusing two $\frac{e}{5}$ quasiholes in the $\mathbb{1}$ channel. We find a localized and isotropic density reduction around each Abelian quasihole, but this calculation turns out to be rather susceptible to the conformal Hilbert space truncation, and we have trouble reaching convergence in the radius calculation.

We now study the braiding of Gaffnian quasiholes. Unlike the unitary $\mathbb{Z}_k$ theories, the conformal blocks for Gaffnian are not asymptotically orthogonal in general. In place of the Berry connection, we consider the linear transform that relates $|\Psi_a(\eta)\rangle$

[5]See Sec. 2.A for more details.

to $|\Psi_b(\eta + \mathrm{d}\eta)\rangle$,

$$\frac{|\Psi_b(\eta)\rangle}{\|\Psi_b(\eta)\|} = \sum_a \widetilde{\mathcal{A}}_{ab}(\eta; \mathrm{d}\eta) \frac{|\Psi_a(\eta + \mathrm{d}\eta)\rangle}{\|\Psi_a(\eta + \mathrm{d}\eta)\|}, \tag{2.38}$$

and we examine its behavior along the braids depicted in Fig. 2.3. Across the branch cuts, the analogue of the unitary half-braid matrices $\mathcal{B}$ are $\widetilde{\mathcal{B}} \equiv \widetilde{\mathcal{A}}(\eta; \mathrm{d}\eta \to 0)$,

$$\widetilde{\mathcal{B}}^{\{12\}} = \begin{bmatrix} e^{i\pi/5} & 0 \\ 0 & e^{i2\pi/5} \end{bmatrix}, \quad \widetilde{\mathcal{B}}^{\{23\}} = \begin{bmatrix} 1.616_2 & 0.746_1 + 1.028_1 i \\ 0.746_1 + 1.028_1 i & -0.4995_5 + 1.537_1 i \end{bmatrix},$$

in agreement with the CFT prediction

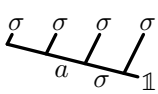

$= \begin{bmatrix} \omega & 0 \\ 0 & \omega^2 \end{bmatrix}_{ba}$
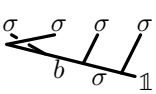

$= \begin{bmatrix} 1/\Phi & \omega^{\frac{3}{2}}/\Phi^{\frac{1}{2}} \\ \omega^{\frac{3}{2}}/\Phi^{\frac{1}{2}} & \omega^3/\Phi \end{bmatrix}_{ba}$
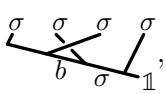

, (2.39)

with errors given in subscripts. Again, this agreement indicates that our MPS correctly implements the conformal blocks. The non-unitarity of $B^{\{23\}}$ comes from that of the $F_\sigma^{\sigma\sigma\sigma}$ matrix [1]. Away from the branch cuts, the behavior of $\widetilde{\mathcal{A}}$ is again controlled by the overlaps $\langle \Psi_a | \Psi_b \rangle$ as a function of quasihole separations. Ideally, we would like to examine the validity of Eq. (2.34) for its individual matrix elements, as we do for the $\mathbb{Z}_k$ RR states. In the $L_y \lesssim 25\ell_0$ regime accessible by MPS, however, this calculation is plagued by finite-size effects, and we have trouble identifying its planar limit.

Fortunately, the conformal-block orthogonality measure

$$\cos\theta_{\mathbb{1},\varphi} \equiv \frac{\langle \sigma \mathbb{1} \sigma | \sigma \varphi \sigma \rangle}{\|\sigma \mathbb{1} \sigma\| \cdot \|\sigma \varphi \sigma\|} \tag{2.40}$$

is immune from such artifacts. Here we are keeping only two quasiholes at a finite separation $\Delta\eta$ while the outer two are set to $\pm\infty$, and we use the notation of Eq. (2.35). As shown in Fig. 2.8, $\cos\theta_{\mathbb{1},\varphi}$ decays exponentially as $\Delta\eta$ increases, but the associated length scale ξ_{ortho} (as in $\cos\theta_{\mathbb{1},\varphi} \propto e^{-|\Delta\eta|/\xi_{\mathrm{ortho}}}$) diverges as $L_y \to \infty$, in sharp contrast to the $\mathbb{Z}_k$ RR states. Hence, in the planar limit, the conformal blocks in Eq. (2.36) with an untwisted tree structure acquires orthogonality extremely slowly,

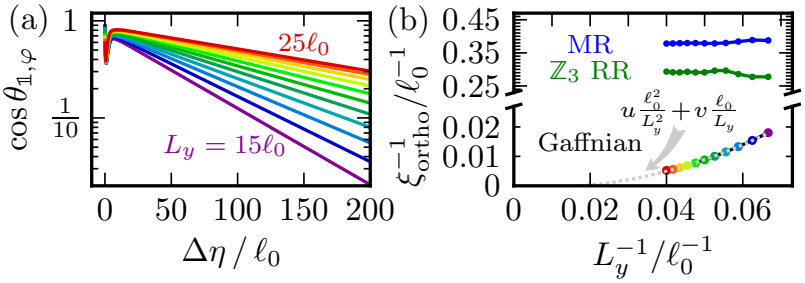

Figure 2.8: (a) shows the asymptotic conformal-block orthogonality at large quasihole separations for Gaffnian, color-coded by $L_y \in [15\ ..\ 25]\,\ell_0$. (b) compares the L_y-dependence of the associated length scales between different theories. The Gaffnian curve has the best fit at $u = 5.46(9)$, $v = -0.095(5)$.

following a power law in $\Delta\eta$ (rather than exponentially), signaling the breakdown of the screening condition Eq. (2.34) for Gaffnian. This highlights its gapless nature, and largely rules out the possibility of defining a sensible braiding statistics for the Gaffnian quasiholes, since the non-universal corrections to the monodromy matrix are not exponentially small in quasihole separations.

2.3 Discussion

To summarize, in this chapter we have extended the MPS technique to non-Abelian quasiholes, and have examined numerically the quasiholes in the $\mathbb{Z}_{k\leq 3}$ RR and the Gaffnian states. We provide the first size estimate for the $\mathbb{Z}_3$ RR quasiholes, and also the first microscopic, quantitative verification of their Fibonacci nature. We determine the correlation lengths associated with the exponential convergence of their braiding statistics. In the context of topological quantum computing, these length scales set the limit of the topological protection against decoherence in realistic systems [6, 21, 17]. Our results also shed new light on the pathology of the Gaffnian wave function manifested in its quasiholes.

2.A The MPS transfer matrix

Here we address some technical aspects of the matrix product states on an infinite cylinder using the transfer matrix formalism.

Following the notation of Ref. [27], we consider the transfer matrix $E = \sum_m^{0,1} (B^m)^* \otimes B^m$, where the B^m matrix is associated with an empty ($m = 0$) or occupied ($m = 1$) Landau orbital in the MPS. The transfer matrix is the basic building block of any generic wave function overlap $\langle \Psi | \Psi' \rangle$. It acts on a direct product of two copies of the truncated conformal Hilbert space, one copy for $\langle \Psi |$, and the other for $|\Psi'\rangle$. From the fusion rules, we find that the CFT Hilbert space can be naturally split into two sectors, each being closed under fusion with the electron (although they are connected by fusion with the quasihole). We refer to them as the "vac" and the "qh" sectors:

	vac	qh
Moore-Read	$\mathbb{1}, \psi$	σ
$\mathbb{Z}_3$ Read-Rezayi	$\mathbb{1}, \psi_1, \psi_2$	$\varepsilon, \sigma_1, \sigma_2$
Gaffnian	$\mathbb{1}, \psi$	σ, φ

The B^m matrices are block-diagonal in the sector index, $B^m = \bigoplus_\alpha B^m_\alpha$, with α summed over {vac, qh}. Therefore, the transfer matrix is also block-diagonal,

$$E = \bigoplus_{\alpha,\beta} E_{\alpha,\beta}, \text{ with } E_{\alpha,\beta} = \sum_m (B^m_\alpha)^* \otimes B^m_\beta. \tag{2.41}$$

We denote by $\lambda^{(i)}_{\alpha,\beta}$ the i-th largest eigenvalue of $E_{\alpha,\beta}$. The MPS auxiliary space is constructed from the truncated conformal Hilbert space, and the truncation is constrained by the entanglement area law. In our calculations, we have to deal with

transfer matrix blocks (after various reductions [27]) with dimensions as large as

	(vac, vac)	(vac, qh)	(qh, qh)
Moore-Read	1.1×10^7	1.5×10^7	2.0×10^7
$\mathbb{Z}_3$ Read-Rezayi	3.6×10^7	5.5×10^7	8.4×10^7
Gaffnian	1.3×10^7	2.0×10^7	3.0×10^7

Incidentally, for the braiding and the overlap calculations, we have to work on the full direct product space without symmetry reduction, the dimension of which can be up to 25 times as large as the sizes mentioned in the previous table.

As explained in the main text, the central object in our braiding study is the overlap matrix $\langle abc|ab'c\rangle$, and we are particularly interested in its exponential convergence

$$\langle abc|ab'c\rangle = C_{abc}\delta_{bb'} + \mathcal{O}(e^{-|\Delta\eta|/\xi_{\langle abc|ab'c\rangle}}). \tag{2.42}$$

The calculation of the overlap $\langle abc|ab'c\rangle$ involves repeated actions of the transfer matrix over the distance $\Delta\eta$ between the two quasiholes. Hence, in the limit of large $\Delta\eta$, the overlap is dominated by the leading eigenmodes of the transfer matrix, and the associated correlation lengths can be simply determined from the spectral gaps of the transfer matrix, without resorting to curve fitting. In the following we explain this using three representative examples. First, consider the off-diagonal element $\langle\sigma_1\psi_1\varepsilon|\sigma_1\sigma_2\varepsilon\rangle$ for the $\mathbb{Z}_3$ Read-Rezayi state. In this case, the action of the transfer matrix over the $\Delta\eta$ interval is confined to the (vac, qh) sector of the product space, while its action outside of the $\Delta\eta$ interval is purely in the (qh, qh) sector. At large $\Delta\eta$, we must have

$$\langle\sigma_1\psi_1\varepsilon|\sigma_1\sigma_2\varepsilon\rangle \sim \left(\frac{\lambda^{(1)}_{\text{vac,qh}}}{\lambda^{(1)}_{\text{qh,qh}}}\right)^{\Delta\eta/\gamma}. \tag{2.43}$$

Here $\gamma = 2\pi\ell_0^2/L_y$ is the separation between adjacent Landau orbitals, while $\lambda^{(1)}_{\text{vac,qh}}$ and $\lambda^{(1)}_{\text{qh,qh}}$ are the largest eigenvalues of the transfer matrix in sectors (vac,qh) and

(qh, qh), resp. The correlation length is then given by

$$\xi_{\text{ortho}} = \left[\frac{L_y}{2\pi\ell_0^2} \log \left(\frac{\lambda^{(1)}_{\text{qh,qh}}}{\lambda^{(1)}_{\text{vac,qh}}} \right) \right]^{-1} . \tag{2.44}$$

As the second example, we consider the norm $\|\mathbb{1}\sigma\psi\|^2$ for the Moore-Read state. To the leading order, we have

$$\|\mathbb{1}\sigma\psi\|^2 \sim \left(\frac{\lambda^{(1)}_{\text{qh,qh}}}{\lambda^{(1)}_{\text{vac,vac}}} \right)^{\Delta\eta/\gamma} , \tag{2.45}$$

while $\lambda^{(1)}_{\text{vac,vac}}$ and $\lambda^{(1)}_{\text{qh,qh}}$ are the largest eigenvalues of the transfer matrix in sectors (vac,vac) and (qh, qh), resp. For $\|\mathbb{1}\sigma\psi\|^2$ to approach a non-zero constant value when $\Delta\eta \to \infty$ as in Eq. (2.42), we need to have $\lambda^{(1)}_{\text{vac,vac}} = \lambda^{(1)}_{\text{qh,qh}}$. This turns out to be true for the $\mathbb{Z}_{k=2,3}$ Read-Rezayi states, up to small finite-size corrections (see below). To characterize the exponential convergence of the norm, we have to consider the second largest eigenvalue in the (qh,qh) channel, $\lambda^{(2)}_{\text{qh,qh}}$. The associated correlation length is given by

$$\xi_{\text{qh}} = \left[\frac{L_y}{2\pi\ell_0^2} \log \left(\frac{\lambda^{(1)}_{\text{qh,qh}}}{\lambda^{(2)}_{\text{qh,qh}}} \right) \right]^{-1} . \tag{2.46}$$

Finally, the correlation length associated with the norm $\|\sigma\psi\sigma\|^2$ for the Moore-Read state is similarly given by

$$\xi_{\text{vac}} = \left[\frac{L_y}{2\pi\ell_0^2} \log \left(\frac{\lambda^{(1)}_{\text{vac,vac}}}{\lambda^{(2)}_{\text{vac,vac}}} \right) \right]^{-1} . \tag{2.47}$$

The numerical calculations of ξ_{vac} and ξ_{qh} are more challenging than ξ_{ortho}, since they depend on subleading eigenvalues of the transfer matrix.

We now examine the $\lambda^{(1)}_{\text{vac,vac}} = \lambda^{(1)}_{\text{qh,qh}}$ condition more carefully. To have a physical understanding of its implication, we adopt the plasma analogy and reinterpret the overlap in Eq. (2.45) as the partition function $e^{-F(\Delta\eta)}$ with two pinned charges representing the two quasiholes at a separation $\Delta\eta$. The derivative of the free energy

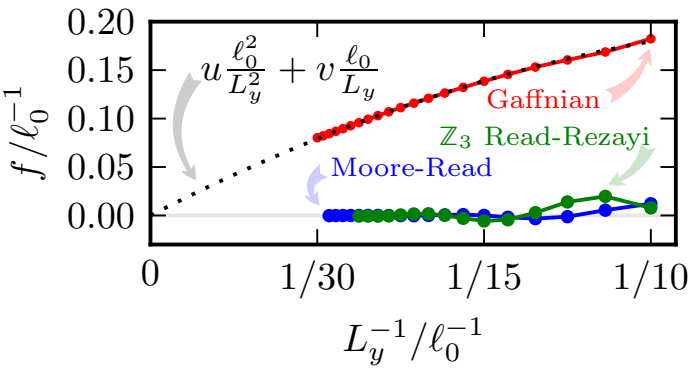

Figure 2.9: Asymptotic repulsion f between two plasma charges representing pinned quasiholes. The Gaffnian curve is fitted by the zero-intercept quadratic formula $f\ell_0 = u\frac{\ell_0^2}{L_y^2} + v\frac{\ell_0}{L_y}$. The best fit has $u = -8.6(2)$ and $v = 2.66(1)$, with the standard error in the last digit given in parentheses.

$F(\Delta\eta)$ with respect to $\Delta\eta$ gives an effective force between the plasma charges

$$f = -\frac{\mathrm{d}F}{\mathrm{d}\Delta\eta} \sim \frac{L_y}{2\pi\ell_0^2} \log\left(\frac{\lambda^{(1)}_{\mathrm{qh,qh}}}{\lambda^{(1)}_{\mathrm{vac,vac}}}\right). \tag{2.48}$$

Therefore, if $\lambda^{(1)}_{\mathrm{vac,vac}} \neq \lambda^{(1)}_{\mathrm{qh,qh}}$, the two plasma charges representing quasiholes are subject to an asymptotically constant confining (if $f < 0$) or anti-confining (if $f > 0$) force that persists even in the limit of infinite separation. The numerical data are shown in Fig. 2.9. For the Moore-Read and the $\mathbb{Z}_3$ Read-Rezayi states, $\lambda^{(1)}_{\mathrm{vac,vac}}$ and $\lambda^{(1)}_{\mathrm{qh,qh}}$ quickly converge as L_y increases. In contrast, the Gaffnian state features an asymptotic repulsion between infinitely separated plasma charges at a finite cylinder perimeter L_y, although it seems to die off in the planar limit $L_y \to \infty$. This makes it very hard to extract a meaningful correlation length for the diagonal elements of the overlap matrix similar to Eq. (2.46). Fortunately, we can still analyze the correlation length associated with the asymptotic orthogonality of conformal blocks, as discussed in the main text.

As a final comment, we note that the peculiarities observed in the density profile of Gaffnian quasiholes are possibly related to this leading eigenvalue mismatch, and are possibly artifacts at finite cylinder perimeter L_y. Unfortunately, we cannot resolve

this issue using the current MPS approach, due to the fundamental constraint on L_y from the area law of quantum entanglement.

Chapter 3

Zoology of Fractional Chern Insulators

In the rest of this dissertation, we study the fractional Chern insulator (FCI) phase of a partially filled Chern band. We aim to address the following questions regarding this new phase of strongly correlated electrons:

- How to identify its presence from finite-size numerics?
- How does the geometry of the topological band affect the many-body interacting phase?
- How to understand the FCI phase from the perspective of fractional quantum Hall (FQH) effect?
- How to construct model wave functions for FCI?
- Does the FCI system offer something truly new, beyond the scope of conventional FQH?

In this chapter, we show that the FCI phase is present in the Haldane model on the honeycomb lattice [40], in a two-orbital model that resembles half (spin-up) of the Mercury-Telluride two-dimensional topological insulator [15], in the Kagome lattice model with spin-orbit coupling [88], and in the spin-polarized ruby lattice model [45].

These models allow us to study FCI in different physical situations such as different lattices or different number of Bloch bands. Working in a single flattened band, we find in each model a more or less robust Laughlin FQH phase at 1/3 filling in the presence of repulsive two-body nearest-neighbor interactions. The 3-fold degenerate ground states are separated from the excited states by a finite gap and flow into each other upon flux insertion with a period of 3 fluxes. This signals a Hall conductance $\sigma_{xy} = 1/3$. We identify hallmarks of fractional excitations of the Laughlin 1/3 universality class in the energy spectrum as well as the entanglement spectrum. We then discuss the stability of the topological ground state under parameter variation, and test its correlation with the anisotropy of the Berry curvature. We also show that another FCI phase reminiscent of the Pfaffian Moore-Read FQH state [60] is present in the Kagome and ruby lattice models at half filling of the valence band. Finally, we highlight several structures in the higher levels of the particle entanglement spectrum [53, 83] of the ground state at filling 1/3 that may serve as a hint for the stable existence of other FQH states at other fillings, such as the Read-Rezayi series [73].

3.1 Haldane model

The Haldane model [40] is the first studied example of a topological insulator. We would like to see if this model can host fermionic FCI phases (the bosonic version has recently been reported in Refs. [94, 96]). We adopt the honeycomb lattice layout from Ref. [65]. As shown in Fig. 3.1, the two sublattices A and B are connected by the vectors $\mathbf{a}_1 = (0, -1)$, $\mathbf{a}_2 = (\sqrt{3}/2, 1/2)$, $\mathbf{a}_3 = (-\sqrt{3}/2, 1/2)$. We define the lattice translation vectors $\mathbf{b}_1 = \mathbf{a}_2 - \mathbf{a}_3$, $\mathbf{b}_2 = \mathbf{a}_3 - \mathbf{a}_1$. The Haldane model [40] has real hopping amplitude t_1 between nearest neighbors (NN), complex hopping amplitude $t_2 e^{\pm i\phi}$ between next-nearest neighbors (NNN), and an inversion-breaking sublattice potential M.

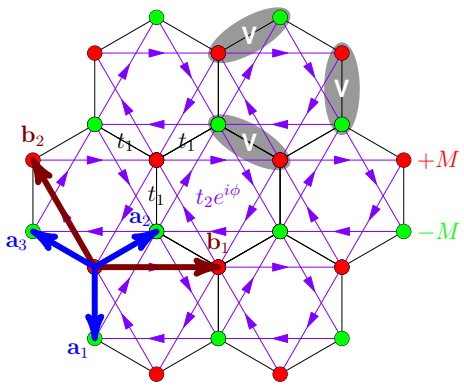

Figure 3.1: The Haldane model on the honeycomb lattice. A and B sublattices are colored in red and green, respectively. The lattice translation vectors are $\mathbf{b}_1 = \mathbf{a}_2 - \mathbf{a}_3$ and $\mathbf{b}_2 = \mathbf{a}_3 - \mathbf{a}_1$. The hopping between NN is t_1, and the hopping between NNN is $t_2 e^{i\phi}$ in the direction of arrows. The density-density repulsion between nearest neighbors is depicted in gray ellipses.

After a Fourier transform to the first Brillouin zone and a gauge transform on the B sublattice $\psi_{\mathbf{k},B} \to e^{i\mathbf{k}\cdot(\mathbf{b}_1+2\mathbf{b}_2)/3}\psi_{\mathbf{k},B}$, the single-particle Hamiltonian can be put in Bloch form as $H = \sum_{\mathbf{k}} (\psi^\dagger_{\mathbf{k},A}, \psi^\dagger_{\mathbf{k},B}) h(\mathbf{k}) (\psi_{\mathbf{k},A}, \psi_{\mathbf{k},B})^{\mathrm{T}}$. Here the lattice momentum $\mathbf{k} = (\mathbf{k}\cdot\mathbf{b}_1, \mathbf{k}\cdot\mathbf{b}_2) \equiv (k_x, k_y)$ is summed over the first Brillouin zone, and the $h(\mathbf{k})$ matrix can be expressed in terms of the identity and 3 Pauli matrices, $h(\mathbf{k}) = d_0 \mathbb{I} + \sum_i d_i \sigma_i$, where

$$d_0 = 2t_2 \cos\phi[\cos k_x + \cos k_y + \cos(k_x + k_y)], \qquad d_x = t_1[1 + \cos(k_x + k_y) + \cos k_y],$$

$$d_z = M + 2t_2 \sin\phi[\sin k_x + \sin k_y - \sin(k_x + k_y)], \quad d_y = t_1[-\sin(k_x + k_y) - \sin k_y].$$

The single-particle Hamiltonian has inversion symmetry at $M = 0$ and the 3-fold point group symmetry of the honeycomb lattice. At $M = 0$, inversion exchanges the two sublattices and transforms the annihilation operators by $(\psi_{\mathbf{k},A}, \psi_{\mathbf{k},B})^{\mathrm{T}} \to \sigma_x(\psi_{-\mathbf{k},A}, \psi_{-\mathbf{k},B})^{\mathrm{T}}$. The 3-fold rotation generates the cyclic permutation of the lattice translation vectors $\mathbf{b}_1 \to \mathbf{b}_2 \to -\mathbf{b}_1 - \mathbf{b}_2 \to \mathbf{b}_1$ on each sublattice and thus transforms the wave vectors by $(k_x, k_y) \to (k_y, -k_x - k_y)$. Therefore, the Bloch Hamiltonian has the following two symmetries:

$$h(k_x, k_y) = \sigma_x h(-k_x, -k_y)\sigma_x, \quad h(k_x, k_y) = U^\dagger(k_x, k_y) h(k_y, -k_x - k_y) U(k_x, k_y), \quad (3.1)$$

where $U(k_x, k_y)$ is a diagonal 2×2 unitary matrix, with $[1, e^{i(k_x+k_y)}]$ on the diagonal. When the system is put on the lattice of finite size $N_x \times N_y$ with periodic boundary, the 3-fold rotation symmetry is lifted, unless $N_x = N_y$.

To focus on the effect of interactions without being distracted by single-particle dispersion, we always take the flat-band limit of the insulator, i.e. replace the original Bloch Hamiltonian $h(\mathbf{k}) = \sum_n E_n(\mathbf{k}) P_n(\mathbf{k})$ by $\sum_n E_n(0) P_n(\mathbf{k})$, where $P_n(\mathbf{k})$ is the projector onto the n-th band. We then send the band gap to infinity and work directly in the lowest band, in the same spirit of the lowest Landau level projection routinely adopted in the FQH literature. We then add a density-density repulsion between nearest neighbors. Since a flattened band does not provide an energy scale, we are free to set the interaction strength to unity. After the aforementioned gauge transform on $\psi_{\mathbf{k},B}$, the interaction term can be written in the sublattice basis as

$$\frac{1}{N} \sum_{\{\mathbf{k}_i\}} \psi^\dagger_{\mathbf{k}_3 A} \psi^\dagger_{\mathbf{k}_4 B} \psi_{\mathbf{k}_2 B} \psi_{\mathbf{k}_1 A} \delta^{\mathrm{mod} 2\pi}_{\mathbf{k}_1+\mathbf{k}_2-\mathbf{k}_3-\mathbf{k}_4} V_{\mathbf{k}_1 \mathbf{k}_2 \mathbf{k}_3 \mathbf{k}_4}, \tag{3.2}$$

where

$$V_{\mathbf{k}_1 \mathbf{k}_2 \mathbf{k}_3 \mathbf{k}_4} = 1 + e^{i(\mathbf{k}_2 - \mathbf{k}_4)\mathbf{b}_2} + e^{i(\mathbf{k}_2 - \mathbf{k}_4)(\mathbf{b}_1 + \mathbf{b}_2)}, \tag{3.3}$$

as illustrated in Fig. 3.1.

3.1.1 Ground state at $1/3$ filling

We diagonalize the interacting Hamiltonian in the flattened lowest band at filling $1/3$. We show the energy spectrum of $N = 8, 10, 12$ particles on the $N_x \times N_y = 6 \times \frac{N}{2}$ lattice in Fig. 3.2. The calculations are performed with $(t_1, t_2, M, \phi) = (1, 1, 0, 0.13)$. The particular choice of parameters will be discussed later. In the three cases ($N = 8, 10, 12$), a 3-fold degenerate ground state is seen at total momenta $\{(0,0), (2,0), (4,0)\}$, $\{(1,0), (3,0), (5,0)\}$, and $\{(0,0), (0,0), (0,0)\}$, respectively. This agrees perfectly with the $(1,3)$-admissible counting proposed in Ref. [74] and recently

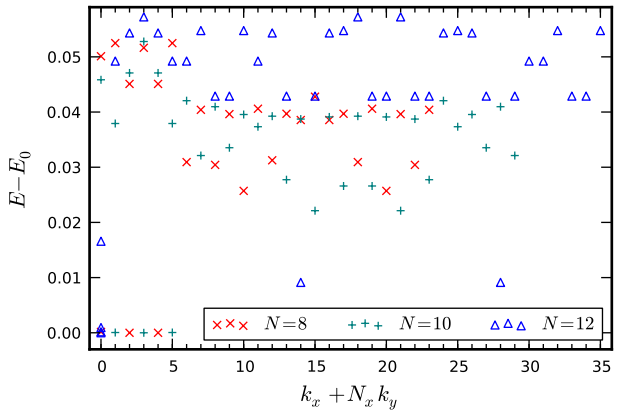

Figure 3.2: Low energy spectrum of the Haldane model with $N = 8$ (marked by red crosses), $N = 10$ (green plus signs), and $N = 12$ (blue triangles) particles on the $N_x \times N_y = 6 \times \frac{N}{2}$ lattice, with energies shifted by E_0, the lowest energy for each system size. We only show the lowest excited level in each momentum sector in addition to the 3-fold ground state.

developed in Ref. [16]. The finite-size scaling of the energy gap ΔE is shown in Fig. 3.3. The energy gap does not seem to remain open in the thermodynamic limit even if the aspect ratio N_x/N_y remains finite. Nonetheless, as discussed in the following sections, we find solid evidence for the topological nature of the ground state; the detailed investigation into the energetics will be presented in future work.

The three degenerate ground states exhibit spectral flow upon flux insertion. For example, inserting a unit flux in the x direction shifts the single particle momentum $k_x \to k_x + 2\pi\gamma_x$, with γ_x going from 0 to 1; this induces the spectral flow within the 3-fold ground state (Fig. 3.4). Upon insertion of 3 full fluxes, the 3 degenerate states restore their original configuration. Given the unit Chern number of the valence band, we conclude the system has Hall conductance $\sigma_{xy} = 1/3$.

We have also checked the effect of density-density repulsion between NNN on the 1/3 phase. Overall, this additional interaction term weakens the Laughlin-like phase. These results are in agreement with those of Sheng et al. [80] for the checkerboard model.

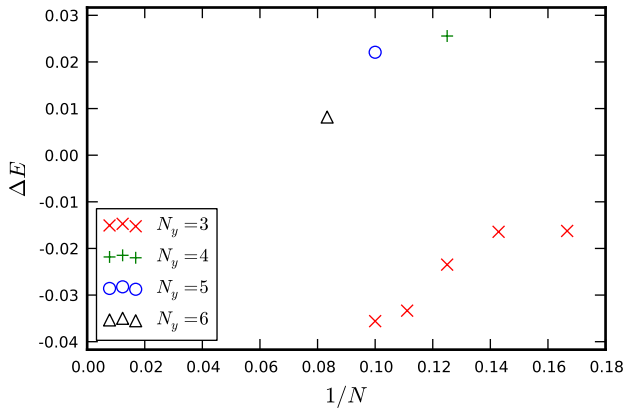

Figure 3.3: Energy gap ΔE for different system sizes and aspect ratios of the Haldane model. The gap is defined as the energy difference between the first excited state and the highest of the 3-fold ground states. A more precise definition of ΔE is given in Sec. 3.1.4. In each case, $N_x = 3N/N_y$. The negative values of ΔE in the $N_y = 3$ group mean that the actual ground state is not in the momentum sectors predicted by the theoretical counting rule, i.e. the gap above the supposed topological ground state closes.

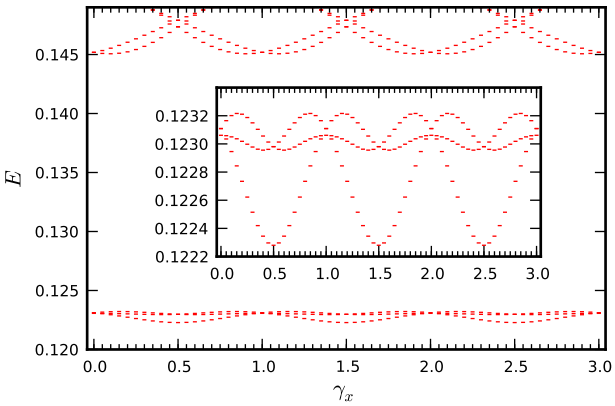

Figure 3.4: Spectral flow of the low-lying states of the Haldane model with $N = 10$ particles on the $N_x \times N_y = 6 \times 5$ lattice upon flux insertion along the x direction. γ_x counts the number of fluxes inserted. The 3-fold ground states flow into each other, and do not mix with higher states during flux insertion. It takes 3 full fluxes for the 3-fold states to return to the original configuration (inset).

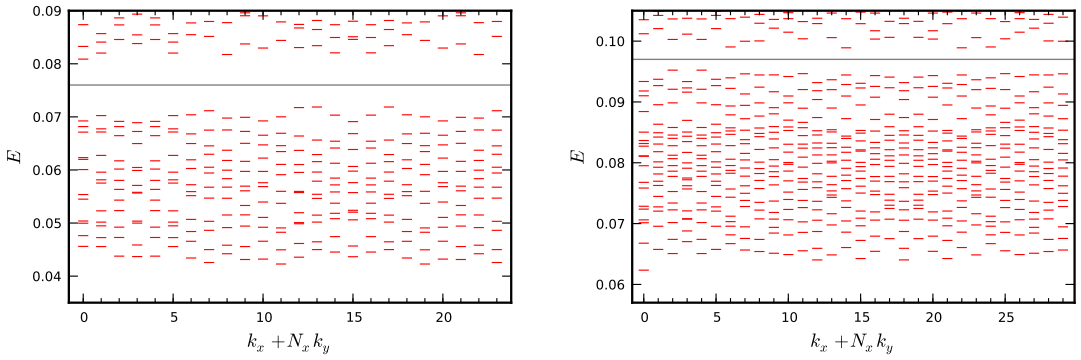

Figure 3.5: Low energy spectrum of the Haldane model at quasihole fillings. Left panel: $N = 7$ particles on 6×4 lattice, with 12 low-lying states in each momentum sector. Right panel: $N = 9$ particles on 6×5 lattice, with 19 low-lying states at $k_x = 0, 3$ and 18 elsewhere.

3.1.2 Quasihole excitations

Three-fold degeneracy alone is insufficient to fully establish the observed ground state as a FQH state; it could very well be an imprint of a lattice charge density wave. To rule out this alternative we need to study the excitations of the system. We decrease the filling ν from 1/3 and check for quasiholes in the energy spectrum. In Fig. 3.5 we show the energy spectra of $N = 7$ particles on the $N_x \times N_y = 6 \times 4$ lattice and $N = 9$ particles on the $N_x \times N_y = 6 \times 5$ lattice. (We run into convergence problems at $N = 11$.) These configurations have the same lattice geometry as the corresponding ground states shown earlier, but with one electron removed. An energy gap is clearly visible in the spectrum, and the low-energy part has the same counting in each momentum sector as predicted by the $(1, 3)$-admissible rule. This further substantiates that the ground state observed at filling 1/3 indeed has the basic features of the Laughlin FQH state [52].

3.1.3 Entanglement spectrum

Recent developments [53, 83, 20] showed that the excitations in FQH systems are manifested in the entanglement between particles [53, 108, 43, 42] in the many-body

ground state. Using this alternative probe, we provide further evidence that the ground state at filling 1/3 is a FQH Laughlin state. This tool is highly valuable in the present case since no overlap with model wave functions can be computed: despite several proposals [71, 56, 58, 93], concrete expressions for the model wave functions have not been established for FCI.

Specifically, we cut the system in the way described in Ref. [83] and further used to look at the FCIs in Ref. [74]. We divide N particles into two subsystem of N_A and N_B particles, and trace out the degrees of freedom carried by the N_B particles. The eigenvalues $e^{-\xi}$ of the resulting reduced density matrix $\rho_A = \mathrm{Tr}_B \rho = \mathrm{Tr}_B |\psi\rangle\langle\psi|$ define the particle entanglement energies ξ. For degenerate ground states, we form the density matrix as an incoherent sum with equal weights [74] $\rho = \frac{1}{3}\sum_i |\psi_i\rangle\langle\psi_i|$. Then, the entanglement energy levels ξ can be displayed in groups marked by the total momentum (k_x, k_y) of the N_A particles. A typical case is shown in Fig. 3.6. The spectrum is very similar to what was found in the checkerboard lattice model [74]. We observe a clear, although narrower, entanglement gap in the spectrum; the counting of the entanglement energy levels below the gap matches (in each momentum sector) the $(1, 3)$-admissible quasihole counting [16] of N_A particles on the $N_x \times N_y$ reciprocal lattice. We have checked all values of N_A manageable by current computers and have found perfect agreement with the counting principle in all cases. Given the vast difference between the checkerboard lattice model and the Haldane model (lattice symmetry, coordination number, flux distribution, etc.), the similarity in the entanglement spectrum is surprising. Compared with the relatively fuzzy quasihole energy spectrum, the ground state entanglement spectrum turns out to be a more reliable alternative route to probe the physics of fractional excitations.

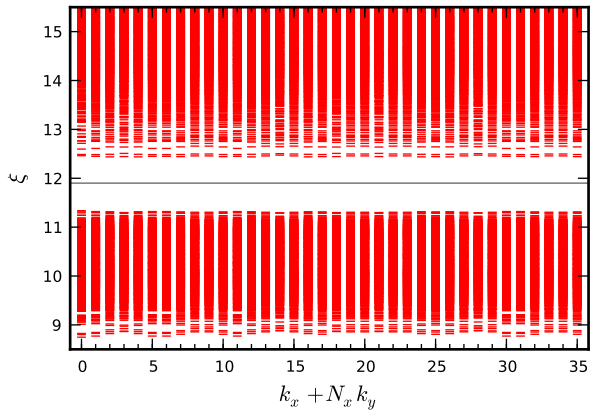

Figure 3.6: Particle entanglement spectrum of the ground state of the Haldane model of $N = 12$ particles on the $N_x \times N_y = 6 \times 6$ lattice, with $N_B = 8$ particles traced out. The number of states below the gray line is 741 in momentum sectors where both k_x and k_y are even and 728 elsewhere, in agreement with the $(1, 3)$-admissible counting rule. The system size is exactly the same as Fig. 13 of Ref. [74].

3.1.4 Parameter dependence

As analyzed by Haldane [40], strong inversion breaking eventually overcomes the non-trivial topology; the Chern number vanishes when $|M| > 3\sqrt{3}|t_2 \sin \phi|$. We now study whether strong interactions would further shrink the volume of the topologically non-trivial phase in parameter space. The density-density interaction projected to the flattened valence band has two parametric degrees of freedom $(M/t_1, t_2 \sin \phi/t_1)$, which effectively change the Berry curvature in the model. Without loss of generality, we fix $t_1 = t_2 = 1$ and study the region with $M > 0$ and $\phi \in [0, \pi/2]$. There is no clear boundary between different interacting phases in finite-size numerics. We thus need a quantitative characterization of the similarity to the ideal FCI state.

We denote the $(1, 3)$-admissible counting of N particles on the $N_x \times N_y$ lattice in momentum sector (k_x, k_y) by n_{k_x,k_y}^{N,N_x,N_y}. We denote by $\mathcal{A}$ the collection of the lowest n_{k_x,k_y}^{N,N_x,N_y} states in each momentum sector, and by $\bar{\mathcal{A}}$ the collection of all the other states. If the system is in a well-developed FCI state, the collection $\mathcal{A}$ is the 3-fold degenerate ground state, while the collection $\bar{\mathcal{A}}$ contains the excited states. The energy gap is thus $\Delta E = \min E_{\bar{\mathcal{A}}} - \max E_{\mathcal{A}}$, and the energy spread of the ground-state

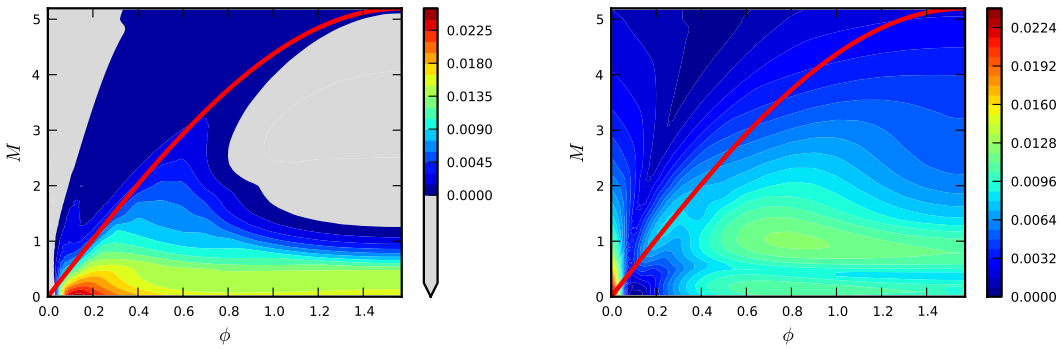

Figure 3.7: The distribution of the energy gap ΔE (left panel) and the energy spread δE (right panel) in the (ϕ, M) plane for the Haldane model of $N = 8$ particles on the $N_x \times N_y = 6 \times 4$ lattice. The region with the gap closed is marked in gray. The bold red line $M = 3\sqrt{3}\sin\phi$ separates the topologically non-trivial sector of the single-particle problem from the trivial one.

manifold can be defined as $\delta E = \max E_{\mathcal{A}} - \min E_{\mathcal{A}}$. Further, we calculate the entanglement spectra of the degenerate ground state for various partitions (N_A, N_B) of N particles. For each N_A, we denote by $\mathbb{A}$ the collection of the lowest $n_{k_x,k_y}^{N_A,N_x,N_y}$ entanglement energy levels in each momentum sector, and by $\bar{\mathbb{A}}$ all the other entanglement energy levels. We define the entanglement gap $\Delta\xi = \min \xi_{\bar{\mathbb{A}}} - \max \xi_{\mathbb{A}}$. The parameter sets with large ΔE, small δE and large $\Delta\xi$ are likely to host a FCI state.

In Figs. 3.7 and 3.8, we show the distribution of ΔE, δE, $\Delta\xi$ over the (ϕ, M) plane. Combining the three plots, we find that the region enclosed by $|M| < 3\sqrt{3}|t_2 \sin\phi|$ and $|M| \lesssim 3\sqrt{3}|t_2|(0.4 - |\sin\phi|)$ has large ΔE and $\Delta\xi$, and small δE, and hence is likely to support a FCI phase.

3.1.5 Berry curvature variation

A few authors pointed out that a Chern band shares an important feature with the Landau level [68, 62, 16]. In the limit of long wave-length and uniform Berry curvature, the projected density operators form a closed Lie algebra. This algebra has the same structure as the Girvin-MacDonald-Platzman algebra of magnetic translations [33], with the Berry curvature taking the role of the uniform magnetic field.

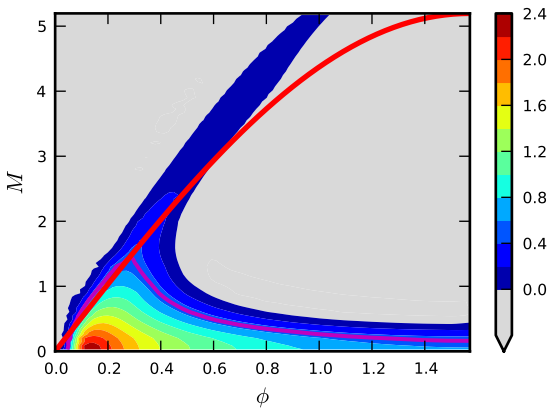

Figure 3.8: The distribution of the entanglement gap $\Delta\xi$ in the (ϕ, M) plane for the ground state of the Haldane model of $N = 8$ particles on the $N_x \times N_y = 6 \times 4$ lattice, with $N_B = 5$ particles traced out. The color code for $\Delta\xi$ is shown by the bar on the right, and the region with the gap closed is marked in gray. The average spacing of the entanglement levels below the gap is at most 0.05 (not shown in the figure); hence the entanglement gap should be considered widely open as long as $\Delta\xi \gg 0.05$. The line with $\Delta\xi = 0.5$ is shown in magenta.

They thus argued that the development of the FCI phase is driven by this algebraic structure. This picture suggests a negative correlation between Berry curvature fluctuations and the propensity towards a FCI phase. This is indeed observed in finite-size numerics, as we describe below.

We measure Berry curvature fluctuations by the simplest possible option, its standard deviation $\sigma_{\mathcal{B}}$ in units of the average Berry curvature $|\bar{\mathcal{B}}| = 1/2\pi$. The distribution of $2\pi\sigma_{\mathcal{B}}$ is shown in Fig. 3.9. Comparing this with the patterns in Figs. 3.7 and 3.8, we find a clear correlation between $\sigma_{\mathcal{B}}$ and the three measures of the propensity towards the FCI phase over the full range of the parameter scan. In particular, the optimal parameter region supporting a robust FCI phase coincides with the part of the parameter space with least fluctuating Berry curvature. While this agrees with the picture we expect from the algebraic structure [68, 62, 16, 34], we stress that the fluctuation at the optimal parameters is still quite significant, with its standard deviation comparable to the mean value. The FCI is apparently more robust to Berry

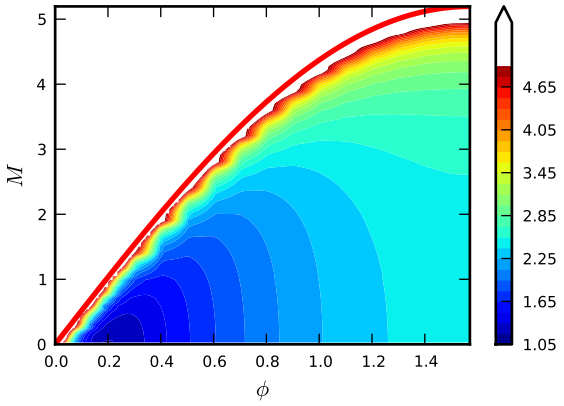

Figure 3.9: The distribution of the standard deviation of the Berry curvature $\sigma_{\mathcal{B}}$ in the (ϕ, M) plane for the Haldane model of $N = 8$ particles on the $N_x \times N_y = 6 \times 4$ lattice. The bar on the right shows the color code for the value of $2\pi\sigma_{\mathcal{B}}$. We focus on the non-trivial sector. The strong fluctuation of the Berry curvature very close to the boundary of the non-trivial sector is not shown.

curvature fluctuations than expected. This is crucial for two-band Chern insulators since their Berry curvature cannot be completely flat due to the no-hair theorem [69].

3.2 Two-orbital model

We now turn to a simpler model with two orbitals on each site of a square lattice. This model represents the spin-up half of the Mercury-Telluride two-dimensional topological insulator [15]. As shown in Fig. 3.10, there are two orbitals A, B on each site, with energy difference $2M$. The intra-orbital NN hopping has amplitude $\pm t_2$, while the inter-orbital NN hopping has amplitude $\pm it_1$ and $\pm t_1$ in the x and y directions, respectively. These amplitudes have been specifically designed such that the single-particle Bloch Hamiltonian takes the form $H = \sum_{\mathbf{k}} (\psi^\dagger_{\mathbf{k},A}, \psi^\dagger_{\mathbf{k},B}) h(\mathbf{k}) (\psi_{\mathbf{k},A}, \psi_{\mathbf{k},B})^{\mathrm{T}}$, where

$$h(\mathbf{k}) = 2t_1 \sin k_x \sigma_x + 2t_1 \sin k_y \sigma_y + [M - 2t_2(\cos k_x + \cos k_y)]\sigma_z. \tag{3.4}$$

Similar to the case of the Haldane model, we can flatten the Bloch bands using projectors. We then add Hubbard inter-orbital repulsion to each site, as shown in

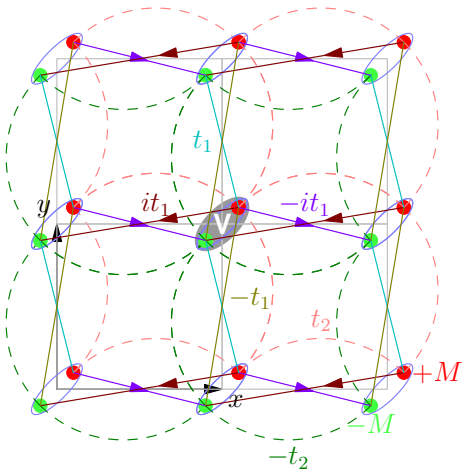

Figure 3.10: The two-orbital model on square lattice. The two orbitals A,B are colored in red and green, respectively. The intra-orbital NN hopping amplitude is t_2 between the A orbitals, and $-t_2$ between the B orbitals. The inter-orbital NN hopping amplitude is $\pm it_1$ in the x direction along the arrows, and $\pm t_1$ in the y direction. The on-site Hubbard repulsion is depicted by the ellipse in gray.

Fig. 3.10. In momentum space, the interaction term reads

$$\frac{1}{N}\sum_{\{\mathbf{k}_i\}}\delta^{\mathrm{mod}2\pi}_{\mathbf{k}_1+\mathbf{k}_2-\mathbf{k}_3-\mathbf{k}_4}\psi^\dagger_{\mathbf{k}_3 A}\psi^\dagger_{\mathbf{k}_4 B}\psi_{\mathbf{k}_2 B}\psi_{\mathbf{k}_1 A}. \tag{3.5}$$

Even though at single-particle level a two-orbital-per-site model is equivalent to a model with two sites in each unit cell, this situation changes when interactions are included. Notice that the interaction here (Eq. 3.5) has a different form factor than the one in Eq. 3.3.

We diagonalize the interacting Hamiltonian in the flattened lowest band at filling 1/3 and $(t_2/t_1, M/t_1) = (1, 2)$. We show the energy spectrum of $N = 8, 10$ particles on the $N_x \times N_y = 6 \times \frac{N}{2}$ lattice in Fig. 3.11. (We run into serious convergence problems at $N = 12$.) In the two cases ($N = 8, 10$), a 3-fold degenerate ground state is seen at total momenta $\{(0,0),(2,0),(4,0)\}$ and $\{(1,0),(3,0),(5,0)\}$, respectively. This agrees perfectly with the $(1,3)$-admissible counting proposed in Ref. [74, 16]. As shown in Fig. 3.12, the energy gap ΔE remains open and scales to a finite value in the limit of $N \to \infty$ with N_x/N_y finite. The three degenerate ground states exhibit spectral flow upon flux insertion with a period of 3 fluxes (see Fig. 3.13). This shows

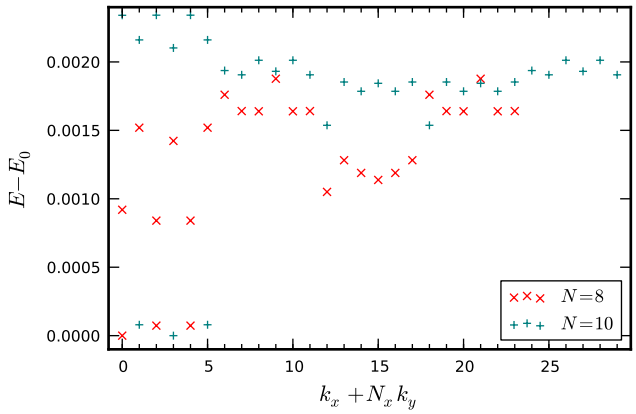

Figure 3.11: Low energy spectrum of two-orbital model for $N = 8$ (marked by red crosses) and $N = 10$ (green plus signs) particles on $(N_x, N_y) = (6, N/2)$ lattice, with energies shifted by E_0, the lowest energy for each system size. We only show the lowest excited level in each momentum sector in addition to the 3-fold ground state.

that the system has Hall conductance $\sigma_{xy} = 1/3$. We study the quasihole excitations through ground state entanglement. In Fig. 3.14, we observe an entanglement gap in the spectrum. The counting of the entanglement energy levels below the gap again matches in each momentum sector the $(1, 3)$-admissible counting. This shows that the excitations in the ground state of the two-orbital model have the same counting as that of Abelian fractional statistics 1/3 quasiholes. We thus conclude that the ground state is a FQH Laughlin state.

The two-orbital model has topologically non-trivial bands when $|M| < 4|t_2|$. We now move the system away from the point $(t_2, M) = (1, 2)$ and probe this parameter region. In Figs. 3.15 and 3.16, we display the distribution of the energy gap ΔE, the energy spread δE, and the entanglement gap $\Delta\xi$ of the ground state. Compared with the Haldane model, the situation is more complicated. The maximum of the energy gap ΔE does not coincide with the minimum of the energy spread δE. Rather, the region with large gap ΔE tends to have large spread δE as well. The peak of the entanglement gap $\Delta\xi$ is close neither to the maximum of ΔE nor to the minimum of δE. Varying (M, t_2) scans over the manifold of the two-orbital interacting Hamiltonians projected to the lowest band. The lack of correlation between ΔE, δE

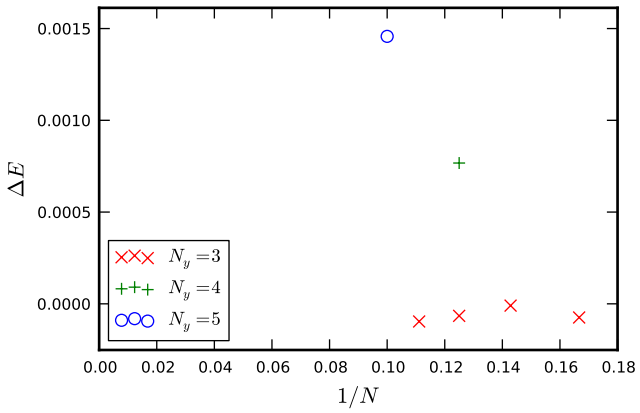

Figure 3.12: Energy gap ΔE of the two-orbital model for different system sizes and aspect ratios. In each case, $N_x = 3N/N_y$. The negative values of ΔE in the $N_y = 3$ group mean that the actual ground state is not in the momentum sectors predicted by the theoretical counting rule.

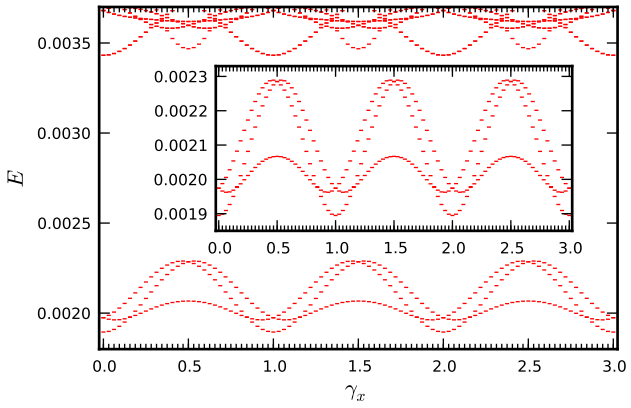

Figure 3.13: Spectral flow of the low-lying states of the two-orbital model with $N = 10$ particles on the $N_x \times N_y = 6 \times 5$ lattice upon flux insertion along the x direction. γ_x counts the number of fluxes inserted. The 3-fold ground states flow into each other, and do not mix with higher states during flux insertion. It takes 3 full fluxes for the 3-fold states to return to the original configuration (inset).

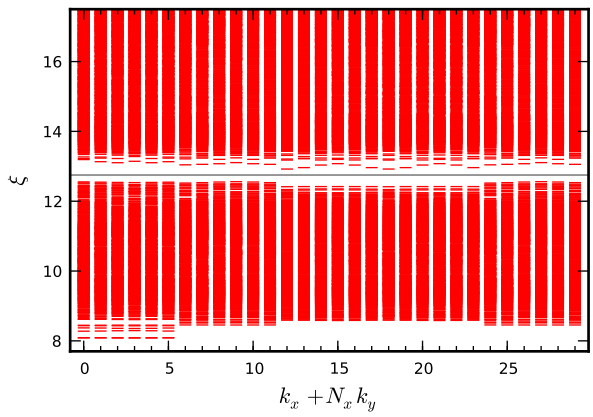

Figure 3.14: Particle entanglement spectrum of the ground state of the two-orbital model of $N = 10$ particles on the $N_x \times N_y = 6 \times 5$ lattice, with $N_B = 5$ particles traced out. The number of states below the gray line is 776 in momentum sectors with $k_y = 0$ and 775 in all the other sectors, in agreement with the analytical counting rule.

and $\Delta\xi$ suggests that the distance from this manifold of Hamiltonians to the Laughlin model Hamiltonian is quite large. Further, we check the correlation between Berry curvature fluctuations and the propensity towards the FCI phase. The variation of the curvature fluctuation is shown in Fig. 3.17. We observe weak correlation between $\sigma_{\mathcal{B}}$ and δE and find little association between $\sigma_{\mathcal{B}}$ and ΔE or $\Delta\xi$. It is possible that $\sigma_{\mathcal{B}}$ is not a very good measure of the Berry curvature fluctuation. We note that in this model the interaction before projection is constant. We leave in-depth study of this issue for future work.

3.3 Kagome lattice model

We study the Kagome lattice model built by Tang et al. [88]. As shown in Fig. 3.18, the lattice is spanned by the translation vectors $\mathbf{b}_1$ and $\mathbf{b}_2$, and it consists of three sublattices A,B,C. In Ref. [88], the single-particle model has been studied both without and with NNN hopping terms. We have looked at the effect of interactions in both cases. But for sake of simplicity we focus mostly on the case without NNN hoppings.

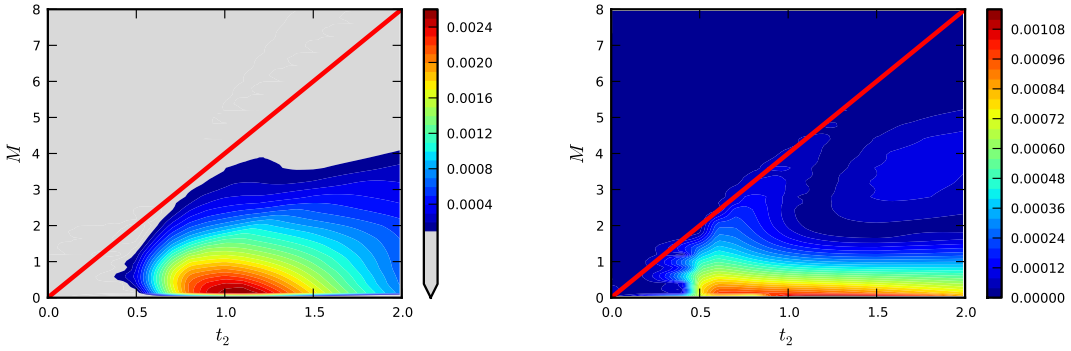

Figure 3.15: The distribution of the energy gap ΔE (left panel) and the energy spread (right panel) in the (t_2, M) plane for the two-orbital model of $N = 8$ particles on the $N_x \times N_y = 6 \times 4$ lattice. The region with the gap closed is marked in gray. The bold red line $M = 4t_2$ separates the topologically non-trivial sector of the single-particle problem from the trivial one.

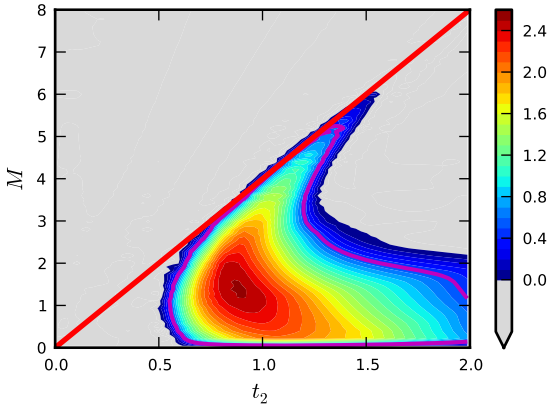

Figure 3.16: The distribution of the entanglement gap $\Delta\xi$ in the (t_2, M) plane for the ground state of the two-orbital model of $N = 8$ particles on the $N_x \times N_y = 6 \times 4$ lattice, with $N_B = 5$ particles traced out. The color code for $\Delta\xi$ is shown by the bar on the right, and the region with the gap closed is marked in gray. The average spacing of the entanglement levels below the gap is at most 0.05 (not shown in the figure); hence the entanglement gap should be considered widely open as long as $\Delta\xi \gg 0.05$. The line with $\Delta\xi = 0.5$ is shown in magenta. The bold red line $M = 4t_2$ separates the topologically non-trivial sector of the single-particle problem from the trivial one.

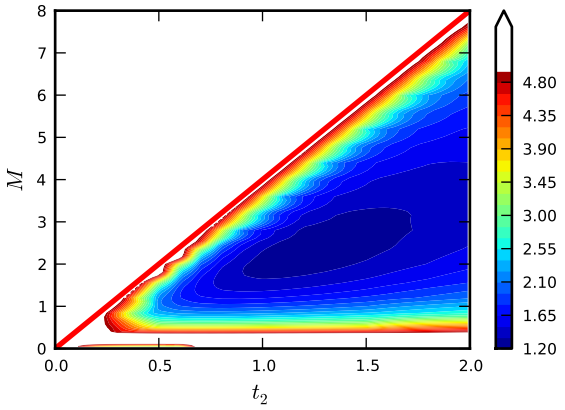

Figure 3.17: The distribution of the standard deviation of the Berry curvature $\sigma_{\mathcal{B}}$ in the (t_2, M) plane for the two-orbital model of $N = 8$ particles on the $N_x \times N_y = 6 \times 4$ lattice. The bar on the right shows the color code for the value of $2\pi\sigma_{\mathcal{B}}$. The bold red line $M = 4t_2$ separates the topologically non-trivial sector of the single-particle problem from the trivial one. We focus on the non-trivial sector. The strong fluctuation of the Berry curvature very close to the boundary of the non-trivial sector is not shown.

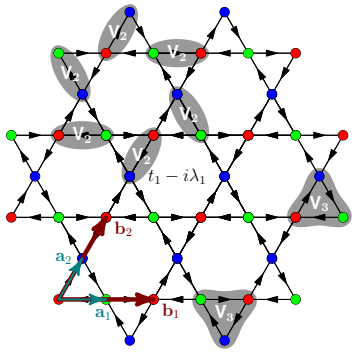

Figure 3.18: The Kagome lattice model with NN spin-orbit coupling. The three sublattices A,B,C are colored in red, green, blue, respectively. The lattice translation vectors are $\mathbf{b}_1 = 2\mathbf{a}_1$, $\mathbf{b}_2 = 2\mathbf{a}_2$. The hopping amplitude between NN is $t_1 - i\lambda_1$ in the direction of arrows. The two-body and the three-body interactions between NN are illustrated by the gray ellipses and triangles, respectively.

The hopping amplitude between NN is $t_1 \pm i\lambda_1$. After a Fourier transform and a gauge transform $\psi_{\mathbf{k},B} \to \psi_{\mathbf{k},B} e^{-i\mathbf{k}\cdot\mathbf{b}_1/2}$, $\psi_{\mathbf{k},C} \to \psi_{\mathbf{k},C} e^{-i\mathbf{k}\cdot\mathbf{b}_2/2}$, the single-particle Hamiltonian can be cast in Bloch form as $H = \sum_{\mathbf{k}} (\psi^\dagger_{\mathbf{k},A}, \psi^\dagger_{\mathbf{k},B}, \psi^\dagger_{\mathbf{k},C}) h(\mathbf{k}) (\psi_{\mathbf{k},A}, \psi_{\mathbf{k},B}, \psi_{\mathbf{k},C})^{\mathrm{T}}$. Here the lattice momentum $\mathbf{k} = (\mathbf{k}\cdot\mathbf{b}_1, \mathbf{k}\cdot\mathbf{b}_2) \equiv (k_x, k_y)$ is summed over the first Brillouin zone, and the $h(\mathbf{k})$ matrix reads

$$h(\mathbf{k}) = -t_1 \begin{bmatrix} 0 & & \text{h.c.} \\ 1+e^{ik_x} & 0 & \\ 1+e^{ik_y} & 1+e^{i(k_y-k_x)} & 0 \end{bmatrix} + i\lambda_1 \begin{bmatrix} 0 & & \text{h.c.} \\ -1-e^{ik_x} & 0 & \\ 1+e^{ik_y} & -1-e^{i(k_y-k_x)} & 0 \end{bmatrix}.$$

The three Bloch bands can be flattened using the projector method detailed for the Haldane model in Sec. 3.1. We focus on the lowest band. Unless specified otherwise, the numerical calculations shown below are performed at $\lambda_1 = t_1$ as discussed in the original paper [88]. The lowest band has unit Chern number.

3.3.1 Filling 1/3

We fill the flattened lowest band to filling 1/3, and add density-density repulsion between NN. After the gauge transform, the interaction term reads

$$\frac{1}{N} \sum_{\{\mathbf{k}_i\}} \delta^{\mathrm{mod}2\pi}_{\mathbf{k}_1+\mathbf{k}_2-\mathbf{k}_3-\mathbf{k}_4} \sum_{\alpha<\beta}^{A,B,C} \psi^\dagger_{\mathbf{k}_3\alpha} \psi^\dagger_{\mathbf{k}_4\beta} \psi_{\mathbf{k}_2\beta} \psi_{\mathbf{k}_1\alpha} V^{\alpha\beta}_{\mathbf{k}_1\mathbf{k}_2\mathbf{k}_3\mathbf{k}_4}, \tag{3.6}$$

where the sublattice indices (α, β) are summed over (A, B), (B, C), (C, A), and the interaction factors are $V^{AB}_{\mathbf{k}_1\mathbf{k}_2\mathbf{k}_3\mathbf{k}_4} = 1+e^{-i(\mathbf{k}_2-\mathbf{k}_4)\cdot\mathbf{b}_1}$, $V^{BC}_{\mathbf{k}_1\mathbf{k}_2\mathbf{k}_3\mathbf{k}_4} = 1+e^{i(\mathbf{k}_2-\mathbf{k}_4)\cdot(\mathbf{b}_1-\mathbf{b}_2)}$, and $V^{CA}_{\mathbf{k}_1\mathbf{k}_2\mathbf{k}_3\mathbf{k}_4} = 1+e^{i(\mathbf{k}_2-\mathbf{k}_4)\cdot\mathbf{b}_2}$. The 6 terms are illustrated by the 6 ellipses in Fig. 3.18.

We show the energy spectrum of $N = 8, 10, 12$ particles on the $N_x \times N_y = 6 \times \frac{N}{2}$ lattice in Fig. 3.19. In the three cases, a 3-fold degenerate ground state is seen at total momenta $\{(0,0),(2,0),(4,0)\}$, $\{(1,0),(3,0),(5,0)\}$, $\{(0,0),(0,0),(0,0)\}$, respectively. Again, this agrees perfectly with the $(1,3)$-admissible counting proposed in Ref. [74, 16]. The ratio of the gap to the energy spread of the ground-state manifold is larger than that of the Haldane model. As shown in Fig. 3.20, the energy gap ΔE

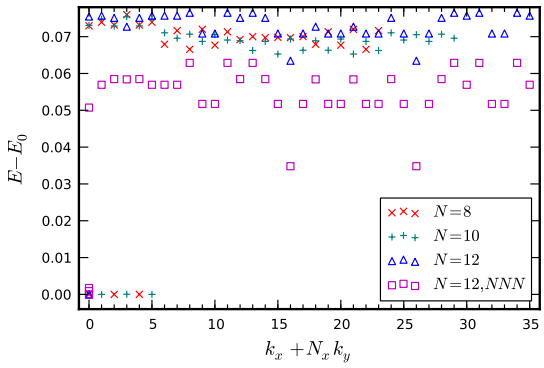

Figure 3.19: Low energy spectrum of the Kagome lattice model with $N = 8$ (marked by red crosses), $N = 10$ (green plus signs), and $N = 12$ (blue triangles) particles on the $N_x \times N_y = 6 \times N/2$ lattice, with energies shifted by E_0, the lowest energy for each system size. Also shown (magenta squares) is the spectrum of $N = 12$ particles on the $N_x \times N_y = 6 \times 6$ lattice in the alternative Kagome model with NNN hoppings at the parameters suggested in the original paper [88], namely $(\lambda_1, \lambda_2, t_2) = (0.28, 0.2, -0.3)$.

remains open and scales to a finite value in the limit of $N \to \infty$ with N_x/N_y finite. And the three degenerate ground states exhibit spectral flow upon flux insertion. The period of 3 fluxes, shown in Fig. 3.21, indicates the system has Hall conductance $\sigma_{xy} = 1/3$.

We probe the quasihole excitations by the particle entanglement spectrum of the ground state. In Fig. 3.22, we observe a clear, *very large* entanglement gap in the spectrum, and the counting of the entanglement energy levels below the gap again matches in each momentum sector the $(1, 3)$-admissible counting [74, 16]. The width of the entanglement gap is $\Delta\xi = 4.64$. This means that in the ground state of the Kagome lattice model, the inter-particle correlations that obey the $(1, 3)$ generalized Pauli principle is stronger than any other correlations *by two orders of magnitude!* We thus conclude that the ground state is a FCI state with characteristics of the FQH Laughlin state.

Now we briefly address the issue of parameter dependence. Without loss of generality, we fix $t_1 = 1$ and vary λ_1 in the range $(0, \sqrt{3})$. In this region, the single-particle spectrum is gapped and the lowest band has unit Chern number [88]. A strong cor-

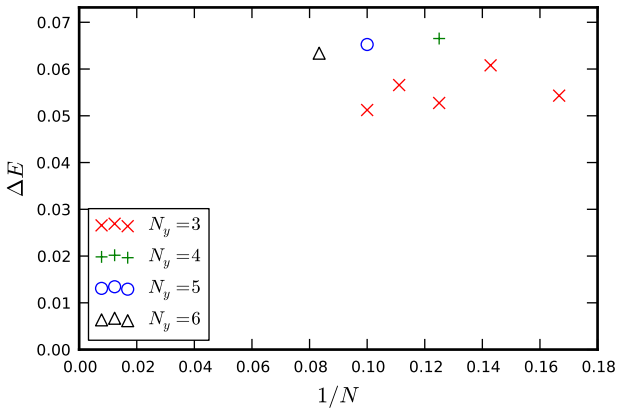

Figure 3.20: Energy gap ΔE of the Kagome lattice model for different system sizes and aspect ratios. In each case, $N_x = 3N/N_y$.

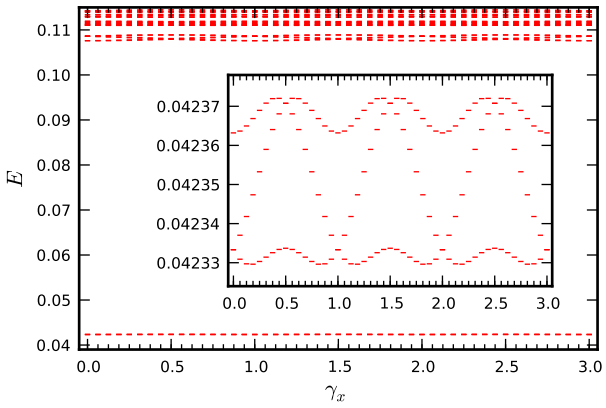

Figure 3.21: Spectral flow of the low-lying states of the Kagome lattice model with $N = 10$ particles on the $N_x \times N_y = 6 \times 5$ lattice upon flux insertion along the x direction. γ_x counts the number of fluxes inserted. The 3-fold ground states flow into each other, and do not mix with higher states during flux insertion. It takes 3 full fluxes for the 3-fold states to return to the original configuration (inset).

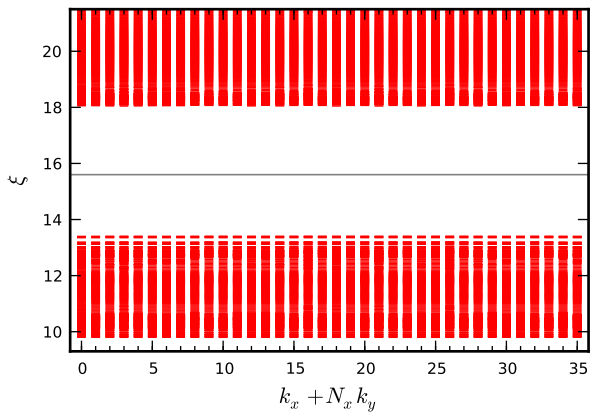

Figure 3.22: Particle entanglement spectrum of the ground state of the Kagome lattice model of $N = 12$ particles on the $N_x \times N_y = 6 \times 6$ lattice, with $N_B = 7$ particles traced out. The number of states below the gray line is 2530 in each momentum sector, in agreement with the $(1, 3)$-admissible counting rule. The width of the entanglement gap is $\Delta\xi = 4.64$, meaning that spurious, non-FQH correlations have a probability of $e^{-4.64} \approx 0.0097$ relative to the universal ones.

relation between the energy gap ΔE and the Berry curvature fluctuation $2\pi\sigma_{\mathcal{B}}$ on λ_1 is clearly visible in Fig. 3.23.

As a sanity check, we have also looked at the case where one partially fills the second band. We assume the lowest band is completely filled and inert, and diagonalize the second band directly. In such a situation, there is no evidence for Laughlin-like physics at filling $1 + 1/3$. This is expected since the second band has zero Chern number [88].

In Ref. [88], it was shown that by adding properly chosen NNN hopping terms, the band gap to bandwidth ratio can be enhanced by more than an order of magnitude, and it was argued that this alternative model could support a more robust Laughlin-like phase when interactions are added. Unfortunately, we observe the opposite effect: compared with the simple model with only NN hoppings, both the energy gap and the entanglement gap are only about half as large for the two cases with NNN hoppings studied in Ref. [88]. The reduction of $\Delta\xi$ from 4.64 to 1.95 means the relative strength of the $(1, 3)$ Pauli principle exclusion is reduced by a factor of ~ 15. The energy and the entanglement spectra for the case with the largest band gap to bandwidth ratio

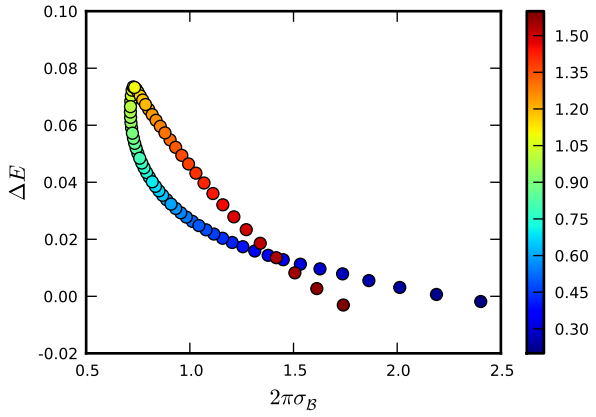

Figure 3.23: The correlation between the standard deviation $\sigma_{\mathcal{B}}$ of Berry curvature and the gap ΔE in the energy spectrum of 8 particles on the $N_x \times N_y = 6 \times 4$ lattice. The calculations are performed at $t_1 = 1$. The color of each scatter point encodes the value of λ_1 per the color bar to the right. A negative correlation between $\sigma_{\mathcal{B}}$ and ΔE is visible.

[at $(\lambda_1, \lambda_2, t_2) = (0.28, 0.2, -0.3)$] are shown in Figs. 3.19 and 3.24. We have checked the nearby parameter region and no qualitative change is observed. Carefully tuning the NNN hoppings could achieve $\sim 10\%$ flatter Berry curvature, but the energy gap and the entanglement gap still end up smaller than the simple model with only NN hoppings, showing that the flat Berry curvature – FQH phase correspondence is to be taken as a general trend, rather than a quantitative result.

3.3.2 Half filling

Among the FQH phases, the Moore-Read (MR) state plays a special role. It is one of the best candidates to explain the experimentally observed fraction $\nu = 5/2$ and its excitations obey non-Abelian statistics. The $\mathbb{Z}_n$ Read-Rezayi (RR) states are the generalization of Laughlin ($n = 1$) and MR ($n = 2$) states. They occur at a filling factor $\nu = n/(n+2)$. The $\mathbb{Z}_3$ RR state is a potential candidate to explain the fraction $\nu = 12/5$.

It has been recently shown that a $(n+1)$-body short-range interaction can stabilize the analogue of a $\mathbb{Z}_n$ RR state on the checkerboard lattice [16]. The $(n+1)$-body

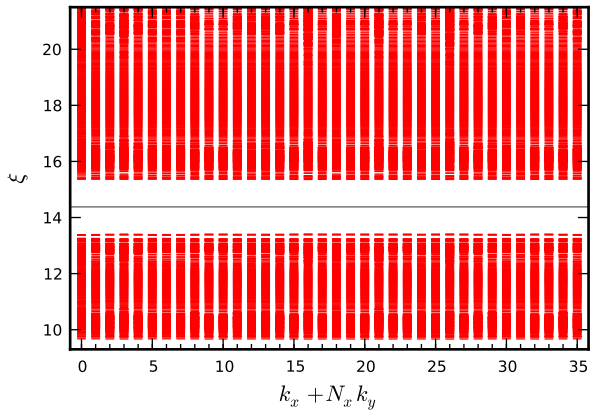

Figure 3.24: Particle entanglement spectrum of the ground state of the Kagome lattice model with NNN hoppings of $N = 12$ particles on the $N_x \times N_y = 6 \times 6$ lattice at $(\lambda_1, \lambda_2, t_2) = (0.28, 0.2, -0.3)$, with $N_B = 7$ particles traced out. The number of states below the gray line is 2530 in each momentum sector, in agreement with the $(1, 3)$ counting rule. The width of the entanglement gap is $\Delta\xi = 1.95$, much smaller than the gap of the model with only NN hoppings shown in Fig. 3.22.

interaction used in Ref. [16] mimics the short range interaction for which the $\mathbb{Z}_n$ RR state is the exact zero-energy ground state with highest density. It has also been very recently demonstrated [96] that the Haldane model of hard-core bosons exhibits a MR state at filling $\nu = 1$. The three-body hard-core repulsion in that case was implemented by restricting the occupancy of any site to be less than three.

In this section, we focus on the half-filling case and thus on the fermionic MR state. Until now, we have found no evidence that a two-body NN interaction could stabilize a MR-like state in any of the lattice models studied. Instead of the two-body NN repulsion, we add to the Kagome lattice model a *three*-body NN repulsion similar to the one in Ref. [16], as shown by the gray triangles in Fig. 3.18. After the gauge transform, the density-density-density interaction term reads

$$\frac{1}{N}\sum_{\{\mathbf{k}_i\}} \delta^{\mathrm{mod}2\pi}_{\substack{\mathbf{k}_1+\mathbf{k}_2+\mathbf{k}_3 \\ -\mathbf{k}_4-\mathbf{k}_4-\mathbf{k}_6}} \psi^\dagger_{\mathbf{k}_4 A}\psi^\dagger_{\mathbf{k}_5 B}\psi^\dagger_{\mathbf{k}_6 C}\psi_{\mathbf{k}_3 C}\psi_{\mathbf{k}_2 B}\psi_{\mathbf{k}_1 A} \times V_{\mathbf{k}_1\mathbf{k}_2\mathbf{k}_3\mathbf{k}_4\mathbf{k}_5\mathbf{k}_6}, \tag{3.7}$$

where

$$V_{\mathbf{k}_1\mathbf{k}_2\mathbf{k}_3\mathbf{k}_4\mathbf{k}_5\mathbf{k}_6} = 1 + e^{-i(\mathbf{k}_2-\mathbf{k}_5)\cdot\mathbf{b}_1 - i(\mathbf{k}_3-\mathbf{k}_6)\cdot\mathbf{b}_2}. \tag{3.8}$$

It is well known that a short-range three-body repulsion stabilizes the Pfaffian MR FQH state [60] in a half-filled Landau level [35]. We therefore expect an analogous FCI phase appearing at half filling. The MR FQH state has fractional excitations governed by the generalized Pauli principle of having no more than 2 particles in 4 consecutive Landau level orbitals and the fermionic statistics of no more than one particle allowed per orbital [12, 13]. This enables a direct extension of the $(1,3)$-admissible FCI counting of having no more than 1 particle in 3 consecutive orbitals [74] to a $(2,4)$-admissible counting [16] for the possible MR FCI state.

We diagonalize the interacting Hamiltonian in the flattened lowest band at filling 1/2. We show the energy spectrum of $N = 8, 10, 12$ particles on the $N_x \times N_y = \frac{N}{2} \times 4$ lattice in Fig. 3.25. In the three cases, a 6-fold degenerate ground state is seen at total momenta $\{6 \times (0,0)\}$, $\{(0,0), 2 \times (0,1), (0,2), 2 \times (0,3)\}$, $\{2 \times (0,0), 4 \times (0,2)\}$, respectively. This agrees exactly with the $(2,4)$-admissible counting proposed above. As shown in Fig. 3.26, the energy gap ΔE remains open and scales to a finite value in the limit of $N \to \infty$ with N_x/N_y finite. The six degenerate ground states exhibit spectral flow upon flux insertion. As shown in Fig. 3.27, the period of the spectral flow is 2 fluxes, and therefore the ground state has Hall conductance $\sigma_{xy} = 1/2$.

We probe the quasihole excitations by using the particle entanglement spectrum of the ground state. In Fig. 3.28, we observe a clear and large gap in the entanglement spectrum, and the counting of the entanglement energy levels below the gap again matches in each momentum sector the $(2,4)$-admissible counting as predicted in Ref. [16]. The width of the entanglement gap is $\Delta\xi = 1.66$. This indicates that the inter-electron correlations that obey the $(2,4)$ generalized Pauli principle, i.e. the pairing of electrons, is 5 times stronger than any other kind of correlations. Therefore, we conclude that the ground state of the Kagome lattice model with the three-body NN interactions at half filling is indeed a MR FQH state.

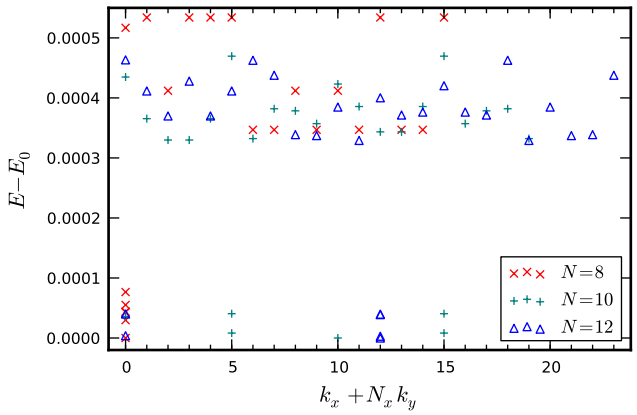

Figure 3.25: Low energy spectrum of the Kagome lattice model with three-body interactions of $N = 8$ (marked by red crosses), $N = 10$ (green plus signs), and $N = 12$ (blue triangles) particles on the $N_x \times N_y = \frac{N}{2} \times 4$ lattice, with energies shifted by E_0, the lowest energy for each system size. We only show the lowest excited level in each momentum sector in addition to the 6-fold ground state.

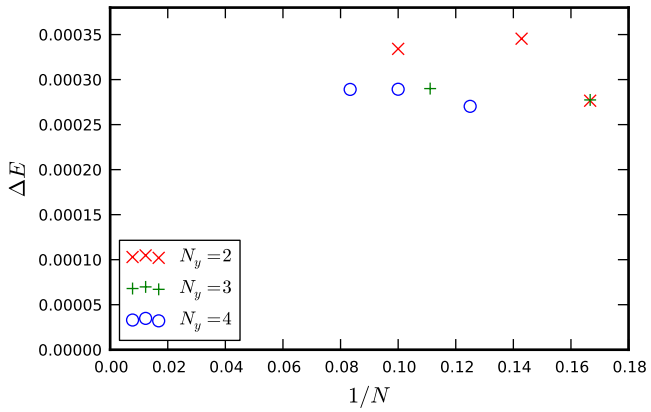

Figure 3.26: Energy gap ΔE of the Kagome lattice model with three-body interactions for different system sizes and aspect ratios. In each case, $N_x = 2N/N_y$.

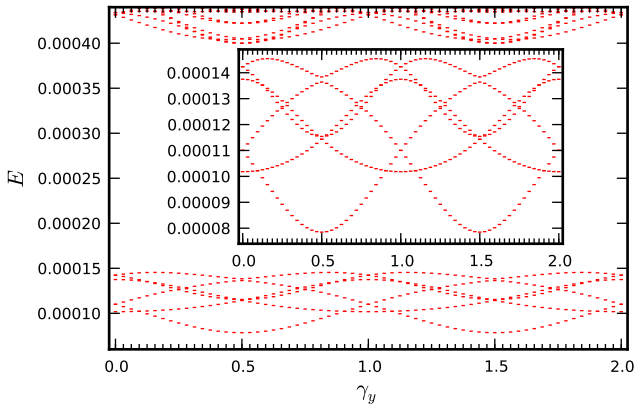

Figure 3.27: Spectral flow of the low-lying states of the Kagome lattice model with three-body interaction of $N = 10$ particles on the $N_x \times N_y = 5 \times 4$ lattice upon flux insertion along the y direction. γ_y counts the number of fluxes inserted. The 6-fold ground states flow into each other, and do not mix with higher states during flux insertion. After insertion of every 2 full fluxes, the 6-fold states return to the original configuration (inset).

Based on the results at filling 1/3 and 1/2, we make the conjecture that *under desirable conditions*, a short-range $(n+1)$-body interaction could stabilize $\mathbb{Z}_n$ RR parafermion FQH state [73] in a Chern band at filling $n/(n+2)$. Further work is needed to confirm the cases $n \geq 3$. The $n = 3$ case has recently been reported in Ref. [16].

We have also looked for a MR phase in the Haldane and two-orbital models using three-body interactions. Unfortunately, these two models do not seem to exhibit such a phase. This appears to be consistent with the more fragile Laughlin-like phase in these models.

3.4 Ruby lattice model

The last Chern insulator we have analyzed is on a ruby lattice. Hu et al. [45] have considered a two-dimensional ruby lattice with strong spin-orbit coupling. The simplified spin-polarized version of this model was shown to provide a Chern insulator with an extremely flat lowest band.

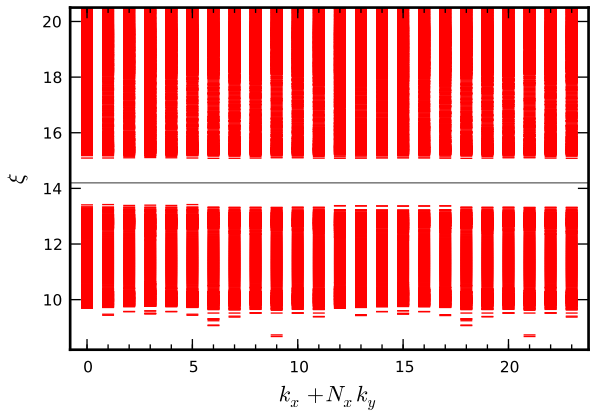

Figure 3.28: Particle entanglement spectrum of the ground state of the Kagome lattice model with three-body interactions of $N = 12$ particles on the $N_x \times N_y = 6 \times 4$ lattice, with $N_B = 6$ particles traced out. The number of states below the gray line is 2910 in momentum sectors with $k_x = 1, 3$ and $k_y = 0, 2$, 2912 in sectors $(0, 0)$ and $(0, 2)$, 2940 in sectors with $k_x = 5$ and sectors with $k_x = 2, 4$ and $k_y = 2, 4$, and 2944 in all the other sectors, in agreement with the $(2, 4)$-admissible counting rule. The width of the entanglement gap is $\Delta\xi = 1.66$.

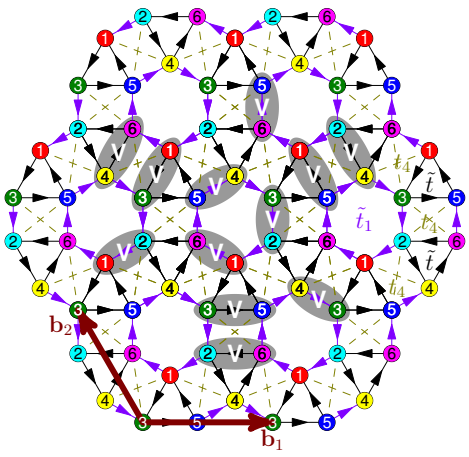

Figure 3.29: The Ruby lattice model. The six sublattices 1 to 6 are colored respectively in red, cyan, green, yellow, blue and magenta. The lattice translation vectors are $\mathbf{b}_1$, $\mathbf{b}_2$. The complex hopping parameters between NN are $\tilde{t} = t_r + it_i$ for sites having the same parity (black arrows) and $\tilde{t}_1 = t_{1r} + it_{1i}$ for sites having opposite parity (purple arrows), both in the direction of the arrows. The real hopping parameter on the diagonal of the square (olive dashed lines) is given by t_4. The density-density repulsion between NN is depicted by gray ellipses.

As depicted in Fig. 3.29, the ruby lattice is spanned by the translation vectors $\mathbf{b}_1$ and $\mathbf{b}_2$ and it is made of six sublattices, denoted from 1 to 6. After a Fourier transform and a trivial gauge transform, the single-particle Hamiltonian can be cast in Bloch form as

$$H = \sum_{\mathbf{k}} \sum_{i,j=1}^{6} \Psi^{\dagger}_{\mathbf{k},i} h_{i,j}\left(\mathbf{k}\right) \Psi_{\mathbf{k},j}. \tag{3.9}$$

Here the lattice momentum $\mathbf{k} = (\mathbf{k}\cdot\mathbf{b}_1, \mathbf{k}\cdot\mathbf{b}_2) \equiv (k_x, k_y)$ is summed over the first Brillouin zone, and the $h(\mathbf{k})$ matrix is given by

$$h(\mathbf{k}) = -\begin{bmatrix} 0 & & & & & \\ \tilde{t}_1^* & 0 & & & \text{h.c.} & \\ \tilde{t} & \tilde{t}_1^* s_x^{-1} s_y^{-1} & 0 & & & \\ t_4(1+s_x) & \tilde{t} & \tilde{t}_1^* s_x & 0 & & \\ \tilde{t}^* & t_4(1+\frac{1}{s_x s_y}) & \tilde{t} & \tilde{t}_1^* & 0 & \\ \tilde{t}_1 s_x & \tilde{t}^* & t_4 s_x(1+s_y) & \tilde{t} & \tilde{t}_1^* s_x s_y & 0 \end{bmatrix}, \tag{3.10}$$

with $s_x = e^{ik_x}$ and $s_y = e^{ik_y}$.

We adopt the parameter values suggested in the original article [45], namely $(t_i, t_{1r}, t_{1i}, t_4) = (1.2, -1.2, 2.6, -1.2)t_r$. For these parameters, the lowest band of the problem is gapped, and has unit Chern number [45].

Again, we flatten the Bloch bands using projectors, and we add density-density repulsion of unit strength between nearest neighbors. There are 12 type of terms as depicted by the gray ellipses in Fig. 3.29. We diagonalize the interacting Hamiltonian in the flattened lowest band at filling 1/3 with up to $N = 12$ particles, and find results quite similar to the previous three models. Namely, we find a 3-fold degenerate ground state in the momentum sectors predicted by the $(1, 3)$ counting principle. The degenerate ground state is separated from the excitations by a finite energy gap. Finite-size scaling indicates that the gap remains open in the thermodynamic limit. Twisting boundary drives spectral flow within the ground-state manifold and the flow

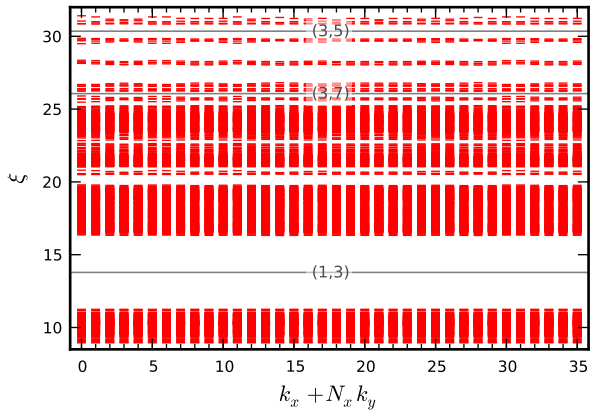

Figure 3.30: Particle entanglement spectrum of the ground state of the ruby lattice model of $N = 12$ particles on the $N_x \times N_y = 6 \times 6$ lattice, with $N_B = 8$ particles traced out. The number of states below each of the three gray lines is $741, 1629, 1645$ in momentum sectors where both k_x and k_y are even and $728, 1612, 1628$ elsewhere. These numbers are in perfect accordance with the $(1,3)$-, $(3,7)$-, and $(3,5)$-admissible counting, respectively. The width of the $(1,3)$ entanglement gap is $\Delta\xi = 5.07$. The counting of levels below the unmarked gaps do not correspond to any (k,r)-admissible rule.

has a period of 3 fluxes. Hence, the system has Hall conductance $\sigma_{xy} = 1/3$. We calculate the entanglement spectra for various system sizes and find an entanglement gap with the $(1,3)$-admissible counting in each case. As an example, we show in Fig. 3.30 the entanglement spectrum of the ground state of $N = 12$ particles. The entanglement gap $\Delta\xi = 5.07$ is comparable to, although slightly smaller than the entanglement gap $\Delta\xi = 5.53$ of the Kagome lattice model with only NN hoppings at the same system size. This pronounced sign of exclusion statistics counting suggests that the system has fractional excitations similar to the Laughlin quasiholes. We do however stress that we have *not* computed the statistics of the quasiholes, as this would require braiding operations likely to be plagued by finite-size effects on the lattices we can reach by computers. We conclude that the ground state of the ruby lattice model with two-body NN repulsions is a FQH Laughlin state.

We have also checked the effect of three-body NN repulsions at half filling. There are a total of 14 terms, corresponding to 2 equilateral triangles and 12 right triangles

embedded in rectangles. Similar to the case of the Kagome lattice model detailed in Sec. 3.3.2, we find a robust MR state here. The state has the hallmark 6-fold degenerate gapped ground state at the correct momenta. We also find a large entanglement gap corresponding to fractional excitations governed by the $(2, 4)$ generalized Pauli principle.

3.5 Structures in entanglement spectrum

As discussed in previous sections, the entanglement spectrum of the ground state of a short-range $(m + 1)$-body interaction has a gap corresponding to the $(m, m + 2)$-admissible counting, for $m = 1, 2$. This gap measures the prominence of m-particle clustering in the ground state. The $(m+1)$-body interactions could possibly generate clusters of other sizes as well. For example, in the FQH effect in the continuum, MR states can be obtained with just two-body potentials. In that case, there could be additional gaps in the entanglement spectrum, and the counting of levels below these gaps could conform to other generalized Pauli principles.

The appearance of a $(n, n + r)$-admissible counting reveals the existence of a specific clustering pattern in the ground state. This pattern is also present in the model fermionic FQH state at filling $\nu = n/(n + r)$ described by the (n, r) Jack polynomials multiplied by a Vandermonde determinant [12, 13]. For example, a $(n, n+2)$-admissible counting corresponds to the $\mathbb{Z}_n$ Read-Rezayi FQH state [73], and a $(2, 5)$-admissible counting corresponds to the 'Gaffnian' FQH wave function [81]. The model wave functions of such FQH states have characteristic zeros when a cluster of $n+1$ particles forms even after removing the "trivial" zeros provided by the fermionic statistics. This reflects specific $(n + 1)$-body correlations in the system. Therefore, the presence of a gap with a $(n, n + r)$ admissible counting in the FCI entanglement

spectrum signals the presence of clustering correlations similar to a specific model FQH state, and implies the presence of stable $(n+1)$-body correlations in the system.

We check comprehensively all the four models studied in this chapter as well as the checkerboard lattice model [87, 74], at various system sizes up to $N = 12$ particles. In most cases, we find extra entanglement gaps other than the one above the states of $(m, m+2)$-admissible counting in the ground state of an $(m+1)$-body interaction, and the counting of entanglement energy levels below *some* of these gaps matches with an $(n, n+r)$-admissible counting in each momentum sector. For all the systems we look at, we usually find at least one such extra gap that matches perfectly with a particular $(n, n+r)$-admissible rule. For example, in the Kagome lattice model with two-body interaction, we find two extra entanglement gaps in the ground state (Fig. 3.31), with the counting of levels below them given *exactly* (in each momentum sector) by the $(2, 4)$- and $(2, 5)$-admissible counting and the folding based on the FQH-FCI mapping [16]. The former case corresponds to the MR state while the latter corresponds to the Gaffnian wave function. We find the appearance of the counting of non-Abelian statistics in the Laughlin-like ground state of two-body interactions quite intriguing.

We do not have a complete understanding of the full gap structure at the moment. In the earlier example of the ruby lattice model shown in Fig. 3.30, we find a few extra entanglement gaps. Two of them have counting below the gap given *exactly* (in each momentum sector) by $(3, 5)$- and $(3, 7)$-admissible rules [16] respectively, the former of which corresponds to a $\mathbb{Z}_3$ Read-Rezayi state. There are other entanglement gaps in the spectrum that cannot be explained by any $(n, n+r)$-admissible rule.

All of such extra $(n, n+r)$ entanglement gaps that we observe have $n+1 = N_A$, where N_A is the number of particles left in the system when evaluating the entanglement spectrum. Tracing out part of the system enhances the correlation between the remaining N_A particles. One can imagine that such enhancement is

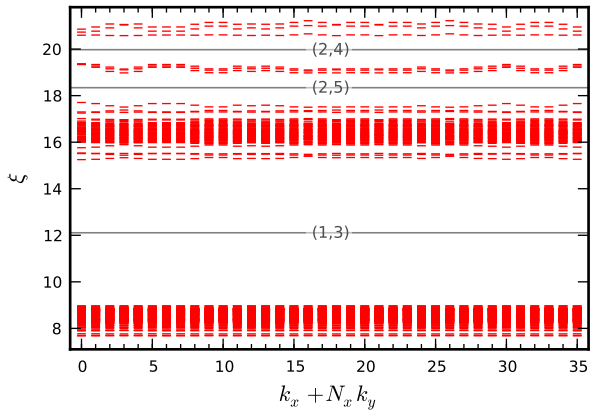

Figure 3.31: Particle entanglement spectrum of the ground state of the Kagome lattice model of $N = 12$ particles on the $N_x \times N_y = 6 \times 6$ lattice, with $N_B = 9$ particles traced out. The number of states below each of the three gray lines is $138, 195, 198$ in momentum sectors where $k_x, k_y \in \{0, 3\}$ and $135, 192, 195$ elsewhere. These numbers are in perfect accordance with the $(1, 3)$-, $(2, 5)$-, and $(2, 4)$-admissible counting, respectively.

more significant for the correlation between the N_A particles as a whole than the correlation within a fraction of the N_A particles. In most cases, we observe such $(N_A - 1, N_A - 1 + r)$ entanglement gaps for almost every value of N_A. Our examples show that a ground-state wave function at $\nu = 1/3$ can give us information about possible non-Abelian correlations.

This suggests a feature of the FCI: the $(n+1)$-body interacting Hamiltonian could not only generate strong $(n+1)$-body correlations, but also higher-body correlations. This gives hope for the possible realization of other members of the Read-Rezayi series with two-body potentials. It is very intriguing that entanglement in the ground state of an $(n + 1)$-body interacting Hamiltonian at filling $\nu = n/(n + 2)$ contains clear clues that some other FQH states could possibly be stabilized by some *other* interaction at some *other* filling.

3.6 Discussion

In this chapter, we have studied four examples of flat-band Chern insulators. If we include the previous articles [80, 65, 94, 74] on the checkerboard lattice, we now have five cases which can be used to compare the universal physics.

First, we have showed that the existence of FCI does not require a special lattice. Under proper conditions, FCI phases could (at least) emerge from lattice models with 2, 3, or 6 sites per unit cell. There is no restriction on the type of Bravais lattice either.

Second, we find concrete evidence that the stability of the FCI phase is not guaranteed by flat band dispersion. A large enough gap to bandwidth ratio is necessary for the existence of an insulating state at a fractional filling. Our calculations performed in the flat-band limit do not capture this effect. However, our results reveal that the single-particle eigenstates play a critical role in the formation of a FCI state as well; a badly chosen parameter set could destroy the topological phase even when the band dispersion is perfectly flat. The example of the Kagome model is especially instructive. While the addition of NNN hopping terms could make the band flatter, it actually deteriorates the FCI phase. Thus the search of a realistic FCI that would include the effect of the band dispersion relation, should not focus only on the flat-band criterion.

Third, the development of a FCI state is often dependent on suppressed fluctuations in the Berry curvature. This agrees qualitatively with the picture derived from the algebra of projected density operators. It should be noted, however, that even the suppressed curvature fluctuations could actually be considerably strong.

Fourth, out of the five models that we have checked, the Kagome lattice model with only NN hoppings has the most robust FCI phase. The ruby lattice model comes close, but has three more tunable parameters.

In conclusion, we have established the existence of a FCI phase in four distinct flat-band lattice models at filling $\nu = 1/3$ with short-range repulsive density-density interactions. The FCI phase is identified by an incompressible ground state with Hall conductance $\sigma_{xy} = 1/3$ and excitations obeying the same counting as Laughlin quasiholes. We have observed that in some cases, band structures that favor the emergence of the FCI phase have less fluctuating Berry curvature. In the presence of short-range three-body repulsive interactions, we have also found another FCI phase reminiscent of the Pfaffian Moore-Read FQH state at half filling of the Kagome lattice model and the ruby lattice model, in addition to the previously known example of the Moore-Read phase in the checkerboard lattice model. This more exotic phase has an incompressible ground state with Hall conductance $\sigma_{xy} = 1/2$ and excitations exhibiting the counting of Moore-Read quasiholes. On the technical side, we have demonstrated from various angles the power of the entanglement spectrum as a sensitive and reliable probe of topological order, when no model wave functions are available. We have also discussed interesting structures in the entanglement spectrum and their implication for the possible stable existence of other FQH states at zero magnetic field.

Chapter 4

Wannier Wave-Functions for Fractional Chern Insulators

In the previous chapter, we established the existence of the fractional Chern insulator (FCI) phase in an array of lattice models with Chern number $C = 1$, and discussed its qualitative resemblance to the fractional quantum Hall (FQH) effect manifested in the energy and the entanglement spectra. Despite the similarity of the emergent features, the FCI and the FQH effects are hosted by substantially different systems. The FQH effects are typically observed in two-dimensional electron gas. This continuum system allows a holomorphic description, and the variational trial wave functions can be characterized by the asymptotic behavior when particles approach each other [12, 13]. In sharp contrast, the Chern insulators are defined on a discrete lattice, and its continuum limit is different from the FQH effect [50, 59]. This obstructs attempts to build model wave functions using the asymptotic behavior.

An open question is thus *to what extent and in what form the FCI can be described by the FQH physics.* In this chapter we provide a generic scheme to compare FQH and $C = 1$ FCI wave functions at finite size. In particular, we address the fermionic FCI phase at filling $\nu = 1/3$ and clarify its relation to the Laughlin state.

The first step in this direction was made by Qi in Ref. [71]. The one-dimensional maximally localized Wannier states are plane waves localized in the direction perpendicular to propagation. They form an alternative basis in a topological flat band, and they resemble the Landau orbitals in the lowest Landau level (LLL) in the continuum. The central, elegant idea of Ref. [71] is to exploit this similarity and transcribe FQH wave functions written in the second-quantized form to the FCI system. The two-dimensional (2D) fractional topological insulator (FTI) system was similarly analyzed using decoupled FQH states in the Wannier basis.

Upon closer inspection, the original proposal suffers from several issues that prevent direct application of this scheme to make contact with existing numerical studies. The formalism in Ref. [71] was built upon a smooth gauge in the continuum. This poses technical challenges for numerical implementation on a finite-size lattice, and conceptually, the one-dimensional (1D) *maximally* localized Wannier states are orthogonal to each other *only in the continuum limit*. The non-orthogonality at finite size spoils the translational invariance of the constructed many-body states. More importantly, the maximally localized Wannier orbital to LLL mapping in Ref. [71] is a mapping between the basis states of two *separate* systems. The two sets of basis states have *independent gauge freedoms*. Merely introducing a 1D relabeling of the Wannier states is not enough to properly fix the mapping from a Chern insulator to the LLL. A naive implementation of the formulas in Ref. [71] results in variational states very low overlaps (lower than 0.04 for a system of 8 particles on a 6×4 lattice) with the exact diagonalization ground states of the two-orbital model discussed therein.

In this chapter, we build upon Ref. [71] and provide an improved prescription for constructing $C = 1$ FCI wave functions using gauge-fixed (non-maximally) localized Wannier states, with large overlap with the exact diagonalization ground states. Our procedure is defined on a lattice of finite size with periodic boundary conditions in

both directions. We do not need gauge smoothing, and we trade maximal localization for the orthogonality between the 1D localized Wannier states at finite size. We explicitly fix the phase choice of the Wannier states so that it best matches that of the Landau orbitals. Our prescription keeps both the center-of-mass translational symmetry and the inversion symmetry at the many-body level, and it implements the folding rule [16] that accounts for the total momenta of the degenerate FCI ground states on a torus. We also show that, in our prescription, using the Wannier bases localized in either x or y directions produces the same set of many-body states in the limit of flat Berry curvature.

As a numerical test, we construct the Laughlin state for several FCI models at filling $\nu = 1/3$. In all cases, the lattice Laughlin states have very high overlap with the ground states, and their entanglement spectra share the same gapped structure. The overlap for the best FCI models found so far reaches 0.99 for a system of 8 particles on a 6×4 lattice, of which the Hilbert space dimension is as large as 3×10^4 in each total momentum sector. Our results provide the first *direct, quantitative* evidence that the fractionalized phase in Chern insulators at $\nu = 1/3$ can be well approximated by the Laughlin state.

The chapter is organized as follows. In Sec. 4.1 we discuss the many-body translational symmetries [39] of the torus FQH states in the continuum. We construct a recombined set of degenerate FQH states that allow a direct mapping to the lattice. Sec. 4.2 summarizes with the basic properties of the 1D localized Wannier states on a lattice. Except for a few subtleties, this discussion is similar to the one in Ref. [71]. In Sec. 4.3 describes the Wannier construction of the many-body FQH states on a lattice. We elaborate upon the *phase* choice of the 1D localized Wannier states. We show that the resulting many-body states are translationally invariant in both directions. We also demonstrate that the counting of the q-fold states in each momentum sector agrees with the counting rule proposed in Ref. [16]. Eq. (4.65) provides an

explicit and ready-to-use formula to rewrite *any FQH wave function* in a given Chern insulator model. Sec. 4.4 presents the numerical verification that the ground states of various FCI models are well approximated by the Laughlin state constructed using our prescription. We also examine how close our phase choice for the Wannier basis is from the absolute ideal by a brute-force optimization. Sec. 4.5 concludes the chapter and discusses a few future directions.

4.1 FQH translational symmetries

It is instructive to review the many-body translational symmetries of the FQH system in the continuum. We begin by recapitulating the main results of the PRL [39] by Haldane.

We study the problem of N_e electrons moving on a *twisted* torus with a perpendicular magnetic field. The twisted torus can be represented by a parallelogram with opposite edges identified. We set up a Cartesian coordinate system $(\widetilde{x}, \widetilde{y})$, with orthonormal basis vectors $(\hat{e}_x, \hat{e}_y)$. The tilde over $\widetilde{x}$ and $\widetilde{y}$ emphasizes the continuous nature of these variables. We consider the torus spanned by $\mathbf{L}_1 = L_1\hat{e}_v$ and $\mathbf{L}_2 = L_2\hat{e}_y$ (see Fig. 4.1).[1] Here, L_1 and L_2 are the length of the two fundamental cycles of the torus, and the unit vector $\hat{e}_v$ is defined by $\hat{e}_v = \sin\theta\,\hat{e}_x + \cos\theta\,\hat{e}_y$, where the twist angle $\theta \in (0, \pi)$ is the angle between the two fundamental cycles. The rectangular torus corresponds to $\theta = \pi/2$. We introduce the normal unit vector $\hat{e}_z \equiv \hat{e}_x \times \hat{e}_y$, and define the reciprocal primitive vectors

$$\mathbf{G}_1 = 2\pi\hat{e}_x/(L_1 \sin\theta), \qquad \mathbf{G}_2 = 2\pi(\hat{e}_y - \cot\theta\,\hat{e}_x)/L_2. \tag{4.1}$$

They satisfy $\mathbf{G}_a \cdot \mathbf{L}_b = 2\pi\delta_{ab}$ for $a, b \in \{1, 2\}$.

[1] It is always possible to line up $\mathbf{L}_2$ with the $\hat{e}_y$ axis for a torus of any aspect ratio.

The torus is pierced by a magnetic field in the $-\hat{e}_z$ direction, $\mathbf{B} = \nabla \times \mathbf{A} = B\hat{e}_z$ with $B < 0$. The Hamiltonian of the interacting electrons reads

$$H = \sum_i \frac{[-i\hbar\nabla_i - e\mathbf{A}(\widetilde{\mathbf{r}}_i)]^2}{2m} + \sum_{i<j} V(\widetilde{\mathbf{r}}_i - \widetilde{\mathbf{r}}_j). \tag{4.2}$$

We denote by $e < 0$ the charge of the electron. The magnetic length is $l_B = \sqrt{\hbar/(eB)}$. The total number of fluxes N_ϕ penetrating the torus has to be an integer, given by $L_1 L_2 \sin\theta = 2\pi l_B^2 N_\phi$. We define $N = \mathrm{GCD}(N_e, N_\phi)$, where GCD stands for the Greatest Common Divisor. Then $p \equiv N_e/N$ and $q \equiv N_\phi/N$ are coprime.

The magnetic translation operator of a single particle is defined by $T(\mathbf{a}) = e^{-i\mathbf{a}\cdot\mathbf{K}/\hbar}$, where $\mathbf{K} = -i\hbar\nabla - e\mathbf{A}(\widetilde{\mathbf{r}}) + e\mathbf{B}\times\widetilde{\mathbf{r}}$ is the guiding center momentum of the i-th particle. We pick Landau gauge $\mathbf{A}(\widetilde{x}, \widetilde{y}) = B\widetilde{x}\,\hat{e}_y$, and impose periodic (not twisted) boundary conditions $T(\mathbf{L}_a) = 1$, $a = 1, 2$. The wave functions $\langle \widetilde{x}, \widetilde{y} | j \rangle$ of the N_ϕ single-particle states in the LLL are given by

$$\phi_j(\widetilde{x}, \widetilde{y}) = \frac{e^{-\widetilde{x}^2/(2l_B^2)}}{(\sqrt{\pi} L_2 l_B)^{1/2}} \sum_n^{\mathbb{Z}} \exp\left[2\pi(j + nN_\phi)\frac{\widetilde{x} + i\widetilde{y}}{L_2} - i\frac{\pi}{N_\phi}\frac{L_1 e^{-i\theta}}{L_2}(j + nN_\phi)^2 \right] \tag{4.3}$$

where the state index j is an integer defined modulo N_ϕ.

We can decompose the translation operator of the i-th electron, $T_i(\mathbf{a})$, into a relative part and a center-of-mass part, $T_i(\mathbf{a}) = T_{\mathrm{rel},i}(\mathbf{a}) T_{\mathrm{cm}}(\mathbf{a}/N_e)$, where

$$T_{\mathrm{rel},i}(\mathbf{a}) = T_i(\mathbf{a}) \prod_j^{N_e} T_j(-\tfrac{\mathbf{a}}{N_e}), \qquad\qquad T_{\mathrm{cm}}(\mathbf{a}) = \prod_j^{N_e} T_j(\mathbf{a}). \tag{4.4}$$

Here and hereafter throughout the chapter, we use shorthand notation for products and summations: $\prod_i^M \equiv \prod_{i=0}^{M-1}$, $\sum_i^M \equiv \sum_{i=0}^{M-1}$. We are particularly interested in the following translation operators and we define the shorthand notations

$$T^x_{\mathrm{rel},i} = T_{\mathrm{rel},i}(p\mathbf{L}_1), \quad T^y_{\mathrm{rel},i} = T_{\mathrm{rel},i}(p\mathbf{L}_2), \quad T^x_{\mathrm{cm}} = T_{\mathrm{cm}}(\mathbf{L}_1/N_\phi), \quad T^y_{\mathrm{cm}} = T_{\mathrm{cm}}(\mathbf{L}_2/N_\phi).$$

Thanks to the periodic boundary condition, we can drop the particle index i from the relative translation operators, since $T^x_{\mathrm{rel},i} = [(T^x_{\mathrm{cm}})^q]^\dagger$ and $T^y_{\mathrm{rel},i} = [(T^y_{\mathrm{cm}})^q]^\dagger$ do not depend on the particle index.

The operators $T^x_{\rm rel}$ and $T^y_{\rm cm}$, and of course $T^y_{\rm rel}$ being a power of $T^y_{\rm cm}$, commute with each other and the Hamiltonian H [39]. We use them to block-diagonalize the Hamiltonian into momentum sectors labeled by two-dimensional (2D) wave numbers (κ_x, κ_y) in an $N \times N_\phi$ Brillouin zone, defined by the eigenvalues[2]

$$T^x_{\rm rel} = e^{i2\pi\kappa_x/N}, \quad T^y_{\rm cm} = e^{-i2\pi\kappa_y/N_\phi}. \tag{4.5}$$

The operator $T^x_{\rm cm}$ commutes with $T^x_{\rm rel}$ and H, but not with $T^y_{\rm cm}$:

$$T^y_{\rm cm} T^x_{\rm cm} = T^x_{\rm cm} T^y_{\rm cm} e^{-i2\pi p/q}. \tag{4.6}$$

Therefore, the many-body energy eigenstates can be grouped into q-fold center-of-mass multiplets; the q states in each multiplet can be transversed by successive applications of $T^x_{\rm cm}$ and they share the same energy and the value of κ_x and κ_y mod N.

We set the cyclotron energy to infinity and focus on the states in the LLL. In this approximation, the many-body Hilbert space is spanned by the occupation-number basis states (Slater determinants) constructed from the LLL states $|j\rangle$. We use the curly braces $\{\cdot\}$ to denote a list of quantum numbers for the N_e electrons. For succinctness, we always omit the electron indices from $\{\cdot\}$ and related expressions.

Now we are in a position to establish a concrete representation of the many-body translation algebra. The basis states in the LLL are $|\{j\}\rangle \equiv |j_0, j_1, \ldots, j_{N_e-1}\rangle$ with an implied anti-symmetrization. The action of the many-body translation operators reads [16]

$$\begin{aligned} T^x_{\rm rel}|\{j\}\rangle &= |\{j-q\}\rangle, \quad T^y_{\rm rel}|\{j\}\rangle = e^{i2\pi\sum j/N}|\{j\}\rangle, \\ T^x_{\rm cm}|\{j\}\rangle &= |\{j+1\}\rangle, \quad T^y_{\rm cm}|\{j\}\rangle = e^{-i2\pi\sum j/N_\phi}|\{j\}\rangle. \end{aligned} \tag{4.7}$$

[2]Notice that the original treatment in Ref. [39] put an additional factor of $(-1)^{pq(N_e-1)}$ in the formula, but this is not necessary for our purposes: (κ_x, κ_y) are *defined* by Eq. (4.5). Our choice can be regarded as an alternative labeling aimed to simplify the formulas in this chapter, at the cost of the identity of (κ_x, κ_y) as true momentum.

Here the sum $\sum j$ runs over all the particles, and the state $|\{j+l\}\rangle$ is obtained from $|\{j\}\rangle$ by shifting the j quantum number of each particle by l. As expected, the relative and the center-of-mass translations are related by the periodic boundary conditions, $T^x_{\rm rel} = [(T^x_{\rm cm})^q]^\dagger$, $T^y_{\rm rel} = [(T^y_{\rm cm})^q]^\dagger$.

4.1.1 Recombination of the q-fold states

It has been suggested that the FCI with $|C| = 1$ on an $N_x \times N_y$ lattice corresponds to a FQH system with flux $N_\phi = N_x N_y$ [71, 16]. We now look for an alternative representation of the many-body translational symmetries with a Brillouin zone commensurate to the lattice system, in preparation for the analysis of the translational symmetry of the Wannier construction in Sec. 4.3.3. We emphasize that we are still working in the continuum and we are merely providing another representation of the center-of-mass translation algebra. The integers N_x and N_y should be understood as a factorization of N_ϕ at this stage.

Following Ref. [16], we define the integers $N_{0x} = \mathrm{GCD}(N_e, N_x)$, $N_{0y} = \mathrm{GCD}(N_e, N_y)$, and $p_x = N_e/N_{0x}$, $p_y = N_e/N_{0y}$, $q_x = N_x/N_{0x}$, $q_y = N_y/N_{0y}$. Obviously p_x, q_x are coprime, so are p_y, q_y. Less obviously, $q_x q_y$ divides q [16], and thus p, q_x are coprime, so are p, q_y. We define the translation operators[3]

$$S_x = (T^x_{\rm cm})^{q/q_x}, \qquad\qquad R_y = (T^y_{\rm cm})^{q_x}. \tag{4.8}$$

They commute with each other and the Hamiltonian H. Therefore, we can use (S_x, R_y), instead of $(T^x_{\rm rel}, T^y_{\rm cm})$, to block-diagonalize the Hamiltonian into momentum sectors. Since $(S_x)^{q_x} = (T^x_{\rm rel})^\dagger$, the new set of 2D wave numbers defined by (S_x, R_y)

[3]We emphasize that the operators S_x and R_y are defined in the continuum. In contrast to the discussions in Ref. [16], here we do not add a lattice pinning potential to the FQH setup. Were we to do that, S_x and R_y would not be legitimate translation operators as they contain one-body translations that are a fraction of a unit cell size. We bridge the FQH and the FCI sides through the properties of the second-quantized amplitudes, without directly migrating the continuum translation operators and their algebra to the lattice.

takes value from an $(Nq_x) \times (N_{0x}N_y)$ Brillouin zone [as opposed to the $N \times N_\phi$ Brillouin zone of Eq. (4.7)].

Notice that S_x operates within the q-fold multiplet. Successive applications of S_x break the multiplet into non-overlapping orbits. The states in each orbit have the same R_y eigenvalue due to $[S_x, R_y] = 0$. The orbit structure can be revealed by the eigenvalues of $T^y_{\rm cm}$, as they are distinct for the q states. Plugging Eq. (4.8) into Eq. (4.6), we have

$$T^y_{\rm cm} S_x = S_x T^y_{\rm cm} e^{-i2\pi p/q_x}, \quad T^x_{\rm cm} R_y = R_y T^x_{\rm cm} e^{i2\pi p/(q/q_x)}. \tag{4.9}$$

Therefore, every orbit of S_x has the same length q_x, and thus the total number of orbits is q/q_x. Further, for $r \in [0 \,..\, q/q_x)$, $(T^x_{\rm cm})^r$ brings any given state in the q-fold multiplet to q/q_x distinct states discriminated by R_y eigenvalues, and thus belonging to q/q_x different orbits of S_x. This covers *each* of the orbits exactly *once*.

We can recombine the q-fold states to form simultaneous eigenstates of S_x and R_y. We start the construction from an arbitrary energy eigenstate $|\Psi\rangle$ in the q-fold multiplet diagonal in $(T^x_{\rm rel}, T^y_{\rm cm})$, labeled by $\kappa_x \in [0 \,..\, N)$ and $\kappa_y \in [0 \,..\, N_y)$. The usual, relative y-momentum which labels the eigenvalue of $T^y_{\rm rel}$ can be easily obtained as κ_y mod N. For the Laughlin case at filling $\nu = 1/3$, $|\Psi\rangle$ is just one of the threefold degenerate states on the torus. The q states can be regrouped into the orbits of S_x, labeled by r:

$$\left\{ (S_x)^m (T^x_{\rm cm})^r |\Psi\rangle \,\middle|\, m \in [0 \,..\, q_x) \right\}, \quad r \in [0 \,..\, q/q_x). \tag{4.10}$$

We can recombine the q_x states in each orbit into q_x eigenstates of S_x. Within the multiplet, ince $(S_x)^{q_x} = (T^x_{\rm rel})^\dagger = e^{-i2\pi\kappa_x/N}$, we have

$$(S_x)^{q_x} = e^{-i2\pi q_x(\kappa_x + sN_e)/(Nq_x)}. \tag{4.11}$$

Note that the values of $e^{i2\pi(\kappa_x+sN_e)/(Nq_x)}$ are distinct for $s \in [0 \,..\, q_x)$, thanks to p, q_x being coprime. We define the $q_x \times (q/q_x)$ states

$$|\Psi; s, r\rangle = \frac{1}{\sqrt{q_x}} \sum_m^{q_x} e^{i2\pi m(\kappa_x+sN_e)/(Nq_x)} (S_x)^m (T^x_{\rm cm})^r |\Psi\rangle, \tag{4.12}$$

for $s \in [0 \,..\, q_x)$ and $r \in [0 \,..\, q/q_x)$. These states are orthonormal, and they are simultaneous eigenstates of S_x and R_y in the $(Nq_x) \times (N_{0x}N_y)$ Brillouin zone,[4]

$$\begin{aligned} S_x|\Psi; s, r\rangle &= e^{-i2\pi(\kappa_x+sN_e)/(Nq_x)}|\Psi; s, r\rangle, \\ R_y|\Psi; s, r\rangle &= e^{-i2\pi(\kappa_y+rN_e)/(N_{0x}N_y)}|\Psi; s, r\rangle. \end{aligned} \tag{4.13}$$

The $q_x \times (q/q_x)$ states are related by center-of-mass translations, namely

$$T^x_{\rm cm}|\Psi; s, r\rangle = |\Psi; s, r+1\rangle, \quad T^y_{\rm cm}|\Psi; s, r\rangle = e^{-i2\pi(\kappa_y+rN_e)/N_\phi}|\Psi; s-1, r\rangle. \tag{4.14}$$

In terms of amplitudes, the second equation above can be written as [using Eq. (4.7)]

$$e^{-i2\pi \sum j/N_\phi}\langle\{j\}|\Psi; s, r\rangle = e^{-i2\pi(\kappa_y+rN_e)/N_\phi}\langle\{j\}|\Psi; s-1, r\rangle. \tag{4.15}$$

Incidentally, we note that $|\Psi; s, r\rangle$ is periodic under $s \to s + q_x$, but it acquires a phase when $r \to r + q/q_x$ [since $(T^x_{\rm cm})^{q/q_x} = S_x$ as defined in Eq. (4.8)]

$$|\Psi; s, r + q/q_x\rangle = e^{-i2\pi(\kappa_x+sN_e)/(Nq_x)}|\Psi; s, r\rangle. \tag{4.16}$$

4.1.2 Translational symmetries in amplitudes

We now consider the manifestation of the translation symmetries in the amplitudes $\langle\{j\}|\Psi; s, r\rangle$. The action of S_x and R_y on the basis states $|\{j\}\rangle$ reads

$$S_x|\{j\}\rangle = |\{j + q/q_x\}\rangle, \quad R_y|\{j\}\rangle = e^{-i2\pi \sum j/(N_{0x}N_y)}|\{j\}\rangle. \tag{4.17}$$

Therefore, from the first equation above we have

$$e^{-i2\pi(\kappa_x+sN_e)/(Nq_x)}\langle\{j\}|\Psi; s, r\rangle = \langle\{j - q/q_x\}|\Psi; s, r\rangle, \tag{4.18}$$

[4] A notable special case is when q divides N_y. Since $\mathrm{GCD}(N_y, q) = \mathrm{GCD}(pN_y, q) = N_yN_{0x}/N = q/q_x$, in this case we have $q_x = 1$, and thus $S_x = (T^x_{\rm rel})^\dagger$ and $R_y = T^y_{\rm cm}$. Hence, the original q-fold states diagonal in $(T^x_{\rm rel}, T^y_{\rm cm})$ are already the simultaneous eigenstates of S_x and R_y without any recombination.

while from the second, we find that the amplitude $\langle\{j\}|\Psi; s, r\rangle$ vanishes unless

$$\sum j = \kappa_y + rN_e \bmod N_{0x}N_y. \tag{4.19}$$

The last two equations above summarize the information that we need from the FQH side to establish the translational invariance of the FCI many-body wave functions to be constructed in Sec. 4.3 on an $N_x \times N_y$ lattice.

4.2 Hybrid localized Wannier states

We now proceed to establish the hybrid Wannier basis in a Chern band on a lattice. The ultimate goal is to construct 1D localized Wannier states which are plane waves in the second direction (hybrid). Such states mimic the Landau orbitals $|j\rangle$. We begin by reviewing the construction and the properties of the 1D maximally localized Wannier states [49, 57, 105].

Consider a 2D band insulator with N_b orbitals per unit cell, indexed by α. We assume lattice translational symmetry and periodic boundary conditions. Denote the primitive translation vectors by $\mathbf{b}_1$ and $\mathbf{b}_2$, with $\hat{e}_z \cdot (\mathbf{b}_1 \times \mathbf{b}_2) > 0$. Then the Bravais lattice is indexed by $x\mathbf{b}_1 + y\mathbf{b}_2$, with $(x, y) \in \mathbb{Z}^2$ [to be differentiated from $(\widetilde{x}, \widetilde{y}) \in \mathbb{R}^2$ in the continuum.] We pick the principal region to be $(x, y) \in [0 \,..\, N_x) \times [0 \,..\, N_y)$. The momentum space is given by the reciprocal lattice $\mathbf{k}$. We label points in the momentum space by wave numbers $(k_x, k_y) \in \mathbb{Z}^2$, defined by $k_x = \mathbf{k}\cdot\mathbf{b}_1$ and $k_y = \mathbf{k}\cdot\mathbf{b}_2$. The single-particle orbitals can be written as $|x, y, \alpha\rangle$, or $|k_x, k_y, \alpha\rangle$ in the momentum space.

The energy eigenstates are Bloch waves. We focus on a single, isolated band $|k_x, k_y\rangle$, which will be fractionally filled in the many-body construction. For now we only focus on the one-band problem. Generalization to the 2D FTI problem is straightforward as that problem decouples in the Wannier basis. The wave function of the Bloch band is $u_\alpha(k_x, k_y) = \langle k_x, k_y, \alpha|k_x, k_y\rangle$. We assume periodic boundary

condition in *both* k_x and k_y directions, $|k_x + l_x N_x, k_y + l_y N_y, n\rangle = |k_x, k_y, n\rangle$, for $l_x, l_y \in \mathbb{Z}$. We set the first Brillouin zone to $[0 \,..\, N_x) \times [0 \,..\, N_y)$.

We denote the position of an orbital α relative to its unit cell coordinate by $\epsilon_\alpha^x \mathbf{b}_1 + \epsilon_\alpha^y \mathbf{b}_2$, where $(\epsilon_\alpha^x, \epsilon_\alpha^y) \in \mathbb{R}^2$ are the relative displacements of the orbitals within an unit cell. Taking into account the periodic boundary, we can define the (exponentiated) position operators

$$\widehat{x} = \sum_{x,y} \sum_{\alpha} |x, y, \alpha\rangle e^{-i2\pi(x+\epsilon_\alpha^x)/N_x} \langle x, y, \alpha|, \tag{4.20}$$

and similarly $\widehat{y}$. Here the integers (x, y) are summed over the Bravais lattice points in the principal region of the torus, and α is summed over all N_b orbitals.

Using the projector to the occupied band

$$P = \sum_{k_x, k_y} |k_x, k_y\rangle\langle k_x, k_y|, \tag{4.21}$$

we can define the projected position operators $\widehat{\mathcal{X}} = P\widehat{x}P$ and $\widehat{\mathcal{Y}} = P\widehat{y}P$. In the momentum space, they take the form

$$\widehat{\mathcal{X}} = \sum_{k_x, k_y} |k_x, k_y\rangle \mathcal{A}_x(k_x, k_y) \langle k_x + 1, k_y|, \quad \widehat{\mathcal{Y}} = \sum_{k_x, k_y} |k_x, k_y\rangle \mathcal{A}_y(k_x, k_y) \langle k_x, k_y + 1|,$$

where (k_x, k_y) is summed over the first Brillouin zone, and $\mathcal{A}_{x,y}(k_x, k_y)$ are the (exponentiated) Berry connections given by

$$\begin{aligned} \mathcal{A}_x(k_x, k_y) &= \langle k_x, k_y | \widehat{x} | k_x + 1, k_y \rangle = \sum_\alpha e^{-i2\pi\epsilon_\alpha^x/N_x} u_\alpha^*(k_x, k_y) u_\alpha(k_x+1, k_y), \\ \mathcal{A}_y(k_x, k_y) &= \langle k_x, k_y | \widehat{y} | k_x, k_y + 1 \rangle = \sum_\alpha e^{-i2\pi\epsilon_\alpha^y/N_y} u_\alpha^*(k_x, k_y) u_\alpha(k_x, k_y+1). \end{aligned} \tag{4.22}$$

Notice that the Berry connections depend on the embedding of the lattice and its orbitals in real space, as does the Berry curvature. We emphasize that the definition of the exponentiated discrete Berry connections does not require a smooth gauge.

4.2.1 Localization and orthogonality

Thanks to the translational invariance, we can view the 2D system as N_y decoupled 1D subsystems labeled by the momentum k_y. The position operator $\widehat{\mathcal{X}}$ operates within each subsystem and is diagonal in k_y. At each value of k_y, the eigenstates of this operator are the closest analogue to the states $|x, k_y, \alpha\rangle$ that we can construct within the occupied bands; they are the maximally localized Wannier state for the 1D subsystem [49, 57, 105]. The eigenvalue of $\widehat{\mathcal{X}}$ is the (exponentiated) Wannier center position in the $\mathbf{b}_1$ direction.

Ref. [71] proposed to build FQH wave functions using the maximally localized Wannier orbitals as one body basis with a one-to-one mapping into the LLL orbitals. A major issue at finite size, however, is that the N_x eigenstates of the projected position operator at each value of k_y are *not orthogonal* due to the *non-unitarity* of the projected position operator at finite N_x. Gram-Schmidt orthogonalization is not a suitable solution, as it mixes the Wannier states localized in different unit cells, thereby spoiling the translational invariance. The proper resolution is to keep only the *phase* part of the exponentiated Berry connection and use the alternative, unitary projected position operators to define the 1D localized Wannier states. Specifically, we define the unitary connections[5]

$$A_a(k_x, k_y) = \mathcal{A}_a(k_x, k_y)/|\mathcal{A}_a(k_x, k_y)|, \quad a = x, y, \tag{4.23}$$

and the unitary projected position operators

$$\widehat{X} = \sum_{k_x,k_y} |k_x, k_y\rangle A_x(k_x, k_y)\langle k_x + 1, k_y|, \quad \widehat{Y} = \sum_{k_x,k_y} |k_x, k_y\rangle A_y(k_x, k_y)\langle k_x, k_y + 1|. \tag{4.24}$$

Technically, the eigenstates of these operators are not *maximally* localized (they are almost so), but this is a small price to pay for the orthogonality.

[5]The non-unitary connection $\mathcal{A}_a(k_y, k_y)$ $(a = x, y)$ may vanish on a very small lattice. This problem is most pronounced on an $N_x \times N_y = 2 \times 2$ lattice with inversion symmetry. In this case, all the four Bloch states are inversion eigenstates. The connection $\mathcal{A}_a$ between two Bloch states vanishes when the two states belong to different inversion eigenvalues. We do not consider such pathological cases in our treatment.

Thanks to the gauge periodicity in both k_x and k_y, we can define the unitary Wilson loops

$$W_x(k_y) = \prod_{k_x}^{N_x} A_x(k_x, k_y), \qquad\qquad W_y(k_x) = \prod_{k_y}^{N_y} A_y(k_x, k_y).$$

For later convenience, we introduce $\lambda_x(k_y)$ and $\lambda_y(k_x)$ defined by

$$[\lambda_x(k_y)]^{N_x} = W_x(k_y), \qquad\qquad [\lambda_y(k_x)]^{N_y} = W_y(k_x). \tag{4.25}$$

We pick $\lambda_x(k_y)$ to be the N_x-th root with argument angle in $(-2\pi/N_x, 0]$, and $\lambda_y(k_x)$ to be the N_y-th root with argument angle in $(-2\pi/N_y, 0]$. We can interpret $\lambda_y(k_x)$ and $\lambda_y(k_x)$ as the "average" phase (connection) of the Wilson loop evenly distributed to each bond along the loop. In general, for more than one occupied band, $\lambda_x(k_y)$ and $\lambda_y(k_x)$ are obtained from the sets of eigenvalues of the corresponding Wilson loop matrices.

The eigenvalues and the eigenstates of $\widehat{X}$ can be found easily, due to its decoupling into N_y blocks labeled by k_y. Each block $\widehat{X}_{k_y}$ is an $N_x \times N_x$ matrix in the Bloch basis. The N_x eigenvalues of $\widehat{X}_{k_y}$ are given by the N_x-th roots of $W_x(k_y)$ [105],

$$\widehat{X}_{k_y}|X, k_y\rangle = \Lambda_x(X, k_y)|X, k_y\rangle, \tag{4.26}$$

where $\Lambda_x(X, k_y) = e^{-i2\pi X/N_x}\lambda_x(k_y)$, indexed by $X \in [0\,..\,N_x)$. The eigenstate belonging to the eigenvalue $\Lambda_x(X, k_y)$ can be written

$$|X, k_y\rangle = \frac{e^{i\Phi_y(X,k_y)}}{\sqrt{N_x}} \times \sum_{k_x}^{N_x} e^{-i2\pi k_x X/N_x} \left\{ \frac{[\lambda_x(k_y)]^{k_x}}{\prod_{\kappa}^{k_x} A_x(\kappa, k_y)} \right\} |k_x, k_y\rangle. \tag{4.27}$$

Recall that we use the shortand

$$\prod_{\kappa}^{k_x} A_x(\kappa, k_y) \equiv \prod_{\kappa=0}^{k_x-1} A_x(\kappa, k_y). \tag{4.28}$$

Since the curly-braced prefactor in Eq. (4.27) is unitary, these states inherit at finite size the orthonormality of $|k_x, k_y\rangle$ through the Fourier transform. These orthogonal Wannier orbitals are not maximally localized for the finite-size lattice, but

quickly become so as the number of sites N_x increases. They exhibit a gauge freedom, $\Phi_y(X, k_y) \in \mathbb{R}$, which is a phase to be specified in Sec. 4.3.2.

The center of the 1D localized Wannier state is given by

$$\langle X, k_y|\widehat{x}|X, k_y\rangle = \Lambda_x(X, k_y)\left[\frac{1}{N_x}\sum_{k_x}^{N_x}\left|\mathcal{A}_x(k_x, k_y)\right|\right], \tag{4.29}$$

where the bracketed factor is a positive real number. Therefore, we can interpret

$$\chi^{X,k_y} = -\frac{N_x}{2\pi}\arg[\Lambda_x(X, k_y)] = X - \frac{1}{2\pi}\arg[W_x(k_y)] \tag{4.30}$$

as the center of the maximally localized Wannier function, where we pick the branch of the argument function with $\arg(z) \in (-2\pi, 0]$ to make $\chi^{X,k_y} \in [X, X+1)$. We place the X-th unit cell over $[X, X+1)$. As expected, in each unit cell there are N_y Wannier centers, corresponding to the N_y values of k_y.

For a flat-band Hamiltonian with no band dispersion, such as the single-particle part of the FCI Hamiltonians studied in the previous chapter, the Wannier states are actually single-particle energy eigenstates of the lowest, fractionally filled band. This qualifies the set of all the 1D localized Wannier states $\{|X, k_y\rangle\}$ as a single-particle basis for constructing the many-body trial states for the FCI, which lie entirely in the lowest band, in the same spirit as the LLL projected FQH wave functions.

4.2.2 Gauge freedom

In the language of Ref. [57], the construction of eigenstates in Eq. (4.27) can be interpreted as transforming the Bloch states with an arbitrary phase factor to the "parallel transport" (pt) gauge, in which

$$|k_x, k_y\rangle_{\text{pt}} = \frac{[\lambda_x(k_y)]^{k_x}}{\prod_{\kappa}^{k_x} A_x(\kappa, k_y)}\,|k_x, k_y\rangle, \tag{4.31}$$

and the 1D localized Wannier states are just Fourier transform of the Bloch states $|k_x, k_y\rangle_{\text{pt}}$. Despite the name, technically the phase of $|k_x, k_y\rangle_{\text{pt}}$ contains not only the

parallel transport $\prod_{\kappa}^{k_y} A_x(\kappa, k_y)$ from $|0, k_y\rangle$, it also contains a rotation to accommodate the Wilson loop $W_x(k_y)$.

Under the gauge transform

$$|k_x, k_y\rangle \to e^{i\eta(k_x,k_y)}|k_x, k_y\rangle, \tag{4.32}$$

the Wilson line transforms by

$$\prod_{\kappa}^{k_x} A_x(\kappa, k_y) \to e^{-i\eta(0,k_y)} \prod_{\kappa}^{k_x} A_x(\kappa, k_y)\, e^{i\eta(k_x,k_y)}, \tag{4.33}$$

and thus the Wannier state transforms by

$$|X, k_y\rangle \to e^{i\eta(0,k_y)}|X, k_y\rangle. \tag{4.34}$$

The reason for the appearance of $e^{i\eta(k_x,k_y)}$ with only $k_x = 0$ is obvious: the parallel transport gauge [Eq. (4.31)] depends only on the initial condition at $k_x = 0$ and the gauge-invariant Wilson loop $W_x(k_y)$. Had we chosen to start the parallel transport from k_x^0, the Wannier state would acquire a phase $e^{i\eta(k_x^0,k_y)}$ upon the gauge transform. The full gauge freedom of the Wannier states is kept in the phase $e^{i\Phi_y(X,k_y)}$. Due to the X-dependency, this is much larger than the gauge freedom in $e^{i\eta(0,k_y)}$.

Incidentally, we point out that any gauge fixing in the k_y direction at $k_x \neq 0$ is futile, as the "parallel transport" construction would effectively override any gauge choice at $k_x \neq 0$. This is reflected by the independence of Eq. (4.34) from $e^{i\eta(k_x,k_y)}$ with $k_x \neq 0$.

We emphasize that the phase factor $e^{i\Phi_y(X,k_y)}$, or the single-particle gauge for $|k_x, k_y\rangle$, do *not* affect the localization of the Wannier state, but they do affect essentially the similarity with the LLL. We will discuss the choice of $e^{i\Phi_y(X,k_y)}$ in Sec. 4.3.2.

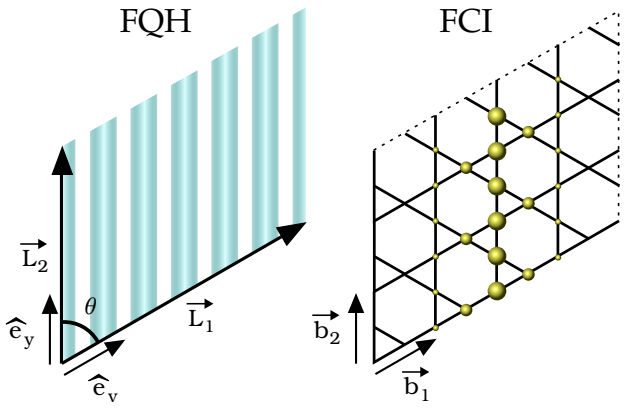

Figure 4.1: Single-particle orbitals in the lowest Landau level (LLL) and the Chern band. In the left panel we show the Landau orbitals in the LLL on a torus. The two fundamental cycles are marked by $\mathbf{L}_1$ and $\mathbf{L}_2$, and the twist angle is labeled by θ. The Landau orbitals are plane waves in the $\hat{e}_y$ direction that are localized in the direction perpendicular to propagation. In the right panel we show a 1D Wannier state localized in the $\mathbf{b}_1$ direction and in the lowest band of the Kagome lattice model. The size of the spheres depicts the weights of the Wannier state on each lattice site.

4.2.3 Connection to the lowest Landau level

Ultimately, we want to bridge the physics of a partially filled band with a Chern number $C = \pm 1$ and that of the spinless FQH effects in the LLL on a continuum torus. (Unless noted otherwise, in this chapter we specialize to Chern number $|C| = 1$.)

As illustrated in Fig. 4.1, at the single-particle level, both the Wannier states $|X, k_y\rangle$ in a Chern band and the Landau-gauge orbitals $|j\rangle$ in the LLL are plane waves localized in the direction perpendicular to wave propagation. Building upon the correspondence between the center lines of the localized states, Ref. [71] proposed a linear relabeling of the Wannier states. The resulting 1D label is analogous to the LLL state index j. We now examine this relabeling of the Wannier states in more details. As we will see, the original prescription lacks a few ingredients that are essential for a concrete numerical implementation of the scheme.

First, we need to specify the torus geometry in the continuum. The number of fluxes in the corresponding LLL problem is given by $N_\phi = N_x N_y$ [71, 16]. We want the continuum torus to take the same shape as the lattice system with periodic

boundaries. The aspect ratio is set to $\frac{L_1}{L_2} = \frac{N_x|\mathbf{b}_1|}{N_y|\mathbf{b}_2|}$. The only remaining parameter is the twist angle θ between $\mathbf{L}_1$ and $\mathbf{L}_2$ (defined in Sec. 4.1). For brevity, we want to map both $C = 1$ and $C = -1$ Chern bands to the LLL with a magnetic field in the $-\hat{e}_z$ direction as studied in Sec. 4.1. For $C = 1$, we put $\mathbf{L}_1$ and $\mathbf{L}_2$ in the direction of $\mathbf{b}_1$ and $\mathbf{b}_2$, respectively. For $C = -1$, we need to "flip" the fundamental parallelogram. This corresponds to choosing the twist angle $\theta = \pi - \langle \mathbf{b}_1, \mathbf{b}_2 \rangle$, where $\langle \mathbf{b}_1, \mathbf{b}_2 \rangle \in (0, \pi)$ is the angle between $\mathbf{b}_1$ and $\mathbf{b}_2$. This choice of θ is justified numerically in Sec. 4.4.2.

We now make a detailed comparison between the LLL orbitals $|j\rangle$ and the Wannier orbitals $|X, k_y\rangle$. In the LLL, the center coordinate $L_1 j/N_\phi$ of orbital $|j\rangle$ in the $\mathbf{b}_1$ direction is a monotonically increasing function of j, and the $j = 0$ orbital is centered along the line $x = 0$. In the Chern band, the unitary Wilson loop $W_x(k_y)$ is a pure phase; when k_y changes, it winds around the unit circle at the origin of the complex plane. In the continuum limit, $W_x(k_y)$ has winding number $C = \pm 1$ when k_y goes around a single Brillouin zone. Assume for the moment that the winding motion of $W_x(k_y)$ on the unit circle is *unidirectional* (clockwise when $C = 1$ and counterclockwise when $C = -1$) when k_y increase from 0 to N_y, i.e. there is no "zigzag" pattern of going back-and-forth anywhere. In this case, when the k_y Brillouin zone boundary is *properly* chosen, $\arg[W_x(k_y)] \in (-2\pi, 0]$ depends *monotonically* on k_y.

The proper choice of the Brillouin zone is illustrated in Fig. 4.2. We start the k_y Brillouin zone from the point where $W_x(k_y)$ is closest to 1 in the lower half of the complex plane. The specific prescription is the following. We pick the branch of $\arg[W_x(k_y)]$ that takes value in $(-2\pi, 0]$. We define the shift $\delta_y \in [0 \,..\, N_y)$ as the cardinality of the set

$$\Big\{ k_y \in [0 \,..\, N_y) \;\Big|\; \arg[W_x(k_y)] > \arg[W_x(0)] \Big\}. \tag{4.35}$$

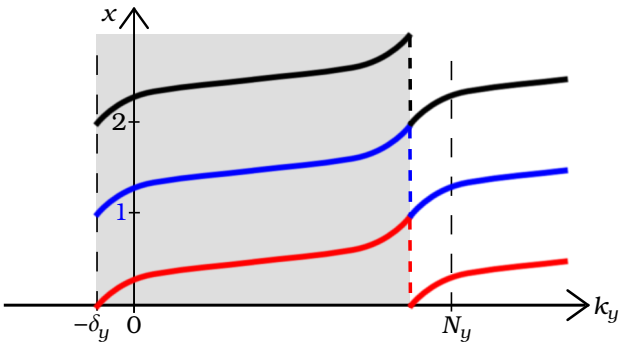

Figure 4.2: The principal Brillouin zone for $C = +1$. Plotted are the flows of the Wannier center position $\chi^{X,k_y} = X - \arg[W_x(k_y)]/(2\pi)$ [Eq. (4.30)] as a function of k_y, color-coded according to the unit cell index X. The movement of the Wannier center in each unit cell is monotonic in the principal Brillouin zone $Ck_y + \delta_y \in [0 \,..\, N_y)$ (marked by the gray shade), but not monotonic in the Brillouin zone $k_y \in [0 \,..\, N_y)$.

For models with inversion symmetry, it is not hard to see that δ_y is fixed to

$$\delta_y = \begin{cases} 0 & \text{if } W_x(0) = 1; \\ N_y/2 & \text{if } W_x(0) = -1 \text{ and } N_y \text{ even}; \\ (N_y - 1)/2 & \text{if } W_x(0) = -1 \text{ and } N_y \text{ odd}. \end{cases} \tag{4.36}$$

Then, for $Ck_y + \delta_y \in [0 \,..\, N_y)$, $\arg[W_x(k_y)]$ depends *monotonically* on k_y; $Ck_y + \delta_y$ labels the Wannier centers in an unit cell sequentially in ascending order of the center position χ^{X,k_y}. We refer to the set of k_y given by

$$Ck_y + \delta_y \in [0 \,..\, N_y) \tag{4.37}$$

as the "principal Brillouin zone" (pBZ). We introduce the 1D label of Wannier states

$$j^{X,k_y} = XN_y + Ck_y + \delta_y \tag{4.38}$$

with $Ck_y + \delta_y \in [0 \,..\, N_y)$. We need to shift k_y back to the pBZ *before* performing the mapping. Thanks to the explicit choice of the domain for k_y, the mapping $(X, k_y) \to j$ is invertible. In the presence of "zigzag" patterns in $W_x(k_y)$, we stick to the above j^{X,k_y} formula, and take δ_y as a variational parameter. This simple dependence on k_y is necessary for the translational invariance of the FQH-analog wave functions, as we

will see in Sec. 4.3.3. In the rest of this chapter we will focus on the case without "zigzag" patterns.

The phase factor $e^{i\Phi_y(X,k_y)}$ is subject to periodicity constraints. Since in the LLL $|j\rangle = |j+N_\phi\rangle$, the Wannier states $|X,k_y\rangle$ and $|X+N_x,k_y\rangle$ are mapped to the same LLL state. This mandates the gauge periodicity in X, i.e. $|X,k_y\rangle = |X+N_x,k_y\rangle$. Eq. (4.27) then leads to

$$e^{i\Phi_y(X,k_y)} = e^{i\Phi_y(X+N_x,k_y)}. \tag{4.39}$$

The periodic gauge of the Bloch state in the k_y direction, i.e. $|k_x,k_y\rangle = |k_x,k_y+N_y\rangle$, requires that

$$e^{i\Phi_y(X,k_y)} = e^{i\Phi_y(X,k_y+N_y)}. \tag{4.40}$$

It should be noted that the analogy between the Wannier states and the LLL states is not exact even in the continuum limit, due to the inevitable fluctuations in the Berry curvature. For example, if the Berry curvature is not uniform in the y direction, the Wannier centers χ^{X,k_y} are not distributed evenly over each unit cell, in contrast to the uniform distribution of the LLL orbitals. This is in line with the comparison between the LLL and the Chern band made in Refs. [68, 34].

4.3 Wannier construction of quantum Hall states

We now turn to the construction of model wave functions in a fractional Chern insulator defined on an $N_x \times N_y$ lattice. We consider finding model wave functions that approximate the ground states of generic density-density interaction with translational invariance, namely

$$V_{\text{lat}} = \sum_{(\mu,\nu,\boldsymbol{\delta})} \sum_{\mathbf{r}} \psi^\dagger_{\mathbf{r}+\boldsymbol{\delta},\mu} \psi^\dagger_{\mathbf{r},\nu} \psi_{\mathbf{r},\nu} \psi_{\mathbf{r}+\boldsymbol{\delta},\mu}, \tag{4.41}$$

Here $\boldsymbol{\delta}$ is the unit cell displacements between neighboring orbitals μ and ν. The sum $(\mu, \nu, \boldsymbol{\delta})$ is over all distinct (up to lattice translation) orbital pairs within some interaction range. The Bravais lattice coordinate $\mathbf{r} = (x, y) \in \mathbb{Z}^2$ is summed over the principal region of the torus. Longer range interactions can also be implemented, but our experience is that they diminish the strength of the FQH-like state.

In the flat-band limit of the single band approximation [74], the interacting Hamiltonian is just the projected density-density interaction $PV_{\text{lat}}P$:

$$H_{\text{lat}} = \frac{1}{N_\phi} \sum_{\{\mu,\nu,\boldsymbol{\delta}\}} \sum_{\mathbf{k}_1\mathbf{k}_2\mathbf{k}_3\mathbf{k}_4} \delta'_{\mathbf{k}_1+\mathbf{k}_2,\mathbf{k}_3+\mathbf{k}_4}\, e^{-i(\mathbf{k}_1-\mathbf{k}_4)\cdot\boldsymbol{\delta}} \times u^*_\mu(\mathbf{k}_1) u^*_\nu(\mathbf{k}_2) u_\nu(\mathbf{k}_3) u_\mu(\mathbf{k}_4)\, \psi^\dagger_{\mathbf{k}_1} \psi^\dagger_{\mathbf{k}_2} \psi_{\mathbf{k}_3} \psi_{\mathbf{k}_4}. \quad (4.42)$$

Here $\mathbf{k}_n = (k_{x,n}, k_{y,n})$, $n = 1, 2, 3, 4$, are summed over the first Brillouin zone, and the primed Kronecker-δ allows umklapp processes $\mathbf{k}_1 + \mathbf{k}_2 = \mathbf{k}_3 + \mathbf{k}_4 \bmod (N_x, N_y)$.

Based on the physics of the FQH, we expect that the Hamiltonian in Eq. (4.42) could have a topological ground state at filling $\nu = 1/q$ that resembles the Laughlin state. The Laughlin state expansion in non-interacting many-body states is known and hence all we need for a model FCI state is an appropriate map between the FCI single-particle orbitals and those of the LLL. The relevance of these trial wave functions to the actual FCI ground state is demonstrated in Sec. 4.4. We now examine the details of this construction.

For a flat-band single-particle lattice Hamiltonian, the many-body Hilbert space is spanned by the Slater determinant states $|\{X, k_y\}\rangle$. The 1D index j^{X,k_y} defined in Eq. (4.38) provides a formal mapping between the many-body basis states $|\{X, k_y\}\rangle$ on the lattice and $|\{j\}\rangle$ in the continuum. The lattice analogue of $|\Psi; s, r\rangle$ states can be constructed:

$$|\Psi; s, r\rangle_{\text{lat}} = \sum_{\{X,k_y\}} |\{X, k_y\}\rangle \, \langle\{j^{X,k_y}\}|\Psi; s, r\rangle, \quad (4.43)$$

where $\langle\{j^{X,k_y}\}|\Psi;s,r\rangle$ are the FQH amplitudes of the states defined in Eq. (4.12), and $\{X,k_y\}$ is summed over all N_e-particle configurations in the Wannier basis.

Naively, this seems to be the end of the story. However, the state $|\Psi;s,r\rangle_{\text{lat}}$ defined above is *not* covariant under a single-particle gauge transform on $|X,k_y\rangle$, as the continuum states $|j\rangle$ do *not* transform accordingly. We have to fix the phase $e^{i\Phi_y(X,k_y)}$ of the Wannier states $|X,k_y\rangle$ in conformity with the phase of the $|j\rangle$ states. This is not surprising: following Ref. [71], up to now we have only established a mapping between the state *labels* (X,k_y) and j, rather than a mapping between the actual *states*. In the following, we seek the guidelines for choosing $e^{i\Phi_y(X,k_y)}$ based on the similarity with the LLL. If we do not properly fix the $e^{i\Phi_y(X,k_y)}$ phase, the overlaps with the exact ground states can be tiny.

4.3.1 Connection between Wannier states

For the LLL orbitals $|j\rangle$ defined in Eq. (4.3), by brute-force calculation we find that the adjacent orbitals satisfy

$$\langle j|e^{-i\mathbf{G}_2\cdot\widetilde{\mathbf{r}}}|j+1\rangle = e^{-|\mathbf{G}_2|^2 l_B^2/4} \in \mathbb{R}_+. \tag{4.44}$$

Here, $\mathbf{G}_2 = 2\pi(\hat{e}_y - \cot\theta\,\hat{e}_x)/L_2$ is the reciprocal lattice vector defined in Eq. (4.1) in Sec. 4.1, and the position operator $\widetilde{\mathbf{r}}$ takes values in the continuum. We can interpret $e^{-i\mathbf{G}_2\cdot\widetilde{\mathbf{r}}}$ as a translation by $-\mathbf{G}_2$ in the momentum space.

This condition spells out the gauge choice of the LLL orbitals. In the continuum limit, it gives the parallel transport between the $|j\rangle$ and $|j+1\rangle$ orbitals. We need to find a consistent gauge for the Wannier states. Recall that $\widehat{Y}$ implements translation in the momentum space along k_y, which is the direction reciprocal to $\mathbf{b}_2$. Therefore, on a lattice, the quantity analogous to $\langle j|e^{-i\mathbf{G}_2\cdot\widetilde{\mathbf{r}}}|j+1\rangle$ is the connection between adjacent Wannier states

$$\langle X,k_y|\widehat{Y}|X',k_y'\rangle. \tag{4.45}$$

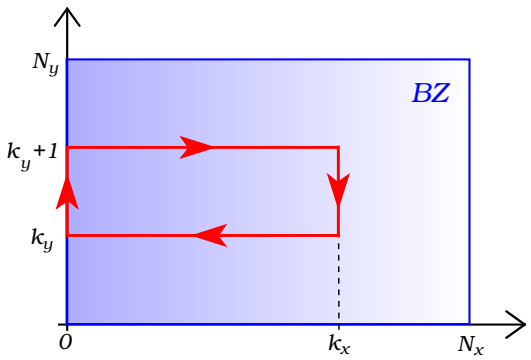

Figure 4.3: The loop $(0,k_y)(0,k_y+1)(k_x,k_y+1)(k_x,k_y)(0,k_y)$ in the $N_x \times N_y$ lattice Brillouin zone. The Wilson loop around this path is defined in Eq. (4.49) as $W_{\blacksquare}(k_x,k_y)$. Notice that at $k_x = N_x$, the connections at the two vertical edges cancel each other due to periodic boundary, leading to $W_{\blacksquare}(N_x,k_y) = W_x(k_y)/W_x(k_y+1)$.

Here, in the same spirit as the orthogonality fix for $|X,k_y\rangle$, we use the *unitary* projected position operator $\widehat{Y}$, defined in Eq. (4.24), and (X',k_y') is the label of the Wannier state *next* to $|X,k_y\rangle$, defined by

$$j^{X',k_y'} = j^{X,k_y} + C. \tag{4.46}$$

Plugging in the definition of j^{X,k_y} in Eq. (4.38), we find $k_y' = k_y + 1 \bmod N_y$. If going from k_y to k_y+1 crosses the boundary of the principal Brillouin zone [Eq. (4.37)], the Wannier centers (X,k_y) and (X',k_y') are located in different unit cells $(X' = X + C)$, otherwise they are in the same unit cell $(X' = X)$. Notice that for $|C| > 1$, Eq. (4.46) breaks the N_xN_y Wannier states into $|C|$ groups, and it implies a $|C|$-layer FQH analogy [7].

We can calculate the Wannier connection $\langle X,k_y|\widehat{Y}|X',k_y'\rangle$ by expanding the Wannier states in Bloch basis using Eq. (4.27). Since the operator $\widehat{Y}$ is diagonal in k_x, the two Bloch basis expansions is reduced into a single sum over k_x. Consider a generic term k_x in the sum. The A_x factors from the Wannier states and the A_y factor from $\widehat{Y}$ can be collected into a Wilson line going along $(0,k_y+1)(k_x,k_y+1)(k_x,k_y)(0,k_y)$, which equals $A_y(0,k_y)$ times the Wilson loop around the path shown in Fig. 4.3. The λ_x factors from the Wannier states are $[\lambda_x(k_y+1)/\lambda_x(k_y)]^{k_x}$. If the two Wannier

states are not in the same unit cell, they must be in adjacent unit cells $X' = X + C$ [due to Eq. (4.46)], and we have another factor $e^{i2\pi k_x C/N_x}$.

Putting all these together, for (X', k_y') defined in Eq. (4.46), we have the expression

$$\langle X, k_y|\widehat{Y}|X', k_y'\rangle = \frac{e^{i\Phi_y(X',k_y')}}{e^{i\Phi_y(X,k_y)}} A_y(0,k_y)\,\mathcal{U}_y(k_y), \tag{4.47}$$

where the gauge-invariant quantity $\mathcal{U}_y(k_y)$ is defined as

$$\mathcal{U}_y(k_y) = \frac{1}{N_x}\sum_{k_x}^{N_x} \frac{W_{\blacksquare}(k_x,k_y)}{\overline{W}_{\blacksquare}(k_x,k_y)}. \tag{4.48}$$

Here, $W_{\blacksquare}(k_x,k_y)$ is the unitary Wilson loop in Fig. 4.3,

$$W_{\blacksquare}(k_x,k_y) = \frac{\prod_\kappa^{k_x} A_x(\kappa,k_y)}{\prod_\kappa^{k_x} A_x(\kappa,k_y+1)} \frac{A_y(k_x,k_y)}{A_y(0,k_y)}, \tag{4.49}$$

while $\overline{W}_{\blacksquare}(k_x,k_y) = [\mu_x(k_y)]^{k_x}$ is given by $\mu_x(k_y)$ defined over the principal Brillouin zone [pBZ, the set of κ satisfying $C\kappa + \delta_y \in [0\,..\,N_y)$],

$$\mu_x(k_y) = \begin{cases} \dfrac{\lambda_x(k_y)}{\lambda_x(k_y+1)} & \text{if } k_y+1 \in \text{pBZ}, \\ e^{i2\pi C/N_x}\dfrac{\lambda_x(k_y)}{\lambda_x(k_y+1)} & \text{otherwise.} \end{cases} \tag{4.50}$$

We emphasize that the above definition requires first shifting k_y back to the pBZ. The two cases in Eq. (4.50) correspond to whether or not going from k_y to k_y+1 crosses the boundary of the pBZ.

We now try to understand $\mu_x(k_y)$ and $\overline{W}_{\blacksquare}(k_x,k_y)$ physically. Without loss of generality, we consider the case of $C = +1$. Since $[\lambda_x(k_y)]^{N_x} = W_x(k_y)$ [Eq. (4.25)], we have for both cases of Eq. (4.50),

$$[\mu_x(k_y)]^{N_x} = \left[\frac{\lambda_x(k_y)}{\lambda_x(k_y+1)}\right]^{N_x} = W_{\blacksquare}(N_x,k_y). \tag{4.51}$$

Now we need to take the N_x-th root of this equation. Special care needs to be taken with the branch choice. Recall from Sec. 4.2.1 that $\arg[\lambda_x(\kappa)]$ lies in $(-2\pi/N_x, 0]$ by definition. Since we assume the absence of "zigzag" patterns in the winding of $W_x(\kappa)$, the motion of $\arg[\lambda_x(\kappa)]$ in the interval $(-2\pi/N_x, 0]$ must be monotonic when

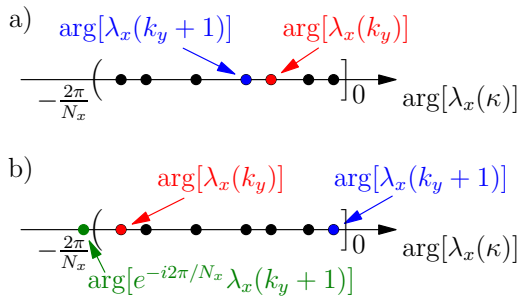

Figure 4.4: Flow of $\arg[\lambda_x(\kappa)]$ in the interval $(-2\pi/N_x, 0]$. The solid dots represents the N_y values of $\arg[\lambda_x(\kappa)]$ for the N_y Wannier centers in each unit cell. Here we show the case of $C = +1$: $\arg[\lambda_x(\kappa)]$ is a monotonically decreasing function of κ in the pBZ. Panel a) When k_y and $k_y + 1$ can be put in the principal Brillouin zone simultaneously, we have $\arg[\lambda_x(k_y)/\lambda_x(k_y + 1)] \in (0, 2\pi/N_x)$. Panel b) When going from k_y to $k_y + 1$ crosses the boundary of the principal Brillouin zone, we have $\arg[e^{i2\pi/N_x}\lambda_x(k_y)/\lambda_x(k_y + 1)] \in (0, 2\pi/N_x)$. Summarizing both cases, we have $\arg[\mu_x(k_y)] \in (0, 2\pi/N_x)$, for $\mu_x(k_y)$ defined in Eq. (4.50).

$\kappa \in$ pBZ, and $\arg[\lambda_x(\kappa)]$ jumps from the left boundary of the interval to the right boundary when κ crosses the boundary of the pBZ. As illustrated in Fig. 4.4, for all values of k_y, we have $\arg[\mu_x(k_y)] \in (0, 2\pi/N_x)$. On the other hand, since the phase angle of the Wilson loop is given by the curvature enclosed in the loop, the argument angle $\arg[W_{\blacksquare}(N_x, k_y)] \in [0, 2\pi)$ is the total curvature enclosed in the N_x plaquettes in the row between k_y and $k_y + 1$. Then, the N_x-th root of Eq. (4.51) gives

$$\arg[\mu_x(k_y)] = \frac{1}{N_x}\arg[W_{\blacksquare}(N_x, k_y)], \tag{4.52}$$

Therefore the argument angle $\arg[\overline{W}_{\blacksquare}(k_x, k_y)] = k_x \arg[\mu_x(k_y)]$ is k_x/N_x times the total curvature enclosed in the N_x plaquettes in the row between k_y and $k_y + 1$. When the curvature is constant across the N_x plaquettes at k_y, we have $\overline{W}_{\blacksquare}(k_x, k_y) = W_{\blacksquare}(k_x, k_y)$. The phase of each term in $\mathcal{U}_y(k_y)$ [Eq. (4.48)] can hence be interpreted as a measure of curvature fluctuations in the k_x direction.

4.3.2 Phase fixing: explicit prescription

Compared with $\langle j|e^{-i\mathbf{G}_2\cdot\tilde{\mathbf{r}}}|j+1\rangle \in \mathbb{R}_+$ in the LLL [Eq. (4.44)], a major difference in the Chern band is that the connection $\langle X, k_y|\widehat{Y}|X', k_y'\rangle$ between the Wannier states *cannot* be gauge fixed to a real number. To see this, we take the product of Eq. (4.47) over all (X, k_y). Thanks to the periodicity of $e^{i\Phi_y(X,k_y)}$ [Eqs. (4.39) and (4.40)], the product takes a simple form:

$$\prod_{X}^{N_x}\prod_{k_y}^{N_y}\langle X, k_y|\widehat{Y}|X', k_y'\rangle = \left[W_y(0)\prod_{k_y}^{N_y}\mathcal{U}_y(k_y)\right]^{N_x}, \tag{4.53}$$

Without further constraints from symmetry, the expression on the right hand side is a complex, rather than a positive real number. Even if we ignore the curvature fluctuations, in general we still *cannot* make all $\langle X, k_y|\widehat{Y}|X', k_y'\rangle \in \mathbb{R}_+$. This is fundamentally different from the LLL [Eq. (4.44)].

Hence, we relax this condition and look for $e^{i\Phi_y(X,k_y)}$ that makes the *phase* of $\langle X, k_y|\widehat{Y}|X', k_y'\rangle$ *independent* from X and k_y. [6] This phase is given by the N_ϕ-th root of the right hand side of Eq. (4.53). Define the phase $U_y(k_y) = \mathcal{U}_y(k_y)/|\mathcal{U}_y(k_y)|$. Similar to the phase $\lambda_y(k_x)$ for the connection $A_y(k_x, k_y)$ [Eq. (4.25)], we can define a phase ω_y with argument angle in $(-\pi/N_y, \pi/N_y]$ by

$$(\omega_y)^{N_y} = \prod_{\kappa}^{N_y} U_y(\kappa). \tag{4.54}$$

Then, to have the phase of $\langle X, k_y|\widehat{Y}|X', k_y'\rangle$ independent from X and k_y, we can use

$$\langle X, k_y|\widehat{Y}|X', k_y'\rangle = \lambda_y(0)\,\omega_y\,|\mathcal{U}_y(k_y)|. \tag{4.55}$$

Here, we have picked a specific branch of the N_ϕ-th root of (the phase of) Eq. (4.53). We could have picked another gauge by putting on the right hand side of Eq. (4.55) an extra factor $e^{i2\pi w/N_\phi}$, with $w \in [0\ ..\ ])(]N_\phi$. However, this makes no difference to the resulting set of many-body states $\{|\Psi; s, r\rangle_{\text{lat}}\}$ [Eq. (4.43)]. The reason is

[6] The absolute value of $\langle X, k_y|\widehat{Y}|X', k_y'\rangle$ does not depend on the choice of the phase $e^{i\Phi_y(X,k_y)}$. It is given by $|\mathcal{U}_y(k_y)|$.

the following. Without loss of generality, we consider the effect of this extra factor $e^{i2\pi w/N_\phi}$ in the case with $C > 0$. When we gauge fix the Wannier states one by one, using Eq. (4.55) but with an extra $e^{i2\pi w/N_\phi}$ between each pair of adjacent Wannier states, the Wannier state $|X, k_y\rangle$ receives an extra factor $e^{i2\pi w j^{X,k_y}/N_\phi}$. Therefore, the many-body state in Eq. (4.43) becomes

$$|\Psi; s, r\rangle^w_{\text{lat}} = \sum_{\{X,k_y\}} |\{X, k_y\}\rangle e^{i2\pi w \sum j^{X,k_y}/N_\phi} \langle\{j^{X,k_y}\}|\Psi; s, r\rangle, \tag{4.56}$$

Plugging in Eq. (4.15), we find

$$|\Psi; s, r\rangle^w_{\text{lat}} = e^{i2\pi w(\kappa_y + rN_e)/N_\phi} |\Psi; s + w, r\rangle_{\text{lat}}. \tag{4.57}$$

The w-dependence is reduced to an overall phase factor, and a shift in the s index, which can be absorbed by a reshuffling of s. Therefore, we can safely set w to zero, and use Eq. (4.55) to fix the phase of the Wannier states.

Plugging this prescription into Eq. (4.47), we find

$$e^{i\Phi_y(X',k'_y) - i\Phi_y(X,k_y)} = \frac{\lambda_y(0)}{A_y(0,k_y)} \frac{\omega_y}{U_y(k_y)}. \tag{4.58}$$

Notices that the quantities on the right hand side are all unitary. Together with the initial condition $e^{i\Phi_y(0,0)} = 1$, Eq. (4.58) recursively specifies the choice of $e^{i\Phi_y(X,k_y)}$ for all the N_ϕ states. Thanks to Eqs. (4.25) and (4.54), this choice of $e^{i\Phi_y(X,k_y)}$ does not depend on X, and we can drop the X argument and write $e^{i\Phi_y(k_y)}$ instead. We note that any choice of $e^{i\Phi_y(k_y)}$ without an X-dependence *that is periodic in* k_y can be achieved by simply modifying the gauge of the single-particle Bloch states along $k_x = 0$. This changes the phase of the Wannier states by $e^{i\eta(0,k_y)}$ as shown in Eq. (4.34).

4.3.3 Translational invariance

We now examine the translational symmetry of the many-body states $|\Psi; s, r\rangle$. For the moment we do not specialize to the phase choice in Eq. (4.58) and consider the constraint from translational invariance on a generic $e^{i\Phi_y(X,k_y)}$.

Define the N_e-particle center-of-mass translation operators on the lattice

$$\begin{aligned} T^x_{\text{lat,cm}} &= \sum_{\{x,y,\alpha\}} |\{x+1, y, \alpha\}\rangle\langle\{x, y, \alpha\}|, \\ T^y_{\text{lat,cm}} &= \sum_{\{x,y,\alpha\}} |\{x, y+1, \alpha\}\rangle\langle\{x, y, \alpha\}|. \end{aligned} \tag{4.59}$$

The action on the wave function of the many-body lattice state $|\Psi; s, r\rangle_{\text{lat}}$ defined in Eq. (4.43) is found to be

$$\langle\{X, k_y\}|T^x_{\text{lat,cm}}|\Psi; s, r\rangle_{\text{lat}} = e^{i\sum[\Phi_y(X,k_y)-\Phi_y(X-1,k_y)]}\langle\{X-1, k_y\}|\Psi; s, r\rangle_{\text{lat}}, \tag{4.60}$$

$$\langle\{X, k_y\}|T^y_{\text{lat,cm}}|\Psi; s, r\rangle_{\text{lat}} = e^{-i2\pi\sum k_y/N_y}\langle\{X, k_y\}|\Psi; s, r\rangle_{\text{lat}}, \tag{4.61}$$

where $\sum$ means summation over all the N_e phases of different quantum numbers $\{X, k_y\}$ of the N_e electron wave function. The translational invariance in the y direction is already apparent: Eq. (4.19) dictates that the non-vanishing components of $\langle\{X, k_y\}|\Psi; s, r\rangle_{\text{lat}}$ have the same value of $\sum k_y = C[\kappa_y + (r - \delta_y)N_e] \bmod N_y$. This is the total momentum K_y. The prefactor in Eq. (4.61) is the same for all the non-vanishing components, i.e. the wave function is translationally invariant in the y direction. The situation in the x direction is more involved. Plugging Eqs. (4.18) and (4.38) into Eq. (4.60), we have

$$\frac{\langle\{X, k_y\}|T^x_{\text{lat,cm}}|\Psi; s, r\rangle_{\text{lat}}}{\langle\{X, k_y\}|\Psi; s, r\rangle_{\text{lat}}} = e^{-i2\pi(\kappa_x+sN_e)/N_x}e^{i\sum[\Phi_y(X,k_y)-\Phi_y(X-1,k_y)]}. \tag{4.62}$$

In general, the exponential prefactor is different for each component (Slater determinants of different sets $\{X, k_y\}$), spoiling the translational invariance. To restore this symmetry, $e^{i\Phi_y(X,k_y)-i\Phi_y(X-1,k_y)}$ has to be *independent* from X and k_y. Translational invariance is part of the main reason why we also have asked for the phase of

$\langle X, k_y|\widehat{Y}|X', k_y'\rangle$ to be independent from X and k_y in the previous section. The periodic boundary condition on $e^{i\Phi_y(X,k_y)}$ then guarantees that the exponential prefactor is an N_x-th root of unity, and thus the state recovers translational invariance in the x direction.

We now consider the phase choice given in Sec. 4.3.2. Plugging Eq. (4.58) into Eq. (4.62), we have

$$\langle\{X, k_y\}|T^x_{\text{lat,cm}}|\Psi; s, r\rangle_{\text{lat}} = e^{-i2\pi(\kappa_x+sN_e)/N_x}\langle\{X, k_y\}|\Psi; s, r\rangle_{\text{lat}}, \tag{4.63}$$

where the relative momentum κ_x of the FQH state $|\Psi\rangle$ is defined by the eigenvalue of the relative translation operator T^x_{rel} in Eq. (4.5). Hence the FQH-analogue many-body wave functions $\langle\{X, k_y\}|\Psi; s, r\rangle_{\text{lat}}$ constructed through the Wannier functions using the above prescription are indeed translationally invariant. The total momentum of the N_e particles in state $|\Psi; s, r\rangle_{\text{lat}}$ is given by the wave numbers

$$K_x = \kappa_x + sN_e \bmod N_x, \quad K_y = C[\kappa_y + (r - \delta_y)N_e] \bmod N_y. \tag{4.64}$$

Ref. [16] obtained the counting for FCI model states from the corresponding counting for FQH model states by first folding the $N \times N$ relative Brillouin zone down to $N_{0x} \times N_{0y}$, and then unfolding to the $N_x \times N_y$ lattice Brillouin zone. We now show that our procedure precisely reproduces this folding picture.

Without loss of generality, we consider the case $C = +1$. Recall that $\text{GCD}(N_e, N_x) = N_{0x}$, $N_x = q_x N_{0x}$, $\text{GCD}(N_e, N_y) = N_{0y}$, $N_y = q_y N_{0y}$. For $s \in [0 \,..\, q_x)$, the q_x values of K_x are all distinct and can be written as $\kappa_x + t_x N_{0x}$ mod N_x with $t_x \in [0 \,..\, q_x)$. This clearly implements the folding rule in the x direction. In the y direction, for $r \in [0 \,..\, q/q_x)$, the q/q_x values of K_y form nothing but a $q/(q_x q_y)$-fold replica of the q_y values of $\kappa_y + t_y N_{0x}$ mod N_y with $t_y \in [0 \,..\, q_y)$. This corresponds to the folding rule in the y direction, producing $q/(q_x q_y)$ states in each momentum sector. The shift parameter δ_y can be absorbed into r and thus only reshuffles the order of K_y values. The results are thus in full agreement with Ref. [16].

In Ref. [96], the generalized Pauli principle [12, 13] was invoked through the Wannier mapping [71] to determine the *total* number of Moore-Read FCI quasihole states. Using our updated formalism, the number of quasihole states in each momentum sector could be found as well, and it is in agreement with the earlier results obtained in Ref. [96].

4.3.4 Many-body amplitudes in the Bloch basis

We are now in a position to give the final formula for the amplitudes of the many-body lattice states constructed from the FQH states $|\Psi; s, r\rangle$,

$$\langle\{k_x, k_y\}|\Psi; s, r\rangle_{\text{lat}} = \prod \left\{ \frac{(\omega_y)^{k_y}}{\prod_\kappa^{k_y} U_y(\kappa)} \frac{[\lambda_y(0)]^{k_y}}{\prod_\kappa^{k_y} A_y(0,\kappa)} \frac{[\lambda_x(k_y)]^{k_x}}{\prod_\kappa^{k_x} A_x(\kappa, k_y)} \right\} \frac{1}{\sqrt{N_x}^{N_e}} \sum_{\{X\}} e^{-i2\pi \sum k_x X/N_x} \langle\{j^{X,k_y}\}|\Psi; s, r\rangle. \quad (4.65)$$

Here the product outside the curly braces is over the (k_x, k_y) configurations of the N_e particles, and $\langle\{j^{X,k_y}\}|\Psi; s, r\rangle$ are the many-body amplitudes of the recombined FQH states [Eq. (4.12)]. The above formula is the central result of this chapter. This prescription is not limited to a specific model wave function. It applies to *any FQH state* that can be expressed in a second-quantized basis; a real-space wave function is not actually needed. We note that the absolute value of each component in the Bloch basis does not depend on the gauge choice of the Wannier states, thanks to the X-independence of $e^{i\Phi_y(X,k_y)}$.

4.4 Numerical tests

We perform the Wannier construction in the five fermionic lattice models studied in the previous chapter at filling $\nu = 1/3$: the checkerboard lattice model [87], the Haldane model on the honeycomb lattice [40], a two-orbital model that resembles half (spin-up) of the mercury-telluride two-dimensional topological insulator [15], the

Kagome lattice model with spin-orbit coupling between nearest neighbors [88], and the spin-polarized ruby lattice model [45]. For each model, we use the parameter set specified previously [74, 99] and focus on the lattice sizes and aspect ratios where the system has a threefold quasi-degenerate ground state in numerics well separated from the excited states. These are all inversion symmetric models, for which we list the values of $W_x(0)$, $W_y(0)$, and C for each model in Table 4.1.

We obtain the Laughlin FCI states on the lattice using the formalism described in this chapter, i.e. replacing $|\Psi\rangle$ in Eqs. (4.12) and (4.65) by the Laughlin FQH states on the torus in the continuum. The threefold Laughlin FQH states are obtained by numerically diagonalizing the FQH model Hamiltonian with only the first pseudopotential, $V_m = \delta_{m,1}$. As detailed in Sec. 4.2.3, the continuum torus for the FQH calculations has the same aspect ratio as the lattice system, and the twist angle θ of the five models are given in the last column of Table 4.1. The three Laughlin states are exact replicas except for a shift in the total momentum κ_y. As shown in Sec. 4.1.1, they can be recombined into $|\Psi; s, r\rangle$ and then mapped to the lattice using the Wannier basis. We will refer to the resulting lattice states as the Laughlin FCI states, as opposed to the Laughlin FQH states in the continuum.

For all of the five models, we find that the Laughlin FCI states are indeed translationally invariant and inversion symmetric. In contrast, if we follow the prescription in Ref. [71], the resulting many-body states break the inversion symmetry for the

Table 4.1: Values of the Chern number C, the Wilson loops $W_x(0)$ and $W_y(0)$, and the twist angle θ of the corresponding FQH torus, for the five lattice models at the studied parameters.

Model	C	$W_x(0)$	$W_y(0)$	θ
Checkerboard	-1	$+1$	-1	$\pi/2$
Haldane	-1	$+1$	-1	$\pi/3$
Kagome	$+1$	$+1$	$+1$	$\pi/3$
Ruby	-1	-1	$+1$	$\pi/3$
Two-orbital	$+1$	-1	-1	$\pi/2$

checkerboard lattice model, the two-orbital model, and the Haldane model. The issue responsible for this is that the Wilson loop $W_y(0)$ equals -1 in these models at the studied parameter set.

4.4.1 Overlap

The relevance of the Laughlin FCI states can be checked by computing the overlap with the ground states obtained from exact diagonalization of the FCI models at filling $\nu = 1/3$ [74, 99].

The number and momenta of Laughlin FCI states (shown in Sec. 4.3.3) match those of the exact ground states obtained by exact diagonalization. When both N_x and N_y are divisible by 3, all of the threefold states have total momentum zero. In such cases with more than one state in a certain momentum sector, the states can mix and we do not have a one-one correspondence between the two groups of states to compute the overlaps. Instead, we first build the projector into the subspace spanned by the exact diagonalization states, then the projector into the subspace spanned by the Laughlin FCI states, and finally, we define the overlap to be the trace of the product of the two projectors, divided by the dimension of the subspace, i.e.

$$\frac{1}{3}\sum_{i}\sum_{s,r}\left|{}_{\text{lat}}\langle \text{ED}; i|\Psi; s, r\rangle_{\text{lat}}\right|^2, \tag{4.66}$$

where $|\text{ED}; i\rangle_{\text{lat}}$, $i = 1, 2, 3$ are the threefold ground states obtained from exact diagonalization, and the indices (s, r) are summed over the threefold Laughlin FCI states in the same momentum sector. This naturally generalizes the usual definition of overlap as the absolute square of the inner product. When the Laughlin FCI states appear at different momenta, we take the usual overlap with the exact diagonalization states.

Shown in Fig. 4.5 against the Hilbert space dimension are the overlap values between the Laughlin FCI states obtained by the Wannier construction and the exact ground states at filling $\nu = 1/3$, of the five models on a lattice of size 4×3, 5×3,

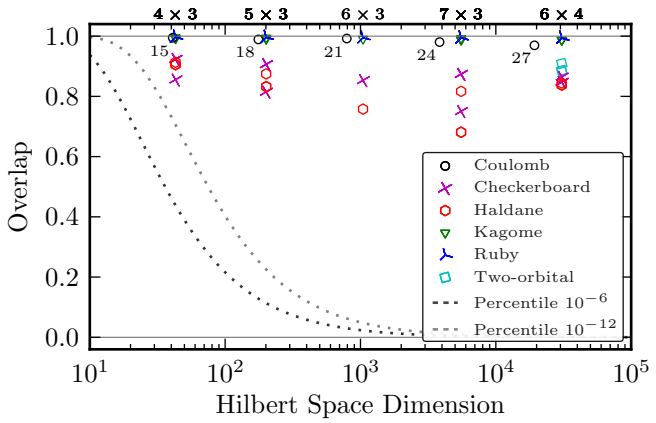

Figure 4.5: Overlap between variational states and the exact ground states. The size of the lattice is labeled by $N_x \times N_y$ at top. The plot includes the checkerboard lattice model (purple crosses), the Haldane model (red hexagons), the Kagome lattice model (green triangles), the ruby lattice model (blue Y-shapes), and the two-orbital model (cyan squares). The Wannier construction is performed using the $|X, k_y\rangle$ basis. At 6×3, the three states in a multiplet are in the same momentum sector, and thus there is one overlap value for each model. At other lattice sizes, two out of the three states have identical overlap due to inversion symmetry. Also shown is the overlap between the FQH ground state of the Coulomb interaction at filling $\nu = 1/3$ and the Laughlin model state, denoted by black circles and labeled by the number of flux N_ϕ. As a baseline, we also plot the top 10^{-6} and 10^{-12} percentiles (gray lines) of the overlap values *between random unit vectors* as a function of the Hilbert space dimension.

6×3, 7×3, and 6×4. The only exception is the two-orbital model: it does not have a *gapped* threefold quasi-degenerate ground state when $N_y = 3$, as we discussed in the previous chapter. At 6×3 the threefold states have the same total momentum, and thus there is only one overlap value for each model. At other lattice sizes, two of the threefold states form an inversion pair and have the same overlap value. Also shown in Fig. 4.5 are the overlap values between the Laughlin state and the FQH ground state of the Coulomb interaction on a torus with unity aspect ratio, pierced by $N_\phi = 15, 18, 21, 24, 27$ fluxes.

We find that at comparable Hilbert space sizes, the overlap for the Kagome lattice model and the ruby lattice model are comparable with or *even higher* than the overlap for the Coulomb interaction in the continuum, while the overlap for the Haldane model, the two-orbital model, and the checkerboard lattice model have slightly

lower overlap than the Coulomb interaction. We note one possible reason for the higher overlaps in the FCI systems. The lattice interactions used in the FCI models are Hubbard interactions between the nearest neighbors. Their short-ranged nature is preserved by the mapping to the LLL via the *localized* Wannier states, and thus the FCI interaction in the Wannier/LLL basis maybe be closer to the Laughlin pseudopotential Hamiltonian, compared with the long-range Coulomb interaction in the continuum. We emphasize that the overlap with the Laughlin FCI state should be interpreted in the context of the size of the Hilbert space. This is illustrated in Fig. 4.5 by the plot of the top 10^{-6} and 10^{-12} percentile values of the overlap between complex random unit vectors, as a function of the Hilbert space dimension.

We observe a slight decreasing trend in the overlap as the system size increases, much slower than the exponential decay of the random overlap. There is also an upward kink when going from 7×3 to 6×4 for the checkerboard lattice and the Haldane models. This agrees with the finding in Ref. [74] that the topological phase is more stable when the aspect ratio is closer to unity.

4.4.2 Mapping parameters revisited

In the previous section, the shift parameter δ_y for the Wannier-LLL mapping and the twist angle θ of the continuum torus used in the FQH calculations were set according to the discussions in Sec. 4.2.3. We now revisit the choice of δ_y and θ by checking explicitly how it affects the overlaps with the FCI ground states.

First we perform the Wannier constructions for the five models using the θ angle specified in Table 4.1, but we vary the shift parameter δ_y over $[0 \,..\, N_y)$. In Fig. 4.6, we show the dependence of the overlaps on δ_y for 6×4 and 6×3 lattices. At $N_y = 4$ (even), for the three models with $W_x(0) = +1$, namely (see Table 4.1), the Kagome lattice model, the checkerboard lattice model, and the Haldane model, the Laughlin FCI states have significant overlaps with the exact diagonalization ground states only

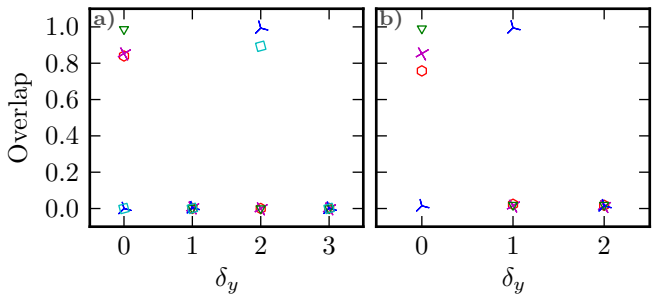

Figure 4.6: Overlaps between the Laughlin FCI states and the exact diagonalization states, as a function of the shift parameter δ_y in the Wannier-LLL mapping. Please refer to the legend and caption of Fig. 4.5 for the annotation of scatter symbols. The left (right) panel shows the calculations on a 6×4 (6×3) lattice. For clarity, for each model at each δ_y we show the average overlap of the threefold states. The two-orbital model is not included in the 6×3 calculation, as it does not have a gapped topological ground state at this lattice size. The values of δ_y that produce significant overlaps are in full agreement with Eq. (4.36).

at $\delta_y = 0$; for the two models with $W_x(0) = -1$, namely, the ruby lattice model and the two-orbital model, the significant overlaps appear at $\delta_y = 2 = N_y/2$. At $N_y = 3$ (odd), the significant overlaps for the three models with $W_x(0) = +1$ are still at $\delta_y = 0$, but for the ruby lattice models with $W_x(0) = -1$, the peak in overlap is shifted to $\delta_y = 1 = (N_y - 1)/2$.[7] The above results are in full agreement with the choice of δ_y in Eq. (4.36).

We now put δ_y to the values specified by Eq. (4.36), but vary the twisted angle θ of the continuum torus for FQH calculations. The overlaps as a function of θ are shown in Fig. 4.7. For each of the five models, we find a clear peak in overlap centered around the value of θ suggested in Sec. 4.2.3, as shown in Table 4.1. This confirms that our choice of the twist angle θ is appropriate.

[7]The two-orbital model is not included in the 6×3 calculations, because this model does not have a gapped topological ground state at this lattice size.

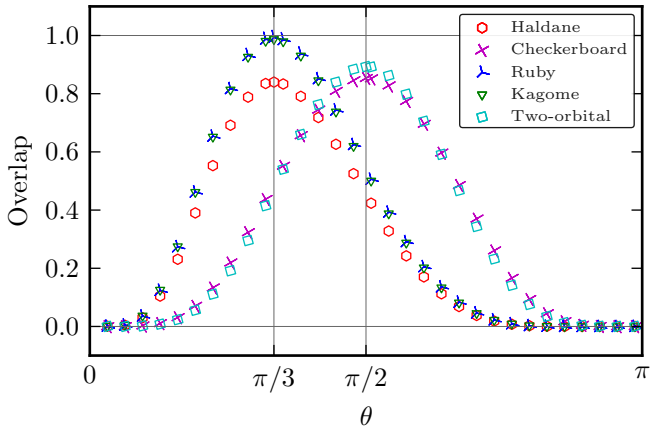

Figure 4.7: Overlaps between the Laughlin FCI states and the exact diagonalization states on a 6×4 lattice, as a function of the twist angle θ of the continuum torus for the FQH calculations. For clarity, for each model at each δ_y we show the average overlap of the threefold states. For each model, a peak in overlap is clearly visible at the value of θ given in Table 4.1, in accordance with the discussion in Sec. 4.2.3.

4.4.3 Entanglement spectrum

Overlap only provides an overall, sometimes inaccurate [81, 75] estimate on the similarity between two states. To compare the correlations in the Laughlin FCI states and the ground states, we now turn to their particle entanglement spectra.

First introduced by Li and Haldane [53], the entanglement spectrum examines the information imprinted in a many-body state. By effectively performing a spectral decomposition of the many-body state, the entanglement spectrum reveals the excitations supported by the state. Of particular interest in our study is the particle entanglement spectrum (PES), which encodes the characteristics of the quasihole excitations from the ground state [83]. We divide the N_e particles into two groups A and B of N_A and N_B particles respectively, trace out the degrees of freedom carried by the particles in B, and examine of the negative logarithm of the eigenvalues of the reduced density matrix ρ_A.

The Laughlin FQH state exhibits a highly non-trivial pattern in the PES: [53, 83, 16] In each momentum sector, the number of entanglement levels at finite entanglement energy matches the counting of the Laughlin quasiholes of N_A particles in qN_e

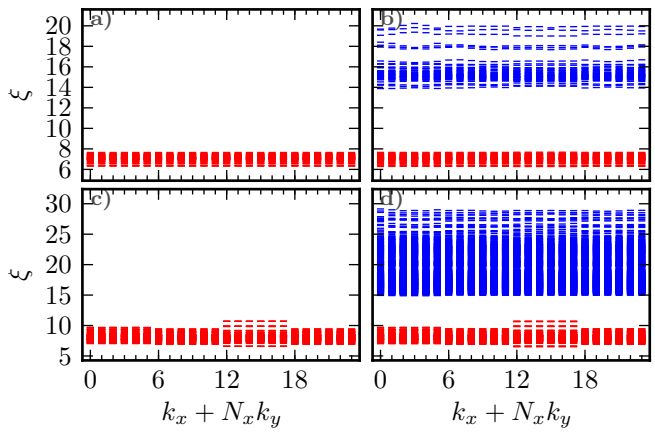

Figure 4.8: Particle entanglement spectrum of the Kagome lattice model of $N = 8$ particles on the $N_x \times N_y = 6 \times 4$ lattice. Shown in a) and b) are the spectra of the Laughlin FCI state and the exact ground state, respectively, with $N_A = 3$. Shown in c) and d) are the corresponding spectra with $N_A = 4$. In each momentum sector, we calculate the number of admissible configurations n, and color the lowest n entanglement energy levels in red and the rest in blue. The structure shown in the left panel exhibits the defining characteristic of the Laughlin state.

fluxes. The total number of levels, i.e. the number of non-zero modes of the reduced density matrix, is much smaller than the dimension of the reduced density matrix.

The PES of various FCI ground states at filling $\nu = 1/3$ has a low entanglement energy structure similar to the PES of the Laughlin state [74, 16, 99]. It also displays a non-universal high entanglement energy structure separated by an entanglement gap from the Laughlin-like structure. The number of levels below the gap at each total momentum matches the number of quasiholes folded to the lattice Brillouin zone [16]. An ideal Laughlin state in the FCI would exhibit an infinite entanglement gap.

For the Laughlin FCI model state obtained from the Wannier construction, we find a large number of zero modes in the reduced density matrix – corresponding to an infinite entanglement gap. The number of the finite entanglement energy levels is given exactly by the counting of Laughlin quasiholes folded to the lattice Brillouin zone. Writing the Laughlin FQH state in the Wannier basis is just a unitary transformation. Thus it does not modify the rank of the reduced density matrix,

and it preserves the entanglement spectrum of the Laughlin FQH state. An example is shown in Fig. 4.8. The entanglement energy levels below the gap of the exact diagonalization ground state exhibit almost identical structure in the spectra of the Laughlin FCI state and the ground state. The Laughlin FCI state captures a very important feature of the correlations in the FCI ground states. This further corroborates the proposal [74, 16] that the quasihole counting in the PES can be interpreted as a signature of a FQH-type of topological phase.

4.5 Discussion

In this chapter, we have studied the Wannier construction of FQH states for fractional Chern insulators with Chern number $C = 1$. Despite being first proposed more than a year ago [71], no overlap studies with the exact diagonalization have been reported. We have proposed a new, related prescription which fixes several outstanding issues in Ref. [71]. In particular, we highlight the gauge freedom in the 1D localized Wannier states and the restriction imposed by the Wilson loops. The key point is that the relative phase between adjacent Wannier states must follow the same pattern as the LLL orbitals in the Landau gauge, otherwise the states obtained from the FQH-FCI mapping are not relevant to the FCI problem.

We describe and justify in details a finite-size prescription for a generic lattice model with multiple sublattices. We provide an explicit, step-by-step recipe to construct the counterpart of any FQH wave function on a Chern insulator with $C = 1$. Our prescription is tailored for the torus geometry to make contact with existing numerical studies. It preserves the full translational invariance in both directions, as well as the inversion symmetry. We find the major obstacle to the Wannier construction to be the fluctuations in the Berry curvature. We try to accommodate the fluctuations in the localization direction in the gauge choice of the Wannier basis.

The fluctuations in the other direction keeps the Wannier centers from evenly spaced like the LLL orbitals, and we find no way to ameliorates the situation without spoiling translational invariance.

In a recent paper [16], a heuristic folding rule was discovered to relate the counting of the FQH states on a torus to the counting of the FCI states at each total momentum. It was established by arguing that the FCI phase on a lattice is in the same universality class as the FQH phase on a torus with δ-function lattice pinning potentials. In this chapter, the Wannier construction reorganizes the degenerate FQH model states and produces a set of model lattice states. These states have exactly the same counting in each total momentum sector of the energy and the entanglement spectra as predicted by the counting rule in Ref. [16]. This provides a concrete implementation of the folding rule that connects the FCI and the FQH effects.

We perform the Wannier construction for the Laughlin state numerically in the five $C = 1$ lattice models known to support a fractionalized phase. We find that the model state obtained from the Wannier construction and the actual FCI ground state have consistently large overlap in all cases, and their entanglement spectra exhibit very similar structures. The many-body physics in Chern insulators at filling $\nu = 1/3$ is indeed a close parallel to the Laughlin-type of FQH physics in the continuum with a strong magnetic field.

Our results provide another comparison across the array of known FCI models. Among the five models that we have checked, the ground states of the Kagome lattice model and the ruby lattice model have the largest overlap with the Laughlin model state. This is consistent with the finding in the previous chapter that these two models host the most stable Laughlin-type FCI phase among the five.

Chapter 5

Fractional Chern Insulators with an Arbitrary Chern Number

In the past two chapters, we examined the fractional Chern insulator (FCI) phases supported by a topological band with Chern number $C = 1$. This interacting lattice system turns out to be very well described by the conventional fractional quantum Hall (FQH) physics in the continuum. The correlated phases in Chern bands with $C > 1$, however, are more intricate. Numerical studies found both bosonic [95, 55, 84] and fermionic [55, 36] topological phases resembling the color SU(C) version of the Halperin [41] and the non-Abelian spin-singlet [4] (NASS) states [84], but with clear deviations [84] in the entanglement spectrum. In this chapter, we aim to understand these $C > 1$ FCI phases, and in particular, their relation to the conventional FQH states in a multicomponent lowest Landau level (LLL).

The main device in this study is a novel momentum-space basis in a C-component LLL that mimics the $N_x \times N_y$ Bloch states in the Chern band. These new one-body basis states entangle the color and the real spaces and form a single $N_x \times N_y$ Brillouin zone with flat Berry curvature and Chern number C, regardless of lattice size commensuration with C. This leads to a new mapping between FCI with arbitrary C

on a lattice of arbitrary size and a C-component FQH system. Our mapping operates directly in Bloch momentum space and utilizes the full lattice translational symmetry. For $C = 1$, this new construction is equivalent to the Wannier construction [71] discussed in the previous chapter, except for a new gauge fixing that further improves the overlaps. For $C > 1$, our model FCI states are equivalent to a new, color-dependent magnetic-flux inserted version of the Halperin or the NASS states, different from the existing proposal [7]. The FCI wave functions produced by our approach have the correct entanglement spectrum [99, 84]. We demonstrate large overlaps for previously unattained sizes between our model FCI wave functions and numerics for both $C = 1$ and the uncharted case of $C > 1$.

The one-body mapping also allows us to construct parent Hamiltonians of the model FCI states. We give a detailed analysis of the simplest bosonic pseudopotential Hamiltonian for the Halperin color-entangled states. We show that the pseudopotential Hamiltonian reduces to *almost* classical electrostatics in the hybrid Wannier basis, when we take the so-called thin-torus limit [89] and carry out truncations motivated by previous numerical results [84, 55]. This enables us to write down the form of its zero modes in this limit. However, in contrast to most well-known FQH states such as Laughlin and Read-Rezayi, a purely classical thin-torus description is not possible. We pinpoint the key difference from the conventional multicomponent FQH due to a subtle twist in the hybrid Wannier states, and detail the procedure to compute the total Bloch momentum of each zero mode. The resulting algorithm correctly predicts the degeneracy of the FCI quasiholes in each lattice momentum sector, without resorting to numerical diagonalization, and can be seen as the extension of the generalized Pauli principle [12, 13] to the color-entangled states.

5.1 Geometry of a Chern band

We first briefly discuss the geometry of the Bloch states in a Chern band. We consider a translationally invariant two-dimensional band insulator on an $N_x \times N_y$ lattice with N_o orbitals per unit cell indexed by b. The Bravais lattice is $m_x\mathbf{b}_x + m_y\mathbf{b}_y$, with $(m_x, m_y) \in \mathbb{Z}^2$ and the primitive translation vectors $\mathbf{b}_x$ and $\mathbf{b}_y$. We focus on a single Chern band of Bloch states $|\mathbf{k}\rangle$, labeled by momentum $\mathbf{k} = \sum_\alpha k_\alpha \mathbf{g}_\alpha$, with $k_\alpha \in \mathbb{Z}$ and $\mathbf{g}_\alpha \cdot \mathbf{b}_\beta = 2\pi\delta_{\alpha\beta}/N_\beta$ ($\alpha, \beta \in \{x, y\}$). We use $|\mathbf{k}\rangle$ and $|k_x, k_y\rangle$ interchangeably. The orbital b is embedded at $\boldsymbol{\epsilon}_b$ relative to its unit cell coordinate in real space [100]. The projected density in the Chern band is [68, 34, 16]

$$\rho_{\mathbf{q}} = \sum_{\mathbf{k}}^{\mathrm{BZ}} \left[\sum_b e^{-i\mathbf{q}\cdot\boldsymbol{\epsilon}_b} u_b^*(\mathbf{k}) u_b(\mathbf{k}+\mathbf{q}) \right] |\mathbf{k}\rangle\langle\mathbf{k}+\mathbf{q}|, \tag{5.1}$$

where $u_b(\mathbf{k})$ is the periodic part of the Bloch wave function. At $\mathbf{q} = \mathbf{g}_\alpha$, the bracketed factor in Eq. (5.1) gives the band geometry through the nonunitary exponentiated Abelian Berry connection, $\mathcal{A}_\alpha = \sum_b e^{-i\mathbf{g}_\alpha\cdot\boldsymbol{\epsilon}_b} u_b^*(\mathbf{k}) u_b(\mathbf{k}+\mathbf{g}_\alpha)$. $|\mathcal{A}_\alpha(\mathbf{k})|$ contains the quantum distance between $|\mathbf{k}\rangle$ and $|\mathbf{k}+\mathbf{g}_\alpha\rangle$, while $A_\alpha(\mathbf{k}) = \mathcal{A}_\alpha(\mathbf{k})/|\mathcal{A}_\alpha(\mathbf{k})|$ is the unitary Berry connection between them. We define $\rho_\alpha = \rho_{\mathbf{g}_\alpha}$.

The gauge-invariant Wilson loops (geometric phases) can be obtained by parallel transporting around a close loop over the BZ torus. All the contractible loops consist of a product of loops around a single plaquette, namely

$$\rho_x\rho_y[\rho_y\rho_x]^{-1} = \sum_{\mathbf{k}}^{\mathrm{BZ}} D(\mathbf{k})\, W_{\blacksquare}(\mathbf{k})\, |\mathbf{k}\rangle\langle\mathbf{k}|. \tag{5.2}$$

Here,

$$D(\mathbf{k}) = |\mathcal{A}_x(\mathbf{k})\mathcal{A}_y(\mathbf{k}+\mathbf{g}_x)\mathcal{A}_x^{-1}(\mathbf{k}+\mathbf{g}_y)\mathcal{A}_y^{-1}(\mathbf{k})| \in \mathbb{R} \tag{5.3}$$

is related to the nonuniformity of the quantum distance, and

$$W_{\blacksquare}(\mathbf{k}) = A_x(\mathbf{k})A_y(\mathbf{k}+\mathbf{g}_x)[A_y(\mathbf{k})A_x(\mathbf{k}+\mathbf{g}_y)]^\dagger \in \mathrm{U}(1) \tag{5.4}$$

is the unitary Wilson loop around the plaquette with its lower-left corner at $\mathbf{k}$. For large enough N_x and N_y, we can unambiguously extract the Berry curvature

$$f_{\mathbf{k}} = \frac{1}{2\pi} \Im \log W_{\blacksquare}(\mathbf{k}), \tag{5.5}$$

with finite-size normalization convention $\sum_{\mathbf{k}}^{\mathrm{BZ}} f_{\mathbf{k}} = C$. $\Im$ takes the imaginary part in the principal branch $\Im \log(z) \in (-\pi, \pi]$. This gives a sharp finite-size formula for the Chern number, $C = \frac{1}{2\pi} \mathrm{Tr} \Im \log[\rho_x \rho_y (\rho_y \rho_x)^{-1}]$. In addition to $W_{\blacksquare}(\mathbf{k})$, there are also two independent noncontractible Wilson loops on the torus, related to charge polarizations: the Wilson loop around $k_y = 0$, $W_x = \mathrm{Phase}\left[\langle \mathbf{0}|\rho_x^{N_x}|\mathbf{0}\rangle\right] = \langle N_x \mathbf{g}_x|\mathbf{0}\rangle \prod_{\kappa=0}^{N_x-1} A_x(\kappa \mathbf{g}_x)$, with $|\mathbf{0}\rangle \equiv |\mathbf{k} = \mathbf{0}\rangle$, and the Wilson loop W_y around $k_x = 0$ defined similarly.

The structure of geometric phases in the Chern band is fully specified by the collection of the Wilson loops $W_{\blacksquare}(\mathbf{k})$ and W_α, $\alpha = x, y$.

5.2 One-body states in a multicomponent lowest Landau level

In this section we construct a one-body basis in a multicomponent LLL that mimic the Bloch basis in a Chern band with an arbitrary Chern number C.[1]

We consider a C-component (generalized spin) electron moving on a torus with a perpendicular uniform magnetic field. The major difference between our approach and the usual treatment of the multicomponent LLL problem is the adoption of a new set of boundary conditions. This alternative choice entangles together the C components and enables us to construct a single manifold of Bloch states with Chern number C. In contrast to the usual picture of multicomponent LLL as C separate manifolds (one for each of the C components) each with unity Chern number, our

[1] In the following discussion we assume $C > 0$ for simplicity. The case of $C < 0$ can be handled by inverting, say, the x direction of the Landau level.

basis provides a natural foundation for the mapping to a single Chern band with an arbitrary Chern number C. The central result of this section is Eq. (5.24), the expansion of the electron density operator in the Bloch basis.

5.2.1 Translations operators

We consider electrons with C internal (color) degrees of freedom $|\sigma\rangle$, labeled by $\sigma \in \mathbb{Z}_C$. For simplicity, we work on a rectangular torus spanned by $\mathbf{L}_x = L_x\hat{x}$ and $\mathbf{L}_y = L_y\hat{y}$, where L_x and L_y are the two fundamental cycles of the torus, and $\hat{x}$ and $\hat{y}$ are orthonormal. The torus is pierced by a magnetic field in the $-\hat{e}_z$ direction, $\mathbf{B} = \nabla \times \mathbf{A} = B\hat{e}_z$ with $B < 0$. We denote by $e < 0$ the charge of the electron. The magnetic length is $l_B = \sqrt{\hbar/(eB)}$. We define the total number of fluxes N_ϕ penetrating the torus by $L_xL_y = 2\pi l_B^2 N_\phi$. Here we do *not* assume N_ϕ to be an integer as in the original treatment of the Landau level on a toroidal geometry [39]. As we will see soon, the alternative set of boundary conditions we pick only requires $CN_\phi \in \mathbb{Z}$. This integer is equal to the dimension of the one-body Hilbert space in the lowest Landau level. We define the magnetic translation operator $T(\mathbf{a}) = e^{-i\mathbf{a}\cdot\mathbf{K}/\hbar}$, where $\mathbf{K} = -i\hbar\nabla - e\mathbf{A}(\mathbf{r}) + e\mathbf{B}\times\mathbf{r}$ is the guiding center momentum. The translation $T(\mathbf{a})$ commutes with the one-body Landau Hamiltonian $H = (-i\hbar\nabla - e\mathbf{A})^2/(2m)$ but not with the translation $T(\mathbf{b})$ at a different displacement, $T(\mathbf{a})T(\mathbf{b}) = T(\mathbf{b})T(\mathbf{a})e^{i\hat{z}\cdot\mathbf{a}\times\mathbf{b}/l_B^2}$.

We need to make contact between the multicomponent Landau level states and the Bloch states in a Chern band. For the latter, we consider a single Bloch band with Chern number C in a tight-binding model on a lattice with $N_x \times N_y$ unit cells. The band has a total of N_xN_y one-body states, one at each lattice momentum in the $N_x \times N_y$ Brillouin zone (BZ). To make contact with this lattice system, we first look in the Landau level for a pair of commuting translation operators that also resolve an $N_x \times N_y$ BZ. To this end, we tune the magnetic field to match the number of one-body states, $CN_\phi = N_xN_y$, and we consider the magnetic translations over a

fictitious $N_x \times N_y$ unit cell structure of the continuous torus, namely,

$$T_x = T(\mathbf{L}_x/N_x), \quad T_y = T(\mathbf{L}_y/N_y). \tag{5.6}$$

The operator T_x (resp. T_y) has N_x (resp. N_y) different eigenvalues. As opposed to the $C = 1$ case, however, for generic C they do not commute due to the $N_\phi/(N_x N_y) = 1/C$ flux over each fictitious plaquette,

$$T_x T_y = T_y T_x e^{i2\pi/C}. \tag{5.7}$$

To compensate for this, we define the 'clock and shift' operators Q and P over the internal (color) Hilbert space by

$$P|\sigma\rangle = |\sigma + 1 \ (\mathrm{mod}\ C)\rangle, \qquad\qquad Q|\sigma\rangle = e^{i2\pi\sigma/C}|\sigma\rangle. \tag{5.8}$$

Both operators are unitary, and they satisfy

$$PQ = QPe^{-i2\pi/C}. \tag{5.9}$$

This leads to a pair of *commuting* composite operators

$$\widetilde{T}_x = T_x P, \quad \widetilde{T}_y = T_y Q. \tag{5.10}$$

We will refer to this pair as the 'color-entangled' magnetic translation operators. For the (color-neutral) Landau Hamiltonian, both operators are good symmetries, and they resolve an $N_x \times N_y$ Brillouin zone once we specify the boundary conditions. Notice that in general $[T(\mathbf{L}_x), \widetilde{T}_y] \neq 0$, $[T(\mathbf{L}_y), \widetilde{T}_x] \neq 0$. This means that we have to abandon the usual boundaries [39] $T(\mathbf{L}_\alpha) = 1$, $\alpha = x, y$. Instead, we adopt the color-entangled generalization $\widetilde{T}_\alpha^{N_\alpha} = 1$, namely,

$$T(\mathbf{L}_x)P^{N_x} = T(\mathbf{L}_y)Q^{N_y} = 1. \tag{5.11}$$

This alternative set of boundary conditions make it possible to construct two sets of basis states in the one-body Hilbert space with desirable properties spelled below.

We define the Bloch states $|\mathbf{k}\rangle$ as the simultaneous eigenstates of $\widetilde{T}_x$ and $\widetilde{T}_y$ within the LLL,

$$\widetilde{T}_\alpha|\mathbf{k}\rangle = e^{-i2\pi k_\alpha/N_\alpha}|\mathbf{k}\rangle, \tag{5.12}$$

with $\mathbf{k} = (k_x, k_y) \in \mathbb{Z}^2$. The N_xN_y states within the first Brillouin zone

$$1\mathrm{BZ} = [0\ ..\ N_x) \times [0\ ..\ N_y) \tag{5.13}$$

have distinct eigenvalues under $\widetilde{T}_\alpha$, and they constitute the Bloch basis in the $N_xN_y = CN_\phi$-dimensional Hilbert space of the C-component LLL.

We now look for the explicit wave function $\langle x, y, \sigma|\mathbf{k}\rangle$ for these basis states. We specialize to the Landau gauge $\mathbf{A} = Bx\hat{y}$. Consider the states $|X, k_y\rangle$ with $X, k_y \in \mathbb{Z}$ defined by the real- and internal-space wave function

$$\langle x, y, \sigma|X, k_y\rangle = \frac{1}{(\sqrt{\pi}L_y l_B)^{1/2}} \sum_m^{\mathbb{Z}} \delta^{\mathrm{mod}\ C}_{\sigma, X+mN_x} \exp\left\{ i2\pi\left(\tfrac{XN_y+k_yC}{C} + mN_\phi\right)\tfrac{y}{L_y} - \tfrac{1}{2}\left[\tfrac{x}{l_B} - \tfrac{2\pi l_B}{L_y}\left(\tfrac{XN_y+k_yC}{C} + mN_\phi\right)\right]^2 \right\}. \tag{5.14}$$

Here X, k_y are state labels taking integer values, while x, y are real space coordinates taking continuous values, and $\sigma \in \mathbb{Z}_C$ is a discrete coordinate in the internal color space. It is not hard to see that $|X, k_y\rangle$ belongs to the lowest Landau level, as the above wave function can be recast in the form $f(x + iy, \sigma)\, e^{-x^2/(2l_B^2)}$. Moreover, we find that $|X, k_y\rangle$ is periodic in X, but with a twist in k_y:

$$|X + N_x, k_y\rangle = |X, k_y\rangle, \quad |X, k_y + N_y\rangle = |X + C, k_y\rangle. \tag{5.15}$$

These relations are reminiscent of the flow of hybrid Wannier states discussed in the previous chapter. Further, as we prove in Appendix 5.A, the color-entangled magnetic translations [Eq. (5.10)] have a representation on $|X, k_y\rangle$ similar to the representation of the lattice translations on the hybrid Wannier states, namely,

$$\widetilde{T}_x|X, k_y\rangle = |X + 1, k_y\rangle, \quad \widetilde{T}_y|X, k_y\rangle = e^{-i2\pi k_y/N_y}|X, k_y\rangle. \tag{5.16}$$

We thus refer to these states as the hybrid Wannier states in the C-component LLL. It is easy to see the states with $X \in [0 \,..\, N_x)$ and $k_y \in [0 \,..\, N_y)$ are linearly independent. We emphasize that unless N_x is divisible by C, these states are *not* color eigenstates, in contrast to the states studied in Ref. [7].

We want to define the Bloch states in the LLL as a Fourier sum of the hybrid Wannier states,[2]

$$|\mathbf{k}\rangle = |k_x, k_y\rangle = \frac{1}{\sqrt{N_x}} \sum_{X}^{N_x} e^{i2\pi X k_x/N_x} |X, k_y\rangle. \tag{5.17}$$

From Eqs. (5.15) and (5.16), we find that the simultaneous eigenvalue equation in (5.12) indeed holds. These states are periodic in k_x, but only quasi-periodic in k_y,

$$|k_x + N_x, k_y\rangle = |k_x, k_y\rangle, \qquad |k_x, k_y + N_y\rangle = e^{-i2\pi k_x C/N_x} |k_x, k_y\rangle. \tag{5.18}$$

The latter non-periodicity signals the topological obstruction to a periodic smooth gauge due to the non-zero Chern number of a Landau level. [3]

5.2.2 Projected density operator

The density operator projected to the lowest Landau level plays a central role in the FQH physics, as it is used to define the inter-particle interaction. As we now show, this operator takes a particularly nice form in our Bloch basis.

By definition, the density operator of color σ at $\mathbf{r} = (x, y)$ projected to the LLL is given by

$$\rho(\mathbf{r}, \sigma) = \sum_{\mathbf{k}_1}^{\mathrm{BZ}} \sum_{\mathbf{k}_2}^{\mathrm{BZ}} |\mathbf{k}_1\rangle \phi^*_{\mathbf{k}_1}(\mathbf{r}, \sigma) \phi_{\mathbf{k}_2}(\mathbf{r}, \sigma) \langle \mathbf{k}_2|, \tag{5.19}$$

[2] Here and hereafter, the summation of the shorthand form $\sum_a^N$ stands for $\sum_{a=0}^{N-1}$.

[3] We can perform a gauge transformation to make the Bloch states periodic. However, the resulting wave function will not be smooth in k_x/N_x and/or k_y/N_y in the continuum limit $N_x, N_y \to \infty$. For example, for $k_y \in [mN_y \,..\, mN_y + N_y)$ with $m \in \mathbb{Z}$, we can take $|k_x, k_y\rangle \to e^{i2\pi k_x m C/N_x} |k_x, k_y\rangle$. This transformation makes the state periodic, but discontinuous at $k_y/N_y \in \mathbb{Z}$.

where $\phi_{\mathbf{k}}(\mathbf{r},\sigma) = \langle \mathbf{r},\sigma|\mathbf{k}\rangle$ is the wave function of the Bloch state $|\mathbf{k}\rangle$ defined in Eq. (5.17), and $\mathbf{k}_1, \mathbf{k}_2$ are each summed over a full BZ. [4] Since $\rho(\mathbf{r},\sigma)$ must have torus periodicity, we can express it as a Fourier sum,

$$\rho(\mathbf{r},\sigma) = \frac{1}{L_x L_y} \sum_{\mathbf{q}} e^{i\mathbf{q}\cdot\mathbf{r}} \rho_{\mathbf{q},\sigma}. \tag{5.20}$$

Here, the wave vector $\mathbf{q}$ lives on the reciprocal lattice

$$\mathbf{q} = \left(\frac{2\pi q_x}{L_x}, \frac{2\pi q_y}{L_y}\right), \quad (q_x, q_y) \in \mathbb{Z}^2. \tag{5.21}$$

The projected density operator in momentum space for a single color component σ is thus given by

$$\rho_{\mathbf{q},\sigma} = \sum_{\mathbf{k}_1}^{\mathrm{BZ}} \sum_{\mathbf{k}_2}^{\mathrm{BZ}} |\mathbf{k}_1\rangle\langle\mathbf{k}_2| \int \mathrm{d}\mathbf{r}\, e^{-i\mathbf{q}\cdot\mathbf{r}} \phi^*_{\mathbf{k}_1}(\mathbf{r},\sigma)\phi_{\mathbf{k}_2}(\mathbf{r},\sigma), \tag{5.22}$$

where $\int \mathrm{d}\mathbf{r}$ is over the torus $[0, L_x) \times [0, L_y)$. We define the full projected density operator $\rho_{\mathbf{q}}$ by

$$\rho_{\mathbf{q}} = \sum_{\sigma}^{C} \rho_{\mathbf{q},\sigma}. \tag{5.23}$$

This operator is the building block of a color-neutral interacting Hamiltonian. In Appendix 5.B, we finish the integral in Eq. (5.22) with the help of the sum over color σ, and prove the main result of this section,

$$\rho_{\mathbf{q}} = e^{-\mathbf{q}^2 l_B^2/4} \sum_{\mathbf{k}}^{\mathrm{BZ}} e^{-i2\pi q_x (k_y + q_y/2)/N_\phi} |\mathbf{k}\rangle\langle\mathbf{k}+\mathbf{q}|. \tag{5.24}$$

It should be noted that when N_x is divisible by C, the integral in Eq. (5.22) can be finished for each σ individually, without the color sum. The above formula can be recast as

$$\rho_{\mathbf{q}} = \sum_{\mathbf{k}}^{\mathrm{BZ}} |\mathbf{k}\rangle\langle\mathbf{k}+\mathbf{q}| \left\{ \exp\left[\frac{\pi}{2} \frac{L_x L_y}{N_x N_y} \left(\frac{q_x^2}{L_x^2} + \frac{q_y^2}{L_y^2} \right) - i2\pi \frac{q_x (k_y + q_y/2)}{N_x N_y} \right] \right\}^C. \tag{5.25}$$

[4] Any BZ choice is fine, and the two BZs for $\mathbf{k}_1$ and $\mathbf{k}_2$ do not have to be the same. It is easy to see that although $|\mathbf{k}\rangle$ is only quasi-periodic in k_y, $\rho(\mathbf{r},\sigma)$ does not depend on the choice of BZ for $\mathbf{k}_1$ or $\mathbf{k}_2$, thanks to the quasi-periodicity condition in Eq. (5.18).

Note that the dependence on C enters only through the exponent shared by all $\rho_{\mathbf{q}}$ and all terms in $\sum_{\mathbf{k}}$.

The above result suggests that the torus formed by the Bloch states $|\mathbf{k}\rangle$ is endowed with a rich geometric structure. As usual, the Berry connection between the BZ points $\mathbf{k}$ and $\mathbf{k}+\mathbf{q}$ is defined as (the phase of) the inner product between the periodic part of the Bloch states $|\mathbf{k}\rangle$ and $|\mathbf{k}+\mathbf{q}\rangle$. This amounts to the matrix element of the operator $e^{-i\mathbf{q}\cdot\hat{\mathbf{r}}}$ between the two states, where $\hat{\mathbf{r}}$ is the position operator. Notice that this exponentiated position operator, when projected to the lowest Landau level, is nothing but the full density operator $\rho_{\mathbf{q}}$ in Eq. (5.23). Therefore, we can interpret Eq. (5.24) as the parallel transport in the momentum space implemented by the projected density $\rho_{\mathbf{q}}$.

Define the primitive vectors on the reciprocal lattice $\mathbf{g}_x = (2\pi/L_x, 0)$ and $\mathbf{g}_y = (0, 2\pi/L_y)$, and the shorthand notations $\rho_\alpha = \rho_{\mathbf{q}=\mathbf{g}_\alpha}$ and $\text{Phase}[z] = z/|z|$ for $z \in \mathbb{C}$. At momentum transfer $\mathbf{q} = \mathbf{g}_\alpha$, the (unitary) exponentiated Berry connection resolves the band geometry,

$$A_\alpha(\mathbf{k}) \equiv \text{Phase}[\langle \mathbf{k}|\rho_\alpha|\mathbf{k}+\mathbf{g}_\alpha\rangle] = e^{-i2\pi q_x(k_y+q_y/2)/N_\phi}, \tag{5.26}$$

while the norm

$$\left|\langle \mathbf{k}|\rho_\alpha|\mathbf{k}+\mathbf{g}_\alpha\rangle\right| = e^{-\mathbf{q}^2 l_B^2/4} \tag{5.27}$$

is the quantum distance between $\mathbf{k}$ and $\mathbf{k}+\mathbf{g}_\alpha$. Notice that the quantum distance does not depend on $\mathbf{k}$.[5] The gauge-invariant Berry phases can be extracted from parallel transport around closed loops of $|\mathbf{k}\rangle$ states over the BZ torus.

Given that we are interested in the Abelian Berry connection, each contractible loop can be decomposed into a product of loops around single plaquettes. Such plaquette Wilson loops take a particularly nice form for the Bloch states we constructed.

[5] This is particular to the Landau level problem; in the tight-binding situation, both the quantum distance and the Berry phase depend on $\mathbf{k}$.

Around the plaquette at $\mathbf{k}$,

$$W_{\blacksquare}(\mathbf{k}) \equiv \text{Phase}[\langle \mathbf{k}|\rho_x\rho_y[\rho_y\rho_x]^{-1}|\mathbf{k}\rangle] = e^{i2\pi/N_\phi} \tag{5.28}$$

is independent from $\mathbf{k}$. Further, we can define the Berry curvature over a single plaquette [101] $f_{\mathbf{k}} = \frac{1}{2\pi}\Im \log W_{\blacksquare}(\mathbf{k})$, where $\Im$ takes the imaginary part in the principal branch $\Im \log z \in (-\pi, \pi]$. We find that the BZ torus for the multicomponent Landau level has constant Berry curvature $f_{\mathbf{k}} = \frac{1}{N_\phi}$, and its Chern number is equal to the number of components

$$\sum_{\mathbf{k}}^{\text{BZ}} f_{\mathbf{k}} = \frac{N_x N_y}{N_\phi} = C. \tag{5.29}$$

In addition to the contractible loops, there are two independent non-contractible Wilson loops around the two fundamental cycles of the torus, related to charge polarization. We define

$$\begin{aligned} W_x(k_y) &\equiv \text{Phase}[\langle 0, k_y|\rho_x^{N_x}|0, k_y\rangle] = e^{-i2\pi k_y C/N_y}, \\ W_y(k_x) &\equiv \text{Phase}[\langle k_x, 0|\rho_y^{N_y}|k_x, 0\rangle] = e^{i2\pi k_x C/N_x}. \end{aligned} \tag{5.30}$$

The geometric phases over the BZ torus are fully specified by the following quantities

$$\{W_{\blacksquare}(\mathbf{k})|\mathbf{k} \in \text{BZ}\}, W_x(0), W_y(0). \tag{5.31}$$

For example, $W_x(1)$ can be obtained from $W_x(0)$ times the product of $W_{\blacksquare}(\mathbf{k})$ around each of the N_x plaquettes between $k_y = 0$ and $k_y = 1$ in the first BZ.

We can easily add a twist to the color-entangled boundary conditions in Eq. (5.11),

$$T(\mathbf{L}_x)P^{N_x} = e^{-i2\pi\gamma_x}, \quad T(\mathbf{L}_y)Q^{N_y} = e^{-i2\pi\gamma_y}. \tag{5.32}$$

The twist angles $\boldsymbol{\gamma} = (\gamma_x, \gamma_y) \in \mathbb{R}^2$ implement color-independent magnetic flux insertions. We incorporate this change by keeping $(k_x, k_y) \in \mathbb{Z}^2$, but applying $\mathbf{k} \to \mathbf{k} + \boldsymbol{\gamma}$ to every equation in this section so far.

5.2.3 Generalized Coulomb gauge

Linking together the LLL $|\mathbf{k}\rangle$ and the lattice $|\mathbf{k}\rangle$ bases requires one additional step of gauge fixing, $|\mathbf{k}\rangle \to e^{i\zeta_{\mathbf{k}}}|\mathbf{k}\rangle$. After that, any many-body state $|\Psi\rangle_{\mathrm{L}}$ over our colorful LLL can be transcribed to the FCI [6],

$$|\Psi\rangle = \sum_{\{\mathbf{k}\}} e^{i\sum_{\mathbf{k}}\zeta_{\mathbf{k}}} |\{\mathbf{k}\}\rangle \times {}^{\boldsymbol{\gamma}}_{\mathrm{L}}\langle\{\mathbf{k}\}|\Psi\rangle_{\mathrm{L}}, \tag{5.33}$$

where ${}^{\boldsymbol{\gamma}}_{\mathrm{L}}\langle\{\mathbf{k}\}|$ is the color-entangled occupation-number basis in the LLL with twist $\boldsymbol{\gamma}$. In the following we describe the construction of the gauge transformation $e^{i\zeta_{\mathbf{k}}}$ for the lattice Bloch states. For clarity, we use a subscript/superscript L to distinguish the LLL quantities from those in a Chern band.

The connections over the lowest Landau level (LLL) Brillouin zone (BZ) are $A^{\mathrm{L}}_x(\mathbf{k}) = e^{-i2\pi k_y/N_\phi}$, and $A^{\mathrm{L}}_y(\mathbf{k}) = 1$ (superscript 'L' represents LLL). They satisfy the discrete analog of the Coulomb gauge condition, [7] i.e. they can be expressed in terms of a "stream function" $\phi^{\mathrm{L}}_{\mathbf{k}} = (k_y + 1/2)^2/(2N_\phi)$ as

$$A^{\mathrm{L}}_\alpha(\mathbf{k}) = \exp\Big(- i2\pi \sum_\beta \varepsilon_{\alpha\beta}\,[\mathrm{d}_\beta \phi^{\mathrm{L}}]_{\mathbf{k}}\Big). \tag{5.34}$$

Here, d_β is the backward finite difference operator, defined by $[\mathrm{d}_\beta\phi]_{\mathbf{k}} = \phi_{\mathbf{k}} - \phi_{\mathbf{k}-\mathbf{g}_\beta}$, and $\phi^{\mathrm{L}}_{\mathbf{k}}$ satisfies the discrete Poisson equation with curvature as source,

$$[\widetilde{\Delta}\phi^{\mathrm{L}}]_{\mathbf{k}} = 1/N_\phi, \tag{5.35}$$

with discrete Laplacian $\widetilde{\Delta}$ given by

$$[\widetilde{\Delta}\phi]_{\mathbf{k}} = \sum_{\mathbf{p}}^{\pm\mathbf{g}_x,\pm\mathbf{g}_y} (\phi_{\mathbf{k}+\mathbf{p}} - \phi_{\mathbf{k}})\,. \tag{5.36}$$

[6] For actual lattice calculations, it is desirable to use periodic gauge with $|\mathbf{k}\rangle = |\mathbf{k} + N_\alpha \mathbf{g}_\alpha\rangle$ (no sum implied). Simply restricting $\mathbf{k}$ to a single BZ would achieve this, as long as the BZ choice for the lattice system is consistent with that for the LLL.

[7] In the continuum limit [100], the exponentiated connections become $A_\alpha(\mathbf{k}) \approx e^{i\mathbf{a}(\mathbf{k})\cdot\mathbf{g}_\alpha}$, where $\mathbf{a}(\mathbf{k}) = -i\langle u_{\mathbf{k}}|\nabla_{\mathbf{k}}|u_{\mathbf{k}}\rangle$ is the Berry connection, with $|u_{\mathbf{k}}\rangle$ being the periodic part of the Bloch state. The Coulomb gauge condition on $\mathbf{a}(\mathbf{k})$ is $\nabla_{\mathbf{k}}\cdot\mathbf{a}(\mathbf{k}) = 0$. This enables one to write the connection in terms of a stream function $\phi(\mathbf{k})$, $\mathbf{a}(\mathbf{k}) = \hat{e}_z \times \nabla_{\mathbf{k}}\phi(\mathbf{k})$. Since $\nabla_{\mathbf{k}} \times \mathbf{a}(\mathbf{k}) = F(\mathbf{k})\hat{e}_z$, $\phi(\mathbf{k})$ satisfies a Poisson equation $\nabla^2_{\mathbf{k}}\phi(\mathbf{k}) = F(\mathbf{k})$, where $F(\mathbf{k})$ is the Berry curvature with the usual normalization $\int \mathrm{d}^2\mathbf{k} F(\mathbf{k}) = 2\pi C$.

We impose the same Coulomb gauge condition on the lattice connections, and handle separately the average and the fluctuations of the lattice BZ curvature:

$$A_\alpha^{\text{target}}(\mathbf{k}) = A_\alpha^{\text{L}}(\mathbf{k}+\boldsymbol{\gamma}) \exp\left(-i2\pi\varepsilon_{\alpha\beta}[\mathrm{d}_\beta\phi]_{\mathbf{k}}\right). \tag{5.37}$$

The non-zero curvature average necessitates the first factor above. The shift $\boldsymbol{\gamma} = \sum_\alpha \gamma_\alpha \mathbf{g}_\alpha$ is determined by $W_x^{\text{lat}} = W_x^{\text{L}}(\gamma_y)$ and $W_y^{\text{lat}} = W_y^{\text{L}}(\gamma_x)$ ('lat' represents lattice), and it accounts for the mismatch in the large Wilson loops between the two systems. The curvature fluctuations are attended by the exponential factor, where the stream function $\phi_{\mathbf{k}}$ satisfies the discrete Poisson equation $[\widetilde{\Delta}\phi]_{\mathbf{k}} = f_{\mathbf{k}} - 1/N_\phi$, with boundary conditions $[\mathrm{d}_\alpha\phi]_{\mathbf{k}} = [\mathrm{d}_\alpha\phi]_{\mathbf{k}-N_\beta\mathbf{g}_\beta}$ (no summation implied) and $\sum_\kappa^{N_x}[\mathrm{d}_y\phi]_{\kappa\mathbf{g}_x} = \sum_\kappa^{N_y}[\mathrm{d}_x\phi]_{\kappa\mathbf{g}_y} = 0$. In plain words, we require that the connection corrections accounting for the curvature fluctuations should be periodic over the lattice BZ,[8] and they should not contribute to the large Wilson loops W_α^{lat} which have already been fixed by the $A_\alpha^{\text{L}}(\mathbf{k}+\boldsymbol{\gamma})$ factor.

Up to an inconsequential $\mathbf{k}$-independent constant, these conditions allow a *unique* solution

$$\phi_{\mathbf{k}} = \varphi_{\mathbf{k}} + v_y k_x - v_x k_y, \tag{5.38}$$

with $v_\alpha = \frac{1}{N_\alpha}\sum_{\kappa=0}^{N_\alpha-1}\sum_\beta \varepsilon_{\alpha\beta}[\mathrm{d}_\beta\varphi]_{\kappa\mathbf{g}_\alpha}$, and

$$\varphi_{\mathbf{k}} = \frac{1}{N_xN_y}\sum_{\mathbf{n}\neq 0}\frac{e^{i2\pi(k_xn_x/N_x+k_yn_y/N_y)}}{2\cos(2\pi n_x/N_x)+2\cos(2\pi n_y/N_y)-4} \sum_{\mathbf{p}}^{\text{BZ}} e^{-i2\pi(p_xn_x/N_x+p_yn_y/N_y)}\left(f_{\mathbf{p}}-\frac{1}{N_\phi}\right), \tag{5.39}$$

where $\mathbf{n}\equiv(n_x,n_y)$ runs over $\{[0\,..\,N_x)\times[0\,..\,N_y)\}\backslash(0,0)$.

The connections $A_\alpha^{\text{target}}(\mathbf{k})$ in Eq. (5.37) are consistent with the actual (fluctuating) curvature over the lattice BZ. Starting from a set of single-particle Bloch states $|\mathbf{k}\rangle$ with an arbitrarily chosen gauge and connections $A_\alpha(\mathbf{k})$, our gauge fixing scheme

[8] The obstruction to simultaneous smoothness and periodicity is manifested in the non-fluctuating part $A_\alpha^{\text{L}}(\mathbf{k}+\boldsymbol{\gamma})$.

amounts to the gauge transform $|\mathbf{k}\rangle \to e^{i\zeta_{\mathbf{k}}}|\mathbf{k}\rangle$ that reproduces $A_\alpha^{\text{target}}(\mathbf{k})$,

$$e^{i\zeta_{\mathbf{k}}} = \left[\prod_{\kappa=0}^{k_y-1} R_y(0,\kappa)\right]\left[\prod_{\kappa=0}^{k_x-1} R_x(\kappa,k_y)\right], \tag{5.40}$$

with $R_\alpha(\mathbf{k}) = A_\alpha^{\text{target}}(\mathbf{k})/A_\alpha(\mathbf{k})$.

Despite the formal similarity of $e^{i\zeta_k}$ expressed as a product of ratios of connections, the gauge choice here is fundamentally different from the "parallel-transport" gauge used in the last chapter. The generalized Coulomb gauge here provides a better treatment of the curvature *fluctuations*, embodied in the carefully constructed $A_\alpha^{\text{lat}}(\mathbf{k})$. Further, this new gauge fixing scheme preserves the full lattice symmetry of the Chern band.

5.2.4 Twisted torus

The above results can be directly generalized to a twisted torus. Instead of the rectangular torus spanned by $\mathbf{L}_x = L_x\hat{x}$ and $\mathbf{L}_y = L_y\hat{y}$, we consider a torus with twist angle θ, spanned by

$$\mathbf{L}_x = L_x \sin\theta\, \hat{x} + L_x \cos\theta\, \hat{y}, \quad \mathbf{L}_y = L_y\hat{y}. \tag{5.41}$$

The number of fluxes N_ϕ is now defined by

$$L_x L_y \sin\theta = 2\pi l_B^2 N_\phi. \tag{5.42}$$

The reciprocal lattice primitive vectors $\mathbf{g}_\alpha$ are now defined by

$$\mathbf{g}_\alpha \cdot \mathbf{L}_\beta = 2\pi\delta_{\alpha\beta}, \tag{5.43}$$

and we have the wave vector $\mathbf{k} = k_x\mathbf{g}_x + k_y\mathbf{g}_y$, $(k_x, k_y) \in \mathbb{Z}^2$. Once we change the wave functions of the hybrid Wannier states in Landau gauge $\mathbf{A} = Bx\hat{y}$ to

$$\langle x, y, \sigma | X, k_y \rangle = \frac{1}{(\sqrt{\pi} L_y l_B)^{1/2}} \sum_{m}^{\mathbb{Z}} \delta^{\mathrm{mod}\, C}_{\sigma, X+mN_x} e^{-x^2/(2l_B^2)} \exp\left[2\pi \left(\frac{XN_y + k_y C}{C} + mN_\phi \right) \frac{x+iy}{L_y} - i\pi \frac{L_x e^{-i\theta}}{N_\phi L_y} \left(\frac{XN_y + k_y C}{C} + mN_\phi \right)^2 \right],$$

all of the earlier results still hold with no essential modifications. In particular, the proof in Appendix 5.B can be adapted straight-forwardly (albeit with even more tedious algebra), and in Eq. (5.24) the density operator requires no formal change except for $\mathbf{q} = q_x\mathbf{g}_x + q_y\mathbf{g}_y$. For the rest of this chapter, we return to the rectangular torus. The results can be similarly generalized to the twisted torus by simple substitutions.

5.3 Bloch model wave functions

With the one-body Bloch and hybrid Wannier bases at hand, we move to the many-body interacting problem.

As demonstrated in the last section, the multicomponent LLL resembles the Chern band once we impose appropriate boundary conditions that join together the C components. This link enables us to take advantage of the well-developed pseudopotential formalism in the LLL. We construct pseudopotential Hamiltonians (in the same way as those of single-component LLL [38, 82]) in the LLL from the projected density operator $\rho_{\mathbf{q}}$, and obtain its zero modes through numerical diagonalization. Following the usual practice in the FQH literature,[9] we define these zero modes as the FCI model wave functions. Then, through the mapping between the Bloch states in the LLL and on the lattice, we transcribe these LLL wave functions to the lattice. The

[9]For example, the Laughlin states at $\nu = 1/3$ on a torus can be defined as the exact zero modes of the LLL-projected hollow-core interaction.

resulting trial wave functions can be directly compared with the FCI ground states obtained numerically for lattice Hamiltonians.

For FCI with $C > 1$, previous studies suggested that the equivalent FQH states are the SU(C) color-singlet Halperin states [7, 55, 84, 56]. They are the exact zero modes of the color-neutral LLL-projected Hamiltonian $H_{\rm FQH} = \sum_{\mathbf{q}} V_{\mathbf{q}} \rho_{\mathbf{q}} \rho_{-\mathbf{q}}$, where $\mathbf{q}$ is summed over the infinite lattice reciprocal to $(\mathbf{L}_x, \mathbf{L}_y)$ and the interaction between color-neutral densities $\rho_{\mathbf{q}} = \sum_\sigma \rho_{\mathbf{q}\sigma}$ is $V_{\mathbf{q}} = V_0$ for bosons and $V_{\mathbf{q}} = V_0 + (1 - \mathbf{q}^2 l_B^2) V_1$ for fermions, with pseudopotential $V_n > 0$[10]. For the FQH effect in 2D electron gas, the boundary conditions $T(\mathbf{L}_\alpha) = 1$ are imposed separately on different color components. In the LLL description of a FCI, however, we require the system to be periodic under the color-entangled translations $\widetilde{T}_\alpha^{N_\alpha}$. This breaks the SU($C$) symmetry. To compare with the Halperin SU(C)-singlet states, we examine the commensurate case $N_x/C \in \mathbb{Z}$. The boundary conditions in Eq. (5.11) thread $\Phi_\sigma = \sigma N_y/C$ (color-dependent) magnetic fluxes along the y direction into the σ component of the LLL[11]. In the one-dimensional localized basis for the LLL, this shifts the Landau orbitals of color σ by $\Phi_\sigma \mathbf{L}_x / N_\phi$ in real space. Hence we propose that the Wannier mapping [7] be modified to identify the hybrid Wannier states with our shifted LLL orbitals. In the generic, noncommensurate case, the translation $T(\mathbf{L}_x)$ changes the color of the particle, due to $T(\mathbf{L}_x) P^{N_x} = 1$. Our construction thus provides a finite-size realization of the "wormhole" connecting different color components [7].

We demonstrate the Bloch construction using the ruby lattice model ($C = 1$) [45] and the two-orbital triangular lattice model ($C = 3$) [104]. We construct the FCI model states through Eq. (5.33) from the exact-diagonalization ground states of $H_{\rm FQH}$ with color-entangled boundaries. We find high overlaps [Fig. 5.1(a)] and an identical low-lying structure in the entanglement spectrum with the FCI ground states [99,

[10] We focus only on the color-singlet states as observed in numerics [84].

[11] We have verified by numerical diagonalization that the eigenstates of $H_{\rm FQH}$ with color-entangled boundary conditions indeed coincide with the usual Halperin states with Φ_σ flux insertion, when $N_x/C \in \mathbb{Z}$.

84]. The 12-fermion Laughlin state on the ruby lattice model has a Hilbert space of dimension 3.4×10^7. This state is well captured by the model wave function obtained from our construction (overlap ≈ 0.99). The triangular lattice model has decent overlaps, albeit lower than the ruby lattice model. The model we propose has the particle-hole symmetry, which is generally absent in the FCI models [51, 36]. When the lattice model exhibits such an emergent symmetry, our construction can also capture it.

To further examine our construction for $C > 1$, we study the interpolation Hamiltonian $H_\lambda = (1-\lambda)H_{\mathrm{FCI}} + \lambda H_{\mathrm{FQH}}$, $0 \le \lambda \le 1$ [77, 54]. For bosonic on-site density-density interaction on the triangular lattice $H_{\mathrm{FCI}} = U \sum_{ab} \sum_{\{\mathbf{k}_{1-3}\}} \widetilde{\psi}^\dagger_{\mathbf{k}_1 a} \widetilde{\psi}^\dagger_{\mathbf{k}_2 b} \widetilde{\psi}_{\mathbf{k}_3 b} \widetilde{\psi}_{\mathbf{k}_4 a}$, where $\mathbf{k}_4 = \mathbf{k}_1 + \mathbf{k}_2 - \mathbf{k}_3 \pmod{N_\alpha \mathbf{g}_\alpha}$, and $\widetilde{\psi}^\dagger_{\mathbf{k}b} = e^{i\zeta_{\mathbf{k}}} u^*_b(\mathbf{k}) \psi^\dagger_{\mathbf{k}}$ is gauge fixed by $e^{i\zeta_{\mathbf{k}}}$, with $|\mathbf{k}\rangle = \psi^\dagger_{\mathbf{k}}|\emptyset\rangle$. For H_{FQH}, we use color-entanglement boundary conditions $\boldsymbol{\gamma}$. We find that the FCI model states are adiabatically connected to the actual ground states: H_λ remains gapped for $\lambda \in [0,1]$ and its ground states retain the characters of the FCI model states as seen in both overlaps and the particle entanglement spectrum [Fig. 5.1(b)-(d)]. As observed in [84], the six-boson state on 6×4 lattice has clear deviations from the usual Halperin state in the entanglement spectrum. Our FCI model state exactly reproduces these novel features. Note that the 8×4 lattice is closer to the thin-torus limit [14], resulting in smaller overlaps and $\Delta\xi$ values.

5.4 Pseudopotential Hamiltonian

As demonstrated in the previous section, the Bloch construction yields model Hamiltonians adiabatically connected to the microscopic lattice Hamiltonian, and leads to trial wave functions with the correct total momentum on lattice and very high overlaps with the actual FCI ground states. Our trial wave functions also reproduce the anomalous particle entanglement spectrum as observed in Ref. [84]. The

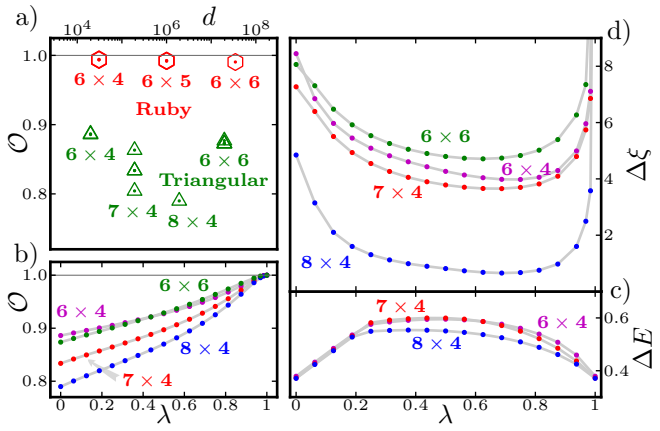

Figure 5.1: (a) shows the overlaps $\mathcal{O}$ between our FCI model states and the ground states of the fermionic ruby and the bosonic triangular lattice models, as a function of the Hilbert space dimension d. (b)-(d) demonstrate the adiabatic continuity between the triangular lattice model and the color-entangled Halperin pseudopotential Hamiltonian on 6×4, 7×4, 8×4, and 6×6 lattices ($\nu = 1/4$ filling). We set $U = 7.4237$, 7.0003, 6.9677, and 5.0955, respectively, to equalize the energy gaps at $\lambda = 0, 1$. (b) shows the overlaps $\mathcal{O}$ between our FCI model states and the ground states of the interpolation Hamiltonian H_λ. (c) shows the energy gap ΔE above the ground states of H_λ. (d) shows the entanglement gap $\Delta\xi$ of the ground states of H_λ. $\Delta\xi$ is defined as the gap between the low-lying structure identical to the full entanglement spectrum of the model states (at $\lambda = 1$) and the higher levels. By this definition, $\Delta\xi$ is infinity at $\lambda = 1$.

question remains, however, how to predict the total lattice momentum for the trial wave functions (including quasiholes) *without* numerical diagonalization, similar to the methods developed for the FQH [12, 13]. For $C = 1$, this problem was solved in Ref. [16] by combining the generalized Pauli principle [12, 13] for single-component FQH states (including quasiholes) with lattice folding. For $C > 1$, we now have the LLL-to-lattice mapping. What we still lack is a multicomponent version of the generalized Pauli principle. Refs. [28, 2] studied this problem for the usual boundary conditions. Due to our modifications to the boundary conditions, their results do not directly apply here.

Fortunately, we can also extract the generalized Pauli principle from the Hamiltonian in the thin-torus limit [89, 11, 79]. In this limit, the hybrid Wannier orbitals in the LLL become isolated from each other. Specifically, we find from Eq. (5.14) that

the ratio between the width of the hybrid Wannier orbital and the spacing between them scales as

$$\frac{\text{width}}{\text{spacing}} \sim \frac{l_B}{2\pi l_B^2/L_y} \sim \sqrt{N_\phi \frac{L_y}{L_x}}. \tag{5.44}$$

Therefore, when the aspect ratio L_x/L_y satisfies

$$\frac{L_x}{L_y} \gg N_\phi, \tag{5.45}$$

the hybrid Wannier orbitals are so separated that the projected density operator becomes approximately diagonal in the hybrid Wannier basis. As a result, the pseudopotential Hamiltonian built from projected density operators also becomes approximately diagonal in the hybrid Wannier basis. (This is not true for certain non-unitary states [67].) By analyzing the classical electrostatics of the leading terms in the Hamiltonian, we can obtain the quantum numbers of the Hamiltonian zero modes. (For FQH with the usual boundary conditions, this was done in Refs. [11, 9, 10].) After the Bloch mapping between FCI and FQH, this will give us a counting rule for the degeneracy of the FCI quasiholes in each lattice momentum sector.

In the rest of this section, we expand the new pseudopotential Hamiltonian proposed earlier [101] in the Wannier basis, and perform the necessary resummation to make it amenable to proper truncation in the thin-torus limit [102]. The actual truncation and the analysis of the zero modes of the truncated Hamiltonian is left for the next section.

5.4.1 Projected density in the hybrid Wannier basis

We obtain the projected density operator in the hybrid Wannier basis by plugging the Fourier transform Eq. (5.17) into Eq. (5.24),

$$\rho_{\mathbf{q}} = e^{-\mathbf{q}^2 l_B^2/4} \sum_{X}^{N_x} \sum_{k_y}^{N_y} e^{-i2\pi q_x[(XN_y + k_y C)/C + q_y/2]/N_\phi} |X, k_y\rangle\langle X, k_y + q_y|. \tag{5.46}$$

Notice that the phase factor depends on the summation variables X, k_y only through the linear combination $XN_y + k_yC$, which is proportional to the center position of the hybrid Wannier orbital $|X, k_y\rangle$ [Eq. (5.14)],

$$\langle X, k_y|\hat{x}|X, k_y\rangle = L_x \frac{XN_y + k_yC}{N_xN_y} \bmod L_x, \tag{5.47}$$

where $\hat{x}$ is the position operator in the x direction. This motivates us to index these orbitals by their center position. In the following, we introduce an alternative labeling $|j, s\rangle$ for the Wannier states. The j index gives the center position of the Wannier state while the s index plays a role similar (but not identical) to the color index σ. As we will see in the next section, the projected interaction decays exponentially when the difference in the j indices between two particles increases.

As seen from Eq. (5.14), the hybrid Wannier state $|X, k_y\rangle$ depends on (X, k_y) only through $XN_y + k_yC$ and $X \bmod C$, in the exponential and the Kronecker-δ in Eq. (5.14), respectively. For integers X, k_y, the linear combination $XN_y + k_yC$ must be an integer multiple of the greatest common divisor (GCD)

$$\widetilde{C} \equiv \mathrm{GCD}(C, N_y). \tag{5.48}$$

Therefore, we introduce two integer labels

$$j = (XN_y + k_yC)/\widetilde{C}, \quad s = X \bmod C. \tag{5.49}$$

For future convenience, we also define integers

$$M = N_xN_y/\widetilde{C}, \quad d = C/\widetilde{C}, \tag{5.50}$$

We emphasize that j and s are not independent. This can be seen by examining the solutions to the first equation in Eq. (5.49). For a given j, if (X, k_y) is a solution, then all the solutions can be parametrized as $(X + nC/\widetilde{C}, k_y - nN_y/\widetilde{C})$, $n \in \mathbb{Z}$. Therefore $s = X \bmod C$ can take $\widetilde{C}$ different values in $[0 \,..\, C)$ with uniform spacing $d = C/\widetilde{C}$ [Eq. (5.50)], corresponding to $n = 1, \ldots, \widetilde{C}$ in $X + nC/\widetilde{C}$. For a given j, we

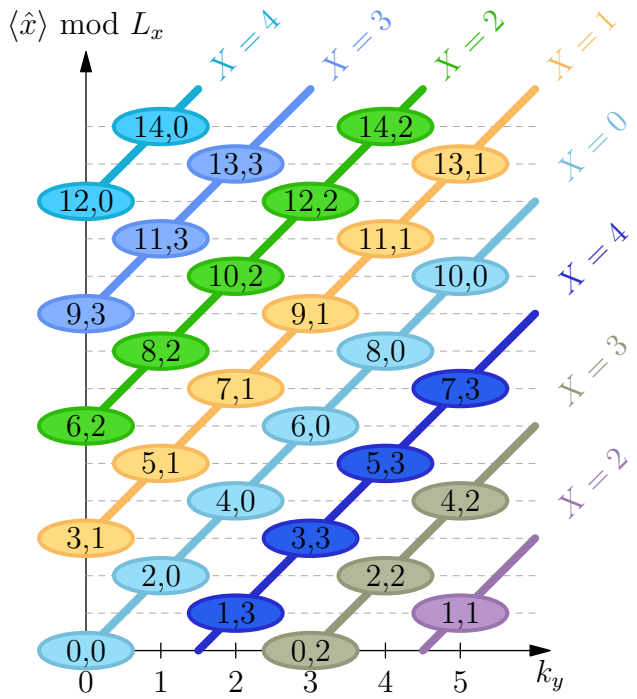

Figure 5.2: Relabeling of the Wannier states $|X, k_y\rangle \leftrightarrow |j, s\rangle$ for $(N_x, N_y) = (5, 6)$ and $C = 4$. We focus on the principal region with $X \in [0 \,..\, N_x)$ and $k_y \in [0 \,..\, N_y)$. Each solid ellipse represents a Wannier center. The horizontal axis gives the k_y index while the vertical axis gives the position of the Wannier center in the x direction (mod L_x). The ellipses are colored according to the X index, and labeled by the (j, s) indices. We have employed Eq. (5.58) to shift j to $[0 \,..\, M)$ and s to $[0 \,..\, C)$. Upon a color-independent flux insertion, each Wannier center flows along the solid lines of its color.

denote this set of $\widetilde{C}$ allowed values of s by

$$S_j \subset [0 \,..\, C). \tag{5.51}$$

A useful property is

$$S_j = S_{j+d}, \tag{5.52}$$

which follows from the fact that $j \to j + d$ can be achieved by $k_y \to k_y + 1$ without touching X. Plugging Eq. (5.49) into Eq. (5.14), we find that indeed we can relabel the hybrid Wannier states

$$|X, k_y\rangle \leftrightarrow |j, s\rangle, \tag{5.53}$$

modulo the identification

$$|j, s\rangle = |j, s + C\rangle. \tag{5.54}$$

An example is given in Fig. 5.2. It is not hard to see that this mapping is bijective, although we cannot easily write down an explicit formula for the solution (X, k_y) to Eq. (5.49) at a given (j, s). We denote the k_y solution formally as

$$k_y(j, s). \tag{5.55}$$

Then, the representation of the color-entangled magnetic translations $\widetilde{T}_\alpha$ in the $|j, s\rangle$ basis can be constructed indirectly from Eq. (5.16),

$$\widetilde{T}_x|j, s\rangle = |j + N_y/\widetilde{C}, s + 1\rangle, \quad \widetilde{T}_y|j, s\rangle = e^{-i2\pi k_y(j,s)/N_y}|j, s\rangle. \tag{5.56}$$

The wave functions for $|j, s\rangle$ can be obtained from Eq. (5.14),

$$\langle x, y, \sigma|j, s\rangle = \frac{1}{(\sqrt{\pi}L_y l_B)^{1/2}} \sum_m^{\mathbb{Z}} \delta_{\sigma, s+mN_x}^{\text{mod } C} \exp\left\{ i2\pi\left(\tfrac{j}{d} + mN_\phi\right) \tfrac{y}{L_y} - \tfrac{1}{2}\left[\tfrac{x}{l_B} - \tfrac{2\pi l_B}{L_y}\left(\tfrac{j}{d} + mN_\phi\right)\right]^2 \right\}. \tag{5.57}$$

In parallel to Eq. (5.15), $|j, s\rangle$ is periodic in s but quasi-periodic in j,

$$|j + M, s + N_x\rangle = |j, s\rangle, \quad |j, s + C\rangle = |j, s\rangle. \tag{5.58}$$

As we will see soon, this twist in s when shifting j is the main issue that sets the current problem apart from the usual multicomponent FQH [28].

We now want to expand the projected density operator in the relabeled hybrid Wannier basis. On the one hand, notice that due to the quasi-periodicity of $|X, k_y\rangle$ [Eq. (5.15)], the double sum of (X, k_y) over $[0 \,..\, N_x) \times [0 \,..\, N_y)$ in Eq. (5.46) can be shifted to any set of $N_x N_y$ points in the $\mathbb{Z}^2$ plane, as long as the corresponding hybrid states are independent from each other. On the other hand, notice that

$$\left\{ |j, s\rangle \,\middle|\, j \in [j_0 \,..\, j_0 + M), s \in S_j \right\} \tag{5.59}$$

label a set of $N_x N_y$ hybrid Wannier states that are independent from each other for any given $j_0 \in \mathbb{Z}$. Therefore, we can rewrite the double sum in Eq. (5.46) as a sum over the above set. Since increasing k_y by q_y while keeping X constant sends (j, s) to $(j + q_y d, s)$, we have

$$\rho_{\mathbf{q}} = e^{-\mathbf{q}^2 l_B^2/4} \sum_{j}^{M}{}' e^{-i2\pi q_x (j + \frac{q_y d}{2})/M} \sum_{s}^{S_j} |j, s\rangle\langle j + q_y d, s|, \tag{5.60}$$

where the primed sum is over $j \in [j_0 \,..\, j_0 + M)$ for an arbitrary $j_0 \in \mathbb{Z}$, with $M = N_x N_y / \widetilde{C}$ [Eq. (5.50)]. The appearance of $\langle j + q_y d, s|$ requires special attention: when we shift $j + q_y d$ back to $[j_0 \,..\, j_0 + M)$ using Eq. (5.58), the s index must be changed accordingly, by $N_x \pmod{C}$. This boundary effect dictates that $\rho_{\mathbf{q}}$ is *not* diagonal in s unless N_x is divisible by C, which discourages a seemingly plausible interpretation of s as an effective spin index in general.

5.4.2 Interacting Hamiltonian

We consider only interactions between a pair of color-neutral densities $\rho_{\mathbf{q}}$. Such interactions can be specified in terms of the Haldane pseudopotentials. Higher-body pseudopotentials[82] can be implemented in the same spirit. We consider only the first two pseudopotentials (V_0, V_1) being non-negative, with all $V_{m>1} = 0$. The interaction strength at momentum transfer $\mathbf{q}$ then reads

$$V_{\mathbf{q}} = 4\pi l_B^2 [V_0 + V_1 \cdot (1 - \mathbf{q}^2 l_B^2)], \tag{5.61}$$

and the Hamiltonian is given by

$$H = \frac{1}{2L_x L_y} \sum_{\mathbf{q}} V_{\mathbf{q}} \rho_{\mathbf{q}} \rho_{-\mathbf{q}}. \tag{5.62}$$

Here $\mathbf{q}$ is summed over the infinite reciprocal lattice.

As discussed earlier, the color-entangled generalizations of the bosonic/fermionic Halperin singlet states and the corresponding quasihole states are defined as the exact

zero modes of the above Hamiltonian (using $V_1 = 0$ for the bosonic case). These states are distinct from the usual Halperin states due to the color-entangled boundary conditions inherent in $\rho_{\mathbf{q}}$. Through numerical diagonalization, we can obtain these zero modes, and then transcribe them to the lattice system of an arbitrary Chern insulator using the one-body mapping between the LLL Bloch states and the lattice Bloch states. We now attempt to achieve an analytic understanding of this Hamiltonian, by exploiting its assumed adiabatic connectivity [101] to the thin-torus limit.

We first plug Eq. (5.60) into Eq. (5.62) and write H in the relabeled hybrid Wannier basis,

$$H = \frac{1}{2L_xL_y}\sum_{\mathbf{q}} e^{-\mathbf{q}^2 l_B^2/2} V_{\mathbf{q}} \sum_{j_1}^{M}{}' \sum_{j_2}^{M}{}' e^{-i2\pi q_x(j_1-j_2+q_yd)/M} \sum_{s_1}^{S_{j_1}} \sum_{s_2}^{S_{j_2}} \psi^\dagger_{j_1,s_1}\psi^\dagger_{j_2,s_2}\psi_{j_2-q_yd,s_2}\psi_{j_1+q_yd,s_1}, \quad (5.63)$$

where M and d are defined in Eq. (5.50), and for $\mathbf{q} = (2\pi q_x/L_x, 2\pi q_y/L_y)$, we have

$$\mathbf{q}^2 l_B^2 = \frac{2\pi}{N_\phi}\left(\frac{L_y}{L_x}q_x^2 + \frac{L_x}{L_y}q_y^2\right). \quad (5.64)$$

We want to massage the above expansion of H to a form amenable to justified truncation in the thin-torus limit. The main obstacle is obviously the oscillatory factor $e^{-i2\pi q_x(j_1-j_2+q_yd)/M}$ in the coefficient. This can be removed in exchange for a Gaussian factor by performing a Poisson resummation over q_x, which does not appear in the index of the creation/annihilation operators. After some straightforward but tedious algebra in Appendix 5.C, we find

$$H = \sqrt{\frac{L_x}{N_\phi L_y}} \sum_{q_y}^{\mathbb{Z}} e^{-\beta(q_yd)^2} \sum_{j}^{M}{}' \sum_{\Delta} \sum_{n}^{\mathbb{Z}} e^{-\beta(\Delta-q_yd+nM)^2} \left\{V_0 + 2\beta V_1\left[(\Delta - q_yd + nM)^2 - (q_yd)^2\right]\right\} \sum_{s}^{S_j}\sum_{s'}^{S_{j+\Delta}} \psi^\dagger_{j,s}\psi^\dagger_{j+\Delta,s'}\psi_{j+\Delta-q_yd,s'}\psi_{j+q_yd,s}, \quad (5.65)$$

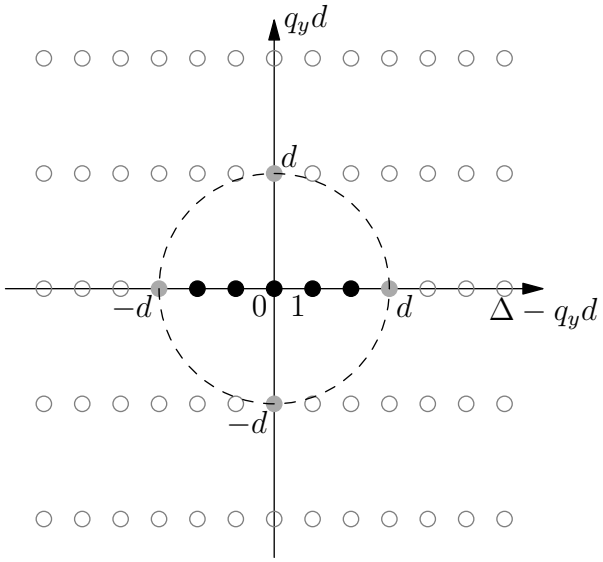

Figure 5.3: Terms in the expansion of the pseudopotential Hamiltonian. Here we illustrate the example of $d = 3$. Each dot represents a term (q_y, Δ) in Eq. (5.67). The weight of each term decays exponentially in its distance from the origin. The dashed circle marks the empirical threshold for truncation $(q_y d)^2 + (\Delta - q_y d)^2 = d^2$. The solid black dots inside are the density-density terms in Eq. (5.70), while the four solid gray dots contain the pair hopping and the density-density terms in Eqs. (5.73) and (5.83).

where Δ is summed over an interval of length M centered around $q_y d$,

$$\Delta \in \big[\, q_y d - \lfloor M/2 \rfloor \,..\, q_y d - \lfloor M/2 \rfloor + M \,\big), \tag{5.66}$$

and we have defined the shorthand $\beta = \dfrac{1}{d^2} \dfrac{\pi}{N_\phi} \dfrac{L_x}{L_y}$.

5.5 Thin-torus analysis

In Eq. (5.65), the Hamiltonian has been organized into groups of density-density or pair hopping terms. The strengths of the terms decay exponentially in the limit $\beta \gg 1$. This is exactly the thin-torus limit in Eq. (5.45). In the following, we perform a proper truncation of the Hamiltonian in this limit and analyze the degeneracy and quantum numbers of its zero modes.

The thin-torus analysis is a well-known, powerful technique to tackle the strongly-correlated physics in single-component FQH effect [11, 9, 10, 14]. In the thin-torus limit, the pair hopping terms die off quickly, and the Hamiltonian becomes classical, dominated by density-density terms and thus solvable. (This is not true for certain non-unitary states [67].) One can obtain the correct degeneracy of the ground states and extract their total momenta simply by minimizing the classical electrostatic energy and completely ignoring the pair hoppings. By assumed adiabatic connectivity, [101] the results must also apply to the isotropic limit. The thin-torus analysis thus provides an intuitive picture for the 'root partitions' and the underlying generalized Pauli principle of Refs. [12, 13]. Our multicomponent pseudopotential Hamiltonian with color-entangled boundaries (5.65) turns out to be considerably more complicated, due to the essential role played by the pair hopping terms. As we will see soon, the largest pair hopping terms have strengths comparable to the subleading density-density terms. Keeping only the leading density-density terms results in too many zero modes compared with the numerical studies [84, 55, 101]. The correct ground-state degeneracy is recovered only after we put back the largest pair hoppings, which turn out to be of similar strength as some of the density-density terms. This indicates that the thin-torus limit of our multicomponent pseudopotential Hamiltonian cannot be described by classical electrostatics alone. The useful result of this section is a set of rules [Sec. 5.5.4] that correctly predict the degeneracy and total lattice momenta of FCI ground states (including quasiholes). This is illustrated by explicit examples in Secs. 5.5.5 and 5.5.6.

5.5.1 Truncation of Bosonic Hamiltonian

Numerical studies in Refs. [84, 55] found gapped FCI phases of bosons at filling $\nu = 1/(C+1)$ with $(C+1)$-fold degenerate ground states, stabilized by on-site interactions projected to a topological flat band with Chern number C. In the following we

specialize to the simplest case of bosons and try to understand the ground states of the pseudopotential Hamiltonian at filling $\nu = 1/(C+1)$ and with quasiholes. Setting $V_0 = \sqrt{N_\phi L_y / L_x} > 0$ and $V_1 = 0$, the Hamiltonian in Eq. (5.65) becomes

$$H = \sum_{q_y}^{\mathbb{Z}} \sum_{j}^{M\,\prime} \sum_{\Delta} \sum_{n}^{\mathbb{Z}} e^{-\beta(q_y d)^2 - \beta(\Delta - q_y d + nM)^2} \sum_{s}^{S_j} \sum_{s'}^{S_{j+\Delta}} \psi^\dagger_{j,s} \psi^\dagger_{j+\Delta,s'} \psi_{j+\Delta-q_y d,s'} \psi_{j+q_y d,s}. \quad (5.67)$$

where the primed sum of j is over

$$j \in [j_0 \,..\, j_0 + M) \quad (5.68)$$

for an arbitrary $j_0 \in \mathbb{Z}$ [Eq. (5.59)], while Δ is summed over the interval of length M given in Eq. (5.66).

In the $\beta \gg 1$ limit, we can safely truncate the sum over n to a single term at $n = 0$, if we assume that $M/d = N_\phi \gg 1$. Further, only the terms with $q_y \sim 0$ and $\Delta - q_y d \sim 0$ have a significant contribution, since the coefficients decay exponentially with respect to the (squared) Euclidean distance from $q_y d = \Delta - q_y d = 0$,

$$R^2(q_y, \Delta) \equiv (q_y d)^2 + (\Delta - q_y d)^2, \quad (5.69)$$

as illustrated in Fig. 5.3. The 4-boson $\psi^\dagger\psi^\dagger\psi\psi$ operator can be either density-density interaction or pair hopping. We find that the terms with $q_y = 0$ are all density-density interactions, while the strongest pair hopping terms may appear at $|q_y| = 1$, $\Delta = q_y d$, with Euclidean distance $R^2 = d^2$.

In light of the previous studies [11, 9, 10, 14], we first examine the effect of the terms with $R^2(q_y, \Delta) < d^2$. They can be collected into

$$H_{<d^2} = \sum_{j}^{M} \sum_{\Delta}^{(-d \,..\, d)} e^{-\beta\Delta^2} n_j n_{j+\Delta}, \quad (5.70)$$

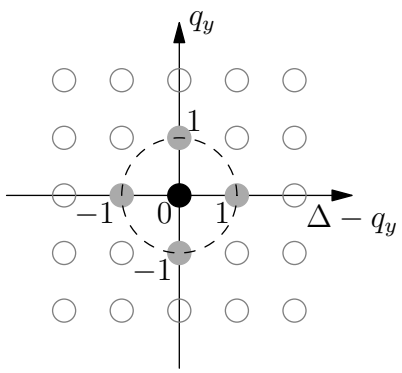

Figure 5.4: Terms in the expansion of the pseudopotential Hamiltonian at $d = 1$. The presentation follows the same format as Fig. 5.3.

where the number operator n_j is defined by

$$n_j = \sum_{s}^{S_j} \psi_{j,s}^{\dagger} \psi_{j,s}. \tag{5.71}$$

Recall from Eq. (5.51) that S_j is the set of all allowed values of s for $\psi_{j,s}$ at a given j, and this set contains $\widetilde{C}$ different values. Also, recall from Eq. (5.50) that $d\,\widetilde{C} = C$. By solving the simple electrostatics, we find that the zero modes of $H_{<d^2}$ with highest density appear at filling $\nu = 1/C$. This leads to much more than $(C+1)$ zero modes at filling $1/(C+1)$, inconsistent with the findings from numerical diagonalization of actual FCI Hamiltonians [84, 55]. This is a clear signal that we should include more terms in the truncated Hamiltonian.

In the following we analyze the effect of the next strongest terms in Eq. (5.67), with Euclidean distance $R^2(q_y, \Delta) = d^2$. They are located at $(|\Delta - q_y d|, |q_y d|) = (0, d)$ and $(d, 0)$, represented by the four solid gray dots in Fig. 5.3. In the next section we provide detailed analysis of the simplest case with $d = 1$. The results for general d will be presented afterwards.

5.5.2 Effect of non-density terms: $d = 1$

In this subsection we specialize to the simplest case $d = 1$, illustrated in Fig. (5.4). In this case N_y is divisible by C [Eqs. (5.48) and (5.50)]. The pseudopotential Hamil-

tonian in Eq. (5.67) (after truncating the sum over n) becomes

$$H = \sum_{q_y}^{\mathbb{Z}} \sum_{j}^{M\,\prime} \sum_{\Delta} e^{-\beta q_y^2 - \beta(\Delta - q_y)^2} \sum_{s}^{S_j} \sum_{s'}^{S_{j+\Delta}} \psi^\dagger_{j,s} \psi^\dagger_{j+\Delta,s'} \psi_{j+\Delta-q_y,s'} \psi_{j+q_y,s}. \tag{5.72}$$

We now extract the terms at $q_y^2 + (\Delta - q_y)^2 = d^2 = 1$, namely, at $(q_y, \Delta) = (1,1), (0,1), (-1,-1), (0,-1)$. To collect together the terms nicely, recall from Eq. (5.52) that $S_j = S_{j+1}$ at $d = 1$, and note that we can take advantage of the freedom in Eq. (5.68) to shift the range of the primed sum over j. We then find

$$\sum_{j}^{M} e^{-\beta} \sum_{s}^{S_j} \sum_{s'}^{S_j} \Big[(1,1) + (0,1) + (-1,-1) + (0,-1) \Big]. \tag{5.73}$$

The four terms in the above brackets are labeled by (q_y, Δ), and explicitly they are given by

$$\begin{aligned} &\psi^\dagger_{j,s} \psi^\dagger_{j+1,s'} \psi_{j,s'} \psi_{j+1,s} + \psi^\dagger_{j,s} \psi^\dagger_{j+1,s'} \psi_{j+1,s'} \psi_{j,s} \\ &+ \psi^\dagger_{j+1,s} \psi^\dagger_{j,s'} \psi_{j+1,s'} \psi_{j,s} + \psi^\dagger_{j+1,s} \psi^\dagger_{j,s'} \psi_{j,s'} \psi_{j+1,s}. \end{aligned} \tag{5.74}$$

The second and the fourth terms above are density-density interactions, while the first and the third exchange the s indices of a pair of particles. We will refer to the latter terms as "s-exchange" terms. Notice that we can combine the above four terms into a single product,

$$b^\dagger_{j,s,s'} b_{j,s,s'}, \tag{5.75}$$

where the pair annihilation operator is given by

$$b_{j,s,s'} = \psi_{j,s'} \psi_{j+1,s} + \psi_{j+1,s'} \psi_{j,s}. \tag{5.76}$$

This combination is the key to the enumeration of zero modes as we detail below. Together with the density-density terms in Eq. (5.70), the bosonic pseudopotential Hamiltonian takes the truncated form

$$H = \sum_{j}^{M} \left[n_j n_j + e^{-\beta} \left(2 n_j n_{j+1} + \sum_{s}^{S_j} \sum_{s'}^{S_j} b^\dagger_{j,s,s'} b_{j,s,s'} \right) \right] + \sum_{j}^{M} \mathcal{O}\left(e^{-2\beta} \right). \tag{5.77}$$

The residual terms are exponentially small for $\beta \gg 1$.

When $\widetilde{C} = 1$, the s index can take only a single value $s = 0$, reducing $b_{j,s,s'}$ to $2\psi_{j,0}\psi_{j+1,0}$. This includes the case of Chern number $C = 1$. The truncated Hamiltonian becomes very simple:

$$H = \sum_{j}^{M} \left(n_j n_j + 4e^{-\beta} n_j n_{j+1} \right) + \sum_{j}^{M} \mathcal{O}\Big(e^{-2\beta}\Big). \tag{5.78}$$

Its zeros modes have no more than one boson in two consecutive orbitals. We thus recover the familiar result [11, 12] for the bosonic Laughlin state at half filling.

We now come back to the case with generic C. We look for the constraints on the zero modes of the above truncated Hamiltonian in Eq. (5.77). Due to the two-body nature of the interaction, we only need to consider a pair of bosons at a time, with j indices being j_1, j_2. In Eq. (5.77), each term in the summation is positive-semidefinite by itself. This means that to find the zero modes of Eq. (5.77), we only need to identify the null space of each term individually, and then take their intersection. From the density-density terms, we find that in a zero mode we must have

$$|j_1 - j_2| \geq 1. \tag{5.79}$$

This amounts to a minimal distance between adjacent bosons along the j axis, with no discrimination of the s indices. The s-exchange terms $\sum b^\dagger b$ in Eq. (5.77) kick in only when the equality sign is taken in Eq. (5.79), as is evident from Eq. (5.76). Specifically, $\sum b^\dagger b$ enforces in a zero mode the antisymmetrization of the s indices between bosons with $|j_1 - j_2| = 1$,

$$\left(\psi^\dagger_{j_1,s_1} \psi^\dagger_{j_2,s_2} - \psi^\dagger_{j_1,s_2} \psi^\dagger_{j_2,s_1} \right) |\emptyset\rangle. \tag{5.80}$$

We emphasize that the $\psi^\dagger$'s are bosonic operators. It is easy to verify that the above antisymmetrized form is indeed annihilated by $\sum b^\dagger b$, whereas the symmetrized form acquires a positive energy $2e^{-\beta}$. To find the zero modes for a system of N bosons, we need to perform the above procedure on each pair of bosons. This is explained in more details in Sec. 5.5.4, and illustrated by an example in Sec. 5.5.6.

One last subtlety comes from the quasi-periodicity of the j index [Eq. (5.58)]. The orbitals at $j+M$ are identified with those at j, but there is a possible mismatch between the s indices,

$$|j+M,s\rangle = |j,s-N_x\rangle. \tag{5.81}$$

For the density terms, this does not make much trouble since $n_j = n_{j+M}$ after the summation of the s index over S_j [Eq. (5.71)]; we just need to enforce the minimal distance condition [Eq. (5.79)] across the quasi-periodic boundary $j = 0 \bmod M$. For the s-exchange terms $\sum b^\dagger b$, however, we have to be more careful about the s index mismatch. We have to first shift their j indices (by integer multiples of M) such that $|j_1 - j_2| = 1$ *before* we can apply the antisymmetrization in Eq. (5.80). More explicitly, if $|j_1 - j_2 + M| = 1$ for example, then the correct antisymmetrization can be either of the following two equivalents,

$$\left(\psi^\dagger_{j_1+M,s_1}\psi^\dagger_{j_2,s_2} - \psi^\dagger_{j_1+M,s_2}\psi^\dagger_{j_2,s_1}\right)|\emptyset\rangle = \left(\psi^\dagger_{j_1,s_1-N_x}\psi^\dagger_{j_2,s_2} - \psi^\dagger_{j_1,s_2-N_x}\psi^\dagger_{j_2,s_1}\right)|\emptyset\rangle, \tag{5.82}$$

but *not* Eq. (5.80) anymore. This is the only reason why we were not able to consistently implement [101] the exclusion principle for conventional multicomponent FQH model states [28, 2] for the color-entangled system.

5.5.3 Effect of non-density terms: general d

The analysis for general d is not much different from $d = 1$. Here we just state the essential results. The s-exchange and density-density terms at $(q_y d)^2 + (\Delta - q_y d)^2 = d^2$ can be merged together,

$$\sum_j^M e^{-\beta d^2} \sum_s^{S_j} \sum_{s'}^{S_j} b^\dagger_{j,s,s'} b_{j,s,s'}, \tag{5.83}$$

where the two-body annihilation operator is given by

$$b_{j,s,s'} = \psi_{j,s'}\psi_{j+d,s} + \psi_{j+d,s'}\psi_{j,s}. \tag{5.84}$$

Combined with the density-density terms in Eq. (5.70), the leading terms in the bosonic pseudopotential Hamiltonian in the limit of $\beta \gg 1$ are

$$H = \sum_{j}^{M} \left[\sum_{\Delta}^{(-d \,..\, d)} e^{-\beta\Delta^2} n_j n_{j+\Delta} + e^{-\beta d^2} \sum_{s}^{S_j} \sum_{s'}^{S_j} b^\dagger_{j,s,s'} b_{j,s,s'} \right], \tag{5.85}$$

up to $\mathcal{O}(e^{-\beta(d^2+1)})$ corrections. The zero modes of the truncated Hamiltonian satisfy the following pairwise constraints. First, for a pair of bosons with j indices being j_1 and j_2, we must have

$$|j_1 - j_2| \geq d. \tag{5.86}$$

Here the difference in j is understood with the quasi-periodic identification $j \sim j+M$. When the equality in Eq. (5.86) holds, the two bosons are further subject to an antisymmetrization in the s indices. For the simplest case $|j_1 - j_2| = d$, we need Eq. (5.80), whereas for $|j_1 - j_2 + M| = d$, we need either of the two equivalents in Eq. (5.82). When $\widetilde{C} = 1$, as s can take only one value, this antisymmetrization consistently reduces to an electrostatic repulsion at distance $|j_1 - j_2| = d$ (and also $|j_1 - j_2 + M| = d$).

5.5.4 Counting rule for degeneracy and momenta

Following the above constraints, we can enumerate all the zero modes of the truncated Hamiltonian for a given system size and a given number of particles, in the form

$$\mathcal{A}\big[\, \psi^\dagger_{j_1,s_1} \psi^\dagger_{j_2,s_2} \psi^\dagger_{j_3,s_3} \psi^\dagger_{j_4,s_4} \cdots \,\big] \, |\emptyset\rangle, \tag{5.87}$$

where $\mathcal{A}$ antisymmetrizes the s indices as follows. As noted earlier, for any pair of particles a and b in a zero mode, we must have $|j_a - j_b| \geq d$, and when the equality holds, we need to carry out antisymmetrization over the s indices (s_a, s_b). Obviously, if we have $j_1 - j_2 = d$ and $j_2 - j_3 = d$, then we need to antisymmetrize over (s_1, s_2, s_3). More generally, if we have a cluster of m consecutive particles satisfying $j_a - j_{a+1} = d$, we need a full antisymmetrization over all the s indices of these m particles.

The last remaining step is to group these zero modes according by the total Bloch momentum and count the degeneracy per momentum sector. The resulting degeneracy is linked by the Bloch mapping [101] to the degeneracy of FCI ground states per lattice momentum sector. This largely follows the same procedure as detailed in Ref. [16]. We represent by lowercase k_α the Bloch momenta of individual particles in the $\alpha = x, y$ direction, and by uppercase

$$K_\alpha = \sum k_\alpha \bmod N_\alpha \tag{5.88}$$

the total Bloch momentum of the many-body system (the summation is over particles). We denote by $\widetilde{T}_\alpha^{\mathrm{cm}}$ the center-of-mass color-entangled magnetic translations, i.e. applying $\widetilde{T}_\alpha$ simultaneously on all the particles. Then, the total Bloch momentum K_α can be read off from the eigenvalue of $\widetilde{T}_\alpha^{\mathrm{cm}}$,

$$\widetilde{T}_\alpha^{\mathrm{cm}} = e^{-i2\pi K_\alpha/N_\alpha}. \tag{5.89}$$

The action of $\widetilde{T}_\alpha^{\mathrm{cm}}$ on the zero modes in Eq. (5.87) is spelled out in Eq. (5.56).

There are four points to make here. *First*, the zero modes in the form of Eq. (5.87) are automatically eigenstates of $\widetilde{T}_y^{\mathrm{cm}}$. Evidently each term in the antisymmetrization $\mathcal{A}$ individually is an eigenstate of $\widetilde{T}_y^{\mathrm{cm}}$. Moreover, the eigenvalues have to be the same for all those terms. This follows from the linearity of Eq. (5.49): to find the total $\sum k_y$ of all particles, we only need to know the total $\sum j$ and $\sum s$; the actual association of between j and s does not matter. *Second*, under the action of $\widetilde{T}_x^{\mathrm{cm}}$, the zero modes in Eq. (5.87) form closed orbits. This follows from the fact that $\widetilde{T}_x^{\mathrm{cm}}$ commutes with the (truncated) pseudopotential Hamiltonian, and thus preserves its null space. More directly, one can easily verify that the constraints on the zero modes described in Secs. 5.5.2 and 5.5.3 are invariant under the action of $\widetilde{T}_x^{\mathrm{cm}}$ (namely $X \to X + 1$, or $|\{j, s\}\rangle \to |\{j+N_y/\widetilde{C}, s+1\}\rangle$), and that the action of $\widetilde{T}_x^{\mathrm{cm}}$ always brings one zero mode in the form of Eq. (5.87) to another zero mode in the same form. *Third*, each action of $\widetilde{T}_x^{\mathrm{cm}}$ along the orbit is associated with a sign, since a term in the antisymmetrization

$\mathcal{A}$ in Eq. (5.87) may be brought to a term with the opposite sign. [12] *Fourth*, all the zero modes in an orbit under $\widetilde{T}_x^{\rm cm}$ share the same eigenvalue under $\widetilde{T}_y^{\rm cm}$. This is a direct consequence of $[\widetilde{T}_x^{\rm cm}, \widetilde{T}_y^{\rm cm}] = 0$.

For each zero mode in the form of Eq. (5.87), we can directly compute the total K_y momentum by just looking at a single term in the antisymmetrization $\mathcal{A}$. We can group together the zero modes by the value of $K_y = \sum k_y \bmod N_y$. Then, within each group, we successively apply $\widetilde{T}_x^{\rm cm}$ on each zero mode and further break them into disjoint orbits. Consider an orbit consisting of n zero modes $|0\rangle, |1\rangle, \ldots, |n-1\rangle$ of the form in Eq. (5.87). They are linked together by

$$\widetilde{T}_x^{\rm cm} |r\rangle = g_r \, |r+1 \bmod n\rangle, \quad r \in [0 \,..\, n), \tag{5.90}$$

with $g_r = \pm 1$ determined from the action of $\widetilde{T}_x^{\rm cm}$ on the antisymmetrization in Eq. (5.87). The n eigenstates of $\widetilde{T}_x^{\rm cm}$ are linear recombinations of these n states in the form of Fourier sums. Without actually writing down the linear recombinations, we can directly obtain the eigenvalues. By successively applying the above equation, we find

$$[\widetilde{T}_x^{\rm cm}]^n \, |r\rangle = g \, |r\rangle, \tag{5.91}$$

with $g = \prod_{r'}^{n} g_{r'}$. This fixes the n eigenvalues of $\widetilde{T}_x^{\rm cm}$ to be the n distinct n-th roots of g. If $g = 1$, the total K_x momenta of the zero modes are

$$K_x = k\frac{N_x}{n} \bmod N_x, \quad k \in [0 \,..\, n), \tag{5.92}$$

whereas if $g = -1$, they are

$$K_x = k\frac{N_x}{n} + \frac{N_x}{2} \bmod N_x, \quad k \in [0 \,..\, n). \tag{5.93}$$

[12] For the case of fermions, there also is a statistical sign, as noted in Ref. [16].

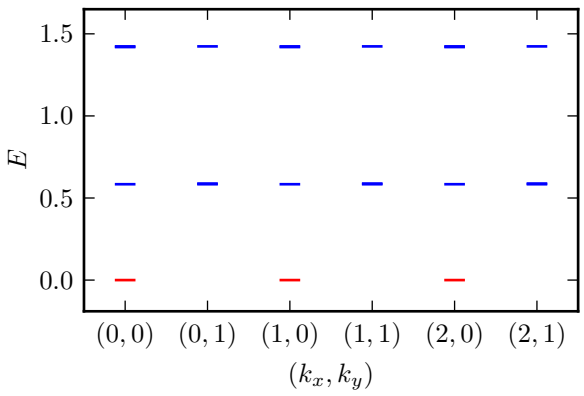

Figure 5.5: Energy spectrum of the pseudopotential Hamiltonian of 2 bosons on a $N_x \times N_y = 3 \times 2$ lattice with Chern number $C = 2$. The three degenerate ground states at zero energy are marked in red.

The numbers on the right hand side of the above equation are guaranteed to be integers: Since $[\widetilde{T}_x^{\mathrm{cm}}]^{N_x}$ is the identity operator per the color-entangled boundary condition [Eq. (5.11)], we must have $N_x/n \in \mathbb{Z}$, and also $g^{N_x/n} = 1$.

Our end goal is an analytic algorithm to obtain the degeneracy of the zero modes in each Bloch momentum sector. This request is more modest than to find the actual expression of the zero modes in each sector, and the above procedure can be further simplified. For example, we do not need to actually write down the zero modes as in Eq. (5.87). We only need to keep track of the structure of clusters of consecutive particles with $j_a - j_{a+1} = d$, as noted below Eq. (5.87), and the set of s indices in each cluster. An open-source reference implementation can be found at `http://fractionalized.github.io`. We have tested our algorithm extensively against the total Bloch momenta of the actual ground states obtained from numerical diagonalization for various system sizes, and found perfect agreement across all cases.

5.5.5 A simple example

To see the above counting rule in action, we consider a simple example, 2 bosons on a $N_x \times N_y = 3 \times 2$ lattice with Chern number $C = 2$. From numerical diagonalization of the pseudopotential Hamiltonian (see Fig. 5.5), we find 3-fold degenerate ground

states with total Bloch momenta

$$(K_x, K_y) = (0,0), (1,0), (2,0) \text{ mod } (3,2). \tag{5.94}$$

We note that the spinless counting rule [16] gives the wrong result $K_y = 1 \text{ mod } 2$ when naively applied to this system. We now show how our new procedure produces the correct momenta.

From $(N_x, N_y) = (3,2)$ and $C = 2$, we compute $\widetilde{C} = \text{GCD}(C, N_y) = 2$, $d = C/\widetilde{C} = 1$, $M = N_x N_y/\widetilde{C} = 3$. Equation (5.49) reduces to

$$j = X + k_y, \quad s = X \text{ mod } 2. \tag{5.95}$$

We denote $s = 0$ by $\downarrow$ and $s = 1$ by $\uparrow$. To facilitate two-way lookup of the mapping $(X, k_y) \leftrightarrow (j, s)$, we can make a table

X	k_y	j	s
0	0	0	$\downarrow$
0	1	1	$\downarrow$
1	0	1	$\uparrow$
1	1	2	$\uparrow$
2	0	2	$\downarrow$
2	1	0	$\uparrow$

(5.96)

The last line in the above table deserves special attention. From Eq. (5.95), for $(X, k_y) = (2,1)$ we obtain $(j, s) = (3, \downarrow)$. However, due to the quasi-periodicity condition in j, [Eq. (5.58)], this is equivalent to $(j, s) = (0, \uparrow)$.

We enumerate all the two-boson zero modes of the truncated pseudopotential Hamiltonian [Eq. (5.85)] in the form of Eq. (5.87). Applying the constraint $|j_1 - j_2| \geq 1$ across the quasi-periodic boundary of j, we find only three possibilities

$$(j_1, j_2) = (0,1), (1,2), (0,2). \tag{5.97}$$

All of them satisfy either $|j_1 - j_2| = d$ (first two) or $|j_1 - j_2 + M| = d$ (last one), and are thus subject to full antisymmetrization of the s indices (s_1, s_2). Since there are only two allowed values of s, we can already see that there are only 3 zero modes in the form

of Eq. (5.87). We now go through them one by one. First, consider $(j_1, j_2) = (0, 1)$. Using Eq. (5.80), we find that the only possible (s_1, s_2) antisymmetrization is

$$|0,1\rangle\rangle \equiv \left(\psi^\dagger_{0,\downarrow}\psi^\dagger_{1,\uparrow} - \psi^\dagger_{0,\uparrow}\psi^\dagger_{1,\downarrow}\right)|\emptyset\rangle. \tag{5.98}$$

Here the double bracket $|\cdot,\cdot\rangle\rangle$ distinguishes the many-body zero mode from the one-body basis state $|j, s\rangle$, and the subscript of the creation operator $\psi^\dagger$ denotes (j, s). Similarly, for $(j_1, j_2) = (1, 2)$, we find

$$|1,2\rangle\rangle \equiv \left(\psi^\dagger_{1,\downarrow}\psi^\dagger_{2,\uparrow} - \psi^\dagger_{1,\uparrow}\psi^\dagger_{2,\downarrow}\right)|\emptyset\rangle. \tag{5.99}$$

The case of $(j_1, j_2) = (0, 2)$ satisfies $|j_1 - j_2 + M| = d$ rather than $|j_1 - j_2| = d$. So we use Eq. (5.82) rather than Eq. (5.80), and find

$$|0,2\rangle\rangle \equiv \left(\psi^\dagger_{3,\downarrow}\psi^\dagger_{2,\uparrow} - \psi^\dagger_{3,\uparrow}\psi^\dagger_{2,\downarrow}\right)|\emptyset\rangle = \left(\psi^\dagger_{0,\uparrow}\psi^\dagger_{2,\uparrow} - \psi^\dagger_{0,\downarrow}\psi^\dagger_{2,\downarrow}\right)|\emptyset\rangle. \tag{5.100}$$

Notice that after we bring the j indices back to $[0 \,..\, M)$ using Eq. (5.81), the s indices on the second line are *not* in an explicit antisymmetrized form. This manifests the core difference of our problem from the usual FQH: When the lattice size is incommensurate with the Chern number, we cannot consistently distinguish the C families of Wannier states, since the flow of Wannier centers are entangled on the quasi-perioidic boundary.

Using the lookup table in Eq. (5.96), we find that the total K_y momenta of the three zero modes are all equal to 0 mod 2, consistent with Eq. (5.94). To compute the K_x momentum, we need to find out the action of the center-of-mass translation $\widetilde{T}_x^{\mathrm{cm}}$ on these states. For our example, Equation (5.56) reduces to

$$\widetilde{T}_x|j, s\rangle = |j + 1, s + 1\rangle. \tag{5.101}$$

We thus find the representation of $\widetilde{T}_x^{\rm cm}$ on the zero modes:

$$\begin{aligned}
\widetilde{T}_x^{\rm cm}|0,1\rangle\!\rangle &= \left(\psi_{1,\uparrow}^\dagger\psi_{2,\downarrow}^\dagger - \psi_{1,\downarrow}^\dagger\psi_{2,\uparrow}^\dagger\right)|\emptyset\rangle = -|1,2\rangle\!\rangle, \\
\widetilde{T}_x^{\rm cm}|1,2\rangle\!\rangle &= \left(\psi_{2,\uparrow}^\dagger\psi_{3,\downarrow}^\dagger - \psi_{2,\downarrow}^\dagger\psi_{3,\uparrow}^\dagger\right)|\emptyset\rangle = |0,2\rangle\!\rangle, \\
\widetilde{T}_x^{\rm cm}|0,2\rangle\!\rangle &= \left(\psi_{1,\downarrow}^\dagger\psi_{3,\downarrow}^\dagger - \psi_{1,\uparrow}^\dagger\psi_{3,\uparrow}^\dagger\right)|\emptyset\rangle \\
&= \left(\psi_{1,\downarrow}^\dagger\psi_{0,\uparrow}^\dagger - \psi_{1,\uparrow}^\dagger\psi_{0,\downarrow}^\dagger\right)|\emptyset\rangle = -|0,1\rangle\!\rangle.
\end{aligned} \tag{5.102}$$

Notice that we can evaluate $\widetilde{T}_x^{\rm cm}|0,2\rangle\!\rangle$ using either line in Eq. (5.100); the results are guaranteed to be the same by the consistency between Eqs. (5.56) and (5.58).

The three zero modes thus form a single orbit under the successive action of $\widetilde{T}_x^{\rm cm}$. They can be recombined to form eigenstates of $\widetilde{T}_x^{\rm cm}$. To find the total K_x momenta of the recombined states, we can either follow the procedure detailed in the last subsection, or we can brute-force diagonalize $\widetilde{T}_x^{\rm cm}$. The representation matrix of $\widetilde{T}_x^{\rm cm}$ over the three zero modes reads

$$\begin{pmatrix} 0 & -1 & 0 \\ 0 & 0 & 1 \\ -1 & 0 & 0 \end{pmatrix}. \tag{5.103}$$

From its eigenvalues $\{1, e^{i2\pi/3}, e^{-i2\pi/3}\}$, we find the total K_x momenta of the three recombined zero modes to be $0, 1, 2 \bmod 3$. In summary, we reproduce the correct total Bloch momenta in Eq. (5.94).

5.5.6 An example with quasiholes

Next, we consider a slightly more complicated example with quasiholes. For a system of 3 bosons with $C = 2$, the densest zero modes of our pseudopotential Hamiltonian occur at filling $\nu = 1/(C+1) = 1/3$, i.e. 3 bosons in 9/2 fluxes. The fractional flux is possible thanks to the color-entangled boundary conditions in Eq. (5.11). We now add $\frac{1}{2}$ flux to each color component and consider $N_x \times N_y = 5 \times 2$ and $N_\phi = 9/2+1/2 = N_xN_y/C = 5$. This leads to a set of 10-fold degenerate quasihole states at

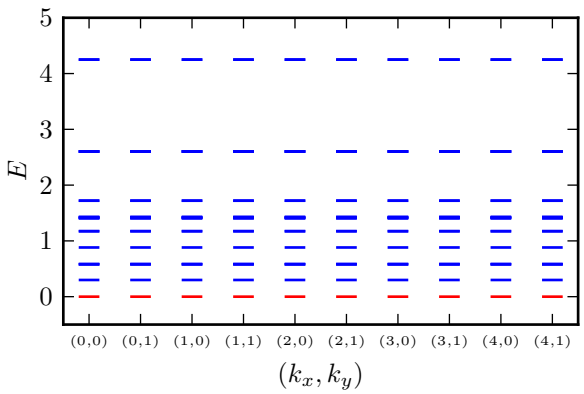

Figure 5.6: Energy spectrum of the pseudopotential Hamiltonian of 3 bosons on a $N_x \times N_y = 5 \times 2$ lattice with Chern number $C = 2$. The 10 degenerate ground states at zero energy are marked in red.

zero energy, with one mode in each momentum sector $(K_x, K_y) \in [0 \,..\, N_x) \times [0 \,..\, N_y)$. This can be seen in the numerical diagonalization results in Fig. 5.6.

We now show how to obtain this counting using our algorithm. The basic procedure is the same as the previous example. We first compute $\widetilde{C} = \mathrm{GCD}(C, N_y) = 2$, $d = C/\widetilde{C} = 1$, and $M = N_x N_y/\widetilde{C} = 5$. Equation (5.49) again reduces to Eq. (5.95), and we have two allowed values of s (0 and 1), denoted by $\downarrow$ and $\uparrow$. Then we can build the $(X, k_y) \leftrightarrow (j, s)$ lookup table,

X	k_y	j	s
0	0	0	$\downarrow$
0	1	1	$\downarrow$
1	0	1	$\uparrow$
1	1	2	$\uparrow$
2	0	2	$\downarrow$
2	1	3	$\downarrow$
3	0	3	$\uparrow$
3	1	4	$\uparrow$
4	0	4	$\downarrow$
4	1	0	$\uparrow$

(5.104)

Again, the last line in the table has a flipped s index due to the quasi-periodic boundary condition in j [Eq. (5.58)].

Compared with the previous example, the enumeration of the zero modes in the form of Eq. (5.87) has an extra complication. Let us first apply the $|j_a - j_b| \geq 1$ rule between each pair of bosons. We find two groups of allowed (j_1, j_2, j_3) configurations,

$$(\underline{0,1,2}), (\underline{1,2,3}), (\underline{2,3,4}), (\underline{3,4,0}), (\underline{4,0,1}), \tag{5.105}$$

and

$$(\underline{0,1},3), (\underline{1,2},4), (\underline{2,3},0), (\underline{3,4},1), (\underline{4,0},2). \tag{5.106}$$

Here we have underlined each cluster of bosons linked together by $|j_a - j_b| = d = 1$ or $|j_a - j_b + M| = d = 1$. Then, we need to antisymmetrize the s indices of the bosons in the same cluster. This kills the five configurations in the first group [Eq. (5.105)]: the three bosons in the same cluster must take different values of s under antisymmetrization, but there are only two possible values of s ($\uparrow$ and $\downarrow$). We are left with the five j configurations in Eq. (5.106). In each configuration, the two clustered bosons have antisymmetrized s indices $\uparrow\downarrow - \downarrow\uparrow$, while the third boson can take either $\uparrow$ or $\downarrow$. For example, for $(j_1, j_2, j_3) = (0, 1, 3)$, we have a pair of zero modes

$$\left(\psi^\dagger_{0,\downarrow}\psi^\dagger_{1,\uparrow} - \psi^\dagger_{0,\uparrow}\psi^\dagger_{1,\downarrow}\right)\psi^\dagger_{3,\uparrow}\left|\emptyset\right\rangle, \quad \left(\psi^\dagger_{0,\downarrow}\psi^\dagger_{1,\uparrow} - \psi^\dagger_{0,\uparrow}\psi^\dagger_{1,\downarrow}\right)\psi^\dagger_{3,\downarrow}\left|\emptyset\right\rangle. \tag{5.107}$$

We can similarly write down the other 8 zero modes. This gives the correct 10-fold degeneracy. Using the lookup table in Eq. (5.104), we can compute the K_y lattice momentum for each zero mode and construct the representation matrix of the color-entangled center-of-mass translation operator $\widetilde{T}^{\mathrm{cm}}_x$ in exactly the same manner as in the previous example. This reproduces the correct degeneracy in each momentum sector. We leave details of this last step for the interested readers.

5.6 Discussion

In this chapter we have studied fractional Chern insulators with an arbitrary Chern number. We establish a one-body mapping between a Chern band with Chern number C, and a C-component LLL with specially engineered boundary conditions. The new boundary conditions lead to an alternative set of pseudopotential Hamiltonians, and the corresponding zero modes define new model wave functions. We introduce a Bloch basis for multicomponent LLL with a rational number of fluxes that entangles real and internal spaces on the one-body level. We establish a Bloch-basis mapping between a Chern band with an arbitrary Chern number C on an arbitrary $N_x \times N_y$ lattice and a C-component LLL with $N_\phi = N_x N_y / C \in \mathbb{Q}$ fluxes. This mapping leads to a novel scheme, which we call Bloch construction, to build FCI model states from color-neutral FQH Hamiltonians. It treats bosonic/fermionic FCI with arbitrary $N_x, N_y, C \in \mathbb{Z}$ in a wholesale fashion, and can handle large system sizes. The new gauge fixing in our basis significantly improves the overlaps with the actual ground states when curvature strongly fluctuates.

We refer to the constructed FCI model states as the color-entangled Halperin states. They are distinct from the SU(C)-singlet Halperin states due to the color-entangled boundary conditions. When the lattice size is commensurate with C, the color-entangled states are the generalization of the usual Halperin states to color-dependent twisted boundaries. More generally, the lattice setup opens up access to the color-entangled, unphysical sectors of a multicomponent FQH system in a physical way.

We have also analyzed the pseudopotential model Hamiltonian for FCI with an arbitrary Chern number. By taking the thin-torus limit and keeping only the leading density-density and pair hopping terms, we are able to analytically solve the pseudopotential Hamiltonian and obtain its zero modes. By analyzing the representation of the center-of-mass translation operators, we derive an algorithm to directly com-

pute the total Bloch momenta of the degenerate zero modes. As we have shown numerically, our pseudopotential Hamiltonian is adiabatically connected to the lattice FCI Hamiltonian, and the its zero modes serve as good trial wave functions for the FCI ground states. In particular, there is a 1-to-1 correspondence between the trial wave function and the FCI ground state in each momentum sector. Therefore, our counting algorithm can be used to obtain the total lattice momenta of the FCI ground states (including quasiholes) without diagonalizing the FCI Hamiltonian, for Abelian FCI states at filling $\nu = 1/(C+1)$.

5.A Hybrid Wannier states under color-entangled magnetic translations

In this Appendix we prove Eq. (5.16), the representation of $\widetilde{T}_x$ and $\widetilde{T}_y$ in the hybrid Wannier basis $|X, k_y\rangle$. In Landau gauge $\mathbf{A} = Bx\hat{y}$, the magnetic translation operators T_x and T_y defined in Eq. (5.6) have the real-space representation

$$T_x = e^{i2\pi \frac{N_\phi}{N_x}\frac{y}{L_y}} e^{-\frac{L_x}{N_x}\partial_x}, \quad T_y = e^{-\frac{L_y}{N_y}\partial_y}. \tag{5.108}$$

Acting on a trial state $|\psi\rangle$, they transform the real-space wave function $\langle x, y|\psi\rangle$ by

$$\langle x, y|T_x|\psi\rangle = e^{i2\pi \frac{N_\phi}{N_x}\frac{y}{L_y}} \langle x - L_x/N_x, y|\psi\rangle, \quad \langle x, y|T_y|\psi\rangle = \langle x, y - L_y/N_y|\psi\rangle. \tag{5.109}$$

Plugging these into the Landau-gauge definition of $|X, k_y\rangle$ in Eq. (5.14), we find

$$\begin{aligned} \langle x, y, \sigma|T_x|X, k_y\rangle &= \langle x, y, \sigma + 1|X + 1, k_y\rangle, \\ \langle x, y, \sigma|T_y|X, k_y\rangle &= e^{-i2\pi(k_y/N_y + \sigma/C)} \langle x, y, \sigma|X, k_y\rangle. \end{aligned} \tag{5.110}$$

Since the clock-and-shift operators Q, P defined in Eq. (5.8) are unitary, we have

$$\langle\sigma|P = \langle\sigma - 1|, \quad \langle\sigma|Q = e^{i2\pi\sigma/C}\langle\sigma|. \tag{5.111}$$

Putting Eqs. (5.110) and (5.111) together, we find the action of $\widetilde{T}_x = T_x P$ and $\widetilde{T}_y = T_y Q$ to be particularly simple,

$$\langle x, y, \sigma | \widetilde{T}_x | X, k_y \rangle = \langle x, y, \sigma | X + 1, k_y \rangle, \quad \langle x, y, \sigma | \widetilde{T}_y | X, k_y \rangle = e^{-i2\pi k_y / N_y} \langle x, y, \sigma | X, k_y \rangle.$$

This proves Eq. (5.16).

5.B Projected density in Bloch basis

In this Appendix we prove Eq. (5.24), the expansion of the projected density operator in the Bloch basis.

We first derive a simpler form for the Bloch wave function $\phi_{\mathbf{k}}(\mathbf{r}, \sigma) = \langle \mathbf{r}, \sigma | \mathbf{k} \rangle$. When we plug Eq. (5.14) into Eq. (5.17), we have a double sum over X, m. However, notice that (X, m) in the double sum can always be combined into $X + mN_x$, thanks to $XN_y/C + mN_\phi = (X + mN_x)N_y/C$ and $e^{i2\pi X k_x/N_x} = e^{i2\pi(X+mN_x)k_x/N_x}$ (recall that $N_\phi = N_x N_y / C$). This enables us to merge the double sum into a single sum of $X + mN_x$ over $\mathbb{Z}$. The Kronecker-δ enforcing $\sigma = X + mN_x \bmod C$ suggests we split $X + mN_x \to nC + \sigma$ with n summed over $\mathbb{Z}$. This leads to the final form of the Bloch wave function,

$$\langle x, y, \sigma | \mathbf{k} \rangle = \frac{1}{(\sqrt{\pi} N_x L_y l_B)^{1/2}} \sum_n^{\mathbb{Z}} e^{i2\pi(nC+\sigma)k_x/N_x}$$
$$\exp\left\{ i2\pi \left(k_y + nN_y + \frac{\sigma}{C} N_y \right) \frac{y}{L_y} - \frac{1}{2} \left[\frac{x}{l_B} - \frac{2\pi l_B}{L_y} \left(k_y + nN_y + \frac{\sigma}{C} N_y \right) \right]^2 \right\}. \quad (5.112)$$

This wave function indeed depends only on $\sigma \bmod C$ (by a re-shift in the dummy variable n), and it has the quasi-periodicity in k_y as in Eq. (5.18). We now plug this

into $\rho_{\mathbf{q},\sigma}$ defined in Eq. (5.22).

$$\rho_{\mathbf{q},\sigma} = \frac{1}{\sqrt{\pi} N_x L_y l_B} \sum_{\mathbf{k}_1}^{\mathrm{BZ}} \sum_{\mathbf{k}_2}^{\mathrm{BZ}} |\mathbf{k}_1\rangle\langle\mathbf{k}_2| \sum_{n_1}^{\mathbb{Z}} \sum_{n_2}^{\mathbb{Z}} e^{-i2\pi(n_1 C+\sigma)k_{1x}/N_x} e^{i2\pi(n_2 C+\sigma)k_{2x}/N_x}$$
$$\Big[\int_0^{L_x} \mathrm{d}x\, e^{-i2\pi q_x x/L_x} \exp\Big\{ -\frac{1}{2}\Big[\frac{x}{l_B} - \frac{2\pi l_B}{L_y}\Big(k_{1y} + \frac{\sigma}{C}N_y + n_1 N_y\Big)\Big]^2$$
$$-\frac{1}{2}\Big[\frac{x}{l_B} - \frac{2\pi l_B}{L_y}\Big(k_{2y} + \frac{\sigma}{C}N_y + n_2 N_y\Big)\Big]^2 \Big\}\Big]$$
$$\Big[\int_0^{L_y} \mathrm{d}y\, e^{-i2\pi q_y y/L_y - i2\pi(k_{1y}+n_1 N_y - k_{2y} - n_2 N_y)y/L_y}\Big]. \quad (5.113)$$

We first finish the $\int \mathrm{d}y$ integral on the last line,

$$\int \mathrm{d}y\, e^{-i2\pi\cdots} = L_y\, \delta_{k_{2y}+n_2 N_y,\, k_{1y}+n_1 N_y+q_y}. \quad (5.114)$$

Notice that the summations of $\mathbf{k}_1$ and $\mathbf{k}_2$ over BZ in the above equation are independent. To accommodate the Kronecker-δ in the above equation, we set the summation of k_{1y} over $[0\ ..\ N_y)$, and the summation of k_{2y} over $[q_y\ ..\ N_y + q_y)$. Then, the Kronecker-δ above can be decomposed into two separate Kronecker-δ's, enforcing

$$k_{2y} = k_{1y} + q_y, \quad n_1 = n_2. \quad (5.115)$$

And we have

$$\rho_{\mathbf{q},\sigma} = \frac{1}{\sqrt{\pi} N_x l_B} \sum_{k_{1x}}^{N_x} \sum_{k_{2x}}^{N_x} \sum_{k_y}^{N_y} |k_{1x}, k_y\rangle\langle k_{2x}, k_y + q_y| \sum_{n}^{\mathbb{Z}} e^{i2\pi(nC+\sigma)(k_{2x}-k_{1x})/N_x}$$
$$\Big[\int_0^{L_x} \mathrm{d}x\, e^{-i2\pi q_x x/L_x} \exp\Big\{ -\frac{1}{2}\Big[\frac{x}{l_B} - \frac{2\pi l_B}{L_y}\Big(k_y + \frac{\sigma}{C}N_y + nN_y\Big)\Big]^2$$
$$-\frac{1}{2}\Big[\frac{x}{l_B} - \frac{2\pi l_B}{L_y}\Big(k_y + q_y + \frac{\sigma}{C}N_y + nN_y\Big)\Big]^2 \Big\}\Big]. \quad (5.116)$$

It is easy to check that $\rho_{\mathbf{q},\sigma}$ is indeed invariant under a shift of the dummy variable $k_y \to k_y + N_y$. We now tackle the $\int \mathrm{d}x$ integral in the bracket. We can collect terms and complete the square in the exponential. After some trivial but tedious algebra,

the integrand becomes

$$e^{-\mathbf{q}^2 l_B^2/4}\, e^{-i2\pi q_x(k_y+q_y/2+\sigma N_y/C+nN_y)/N_\phi}$$
$$\exp\left\{-\left[\frac{x}{l_B}-\frac{2\pi l_B}{L_y}\left(k_y+\frac{\sigma}{C}N_y+nN_y+\frac{1}{2}\left(q_y-i\frac{L_y}{L_x}q_x\right)\right)\right]^2\right\}. \quad (5.117)$$

Here we have used $2\pi l_B^2 N_\phi = L_x L_y$, and

$$\mathbf{q}^2 l_B^2 = \frac{2\pi}{N_\phi}\left(\frac{L_y}{L_x}q_x^2+\frac{L_x}{L_y}q_y^2\right). \quad (5.118)$$

The projected density can thus be written as

$$\rho_{\mathbf{q},\sigma} = \frac{1}{\sqrt{\pi}N_x l_B} e^{-\mathbf{q}^2 l_B^2/4} \sum_{k_{1x}}^{N_x}\sum_{k_{2x}}^{N_x}\sum_{k_y}^{N_y} |k_{1x},k_y\rangle\langle k_{2x},k_y+q_y|\, e^{-i2\pi q_x(k_y+q_y/2)/N_\phi}$$
$$\sum_n^{\mathbb{Z}} e^{i2\pi(nC+\sigma)(k_{2x}-k_{1x}-q_x)/N_x} \int_0^{L_x} \mathrm{d}x$$
$$\exp\left\{-\left[\frac{x}{l_B}-\frac{2\pi l_B}{L_y}\left(k_y+\frac{\sigma}{C}N_y+nN_y+\frac{1}{2}\left(q_y-i\frac{L_y}{L_x}q_x\right)\right)\right]^2\right\}. \quad (5.119)$$

Notice that

$$\frac{x}{l_B}-\frac{2\pi l_B}{L_y}nN_y = \frac{x-nN_yL_x/N_\phi}{l_B}; \quad (5.120)$$

we can shift the integration interval to

$$\int_{n\frac{N_y}{N_\phi}L_x}^{L_x+n\frac{N_y}{N_\phi}L_x} \mathrm{d}x. \quad (5.121)$$

This moves the dependence on n from the integrand to the integration limits (and also the exponential prefactor $e^{i2\pi(nC+\sigma)(k_{2x}-k_{1x}-q_x)/N_x}$).

We want to sew together the integrals for all n so that we can finish the Gaussian integral, but the integration intervals for different n are overlapping and cannot be joined head to tail in general, unless N_x is divisible by C. However, recall that (to have symmetries P, Q) we restrict the interacting Hamiltonian to be color-neutral, so we are interested only in $\rho_{\mathbf{q}} = \sum_\sigma^C \rho_{\mathbf{q},\sigma}$. The color sum saves us. Notice that the dependence on (σ, n) is all through the combination $nC+\sigma$. We can merge the two

sums over σ and n into a single sum over integers, $nC + \sigma \to m$:

$$\rho_{\mathbf{q}} = \frac{1}{\sqrt{\pi} N_x l_B} e^{-\mathbf{q}^2 l_B^2/4} \sum_{k_{1x}}^{N_x} \sum_{k_{2x}}^{N_x} \sum_{k_y}^{N_y} |k_{1x}, k_y\rangle\langle k_{2x}, k_y + q_y| \, e^{-i2\pi q_x (k_y + q_y/2)/N_\phi}$$
$$\sum_n^{\mathbb{Z}} e^{i2\pi n (k_{2x} - k_{1x} - q_x)/N_x} \int_0^{L_x} \mathrm{d}x$$
$$\exp\left\{ -\left[\frac{x}{l_B} - \frac{2\pi l_B}{L_y} \left(k_y + \frac{n}{C} N_y + \frac{1}{2} \left(q_y - i \frac{L_y}{L_x} q_x \right) \right) \right]^2 \right\}. \quad (5.122)$$

Notice that

$$\sum_n^{\mathbb{Z}} \cdots \int_0^{L_x} \mathrm{d}x \cdots = \sum_n^{\mathbb{Z}} e^{i2\pi n (k_{2x} - k_{1x} - q_x)/N_x} \int_{(n/N_x) L_x}^{(1+n/N_x) L_x} \mathrm{d}x$$
$$\exp\left\{ -\left[\frac{x}{l_B} - \frac{2\pi l_B}{L_y} \left(k_y + \frac{1}{2} \left(q_y - i \frac{L_y}{L_x} q_x \right) \right) \right]^2 \right\}. \quad (5.123)$$

Each interval $[\frac{m}{N_x} L_x, \frac{m+1}{N_x} L_x)$ is covered by the integral for N_x times, and during the N_x times, the exponential prefactor runs through all the N_x values of $e^{i2\pi t (k_{2x} - k_{1x} - q_x)}$ for $t \in [0 \,..\, N_x)$. In formula, we have

$$\sum_n^{\mathbb{Z}} \cdots \int \mathrm{d}x \cdots = \sum_n^{N_x} e^{i2\pi n (k_{2x} - k_{1x} - q_x)/N_x} \int_{-\infty}^{\infty} \mathrm{d}x$$
$$\exp\left\{ -\left[\frac{x}{l_B} - \frac{2\pi l_B}{L_y} \left(k_y + \frac{1}{2} \left(q_y - i \frac{L_y}{L_x} q_x \right) \right) \right]^2 \right\} \quad (5.124)$$
$$= \sqrt{\pi} N_x l_B \, \delta^{\mathrm{mod}\ N_x}_{k_{2x},\, k_{1x} + q_x}. \quad (5.125)$$

The "mod N_x" does not lead to any problem, since $|\mathbf{k}\rangle$ is periodic in k_x. Finally, we arrive at Eq. (5.24):

$$\rho_{\mathbf{q}} = e^{-\mathbf{q}^2 l_B^2/4} \sum_{\mathbf{k}}^{\mathrm{BZ}} e^{-i2\pi q_x (k_y + q_y/2)/N_\phi} \, |\mathbf{k}\rangle\langle \mathbf{k} + \mathbf{q}|.$$

5.C Pseudopotential Hamiltonian reorganized

In this Appendix we prove Eq. (5.65), the reorganized expression for the pseudopotential Hamiltonian in Eq. (5.63) suitable for truncation.

Starting from Eq. (5.63), we first isolate the q_x dependence,

$$H = \sum_{q_y}^{\mathbb{Z}} e^{-\frac{\pi}{N_\phi}\frac{L_x}{L_y}q_y^2} \sum_{j_1}^{M\prime} \sum_{j_2}^{M\prime} G_V(j_1 - j_2, q_y) \sum_{s_1}^{S_{j_1}} \sum_{s_2}^{S_{j_2}} \psi^\dagger_{j_1,s_1} \psi^\dagger_{j_2,s_2} \psi_{j_2 - q_y d, s_2} \psi_{j_1 + q_y d, s_1}, \quad (5.126)$$

where $G_V(j_1 - j_2, q_y)$ is defined by

$$G_V(k, q_y) = \sum_{q_x}^{\mathbb{Z}} \frac{V_{\mathbf{q}}}{2L_x L_y} \exp\left[-\frac{\pi}{N_\phi}\frac{L_y}{L_x} q_x^2 - i2\pi q_x \frac{k + q_y d}{M} \right]. \quad (5.127)$$

Through a Poisson resummation, we can easily prove the general formula

$$\sum_{q_x}^{\mathbb{Z}} e^{-\pi A q_x^2 - i2\pi q_x \xi} = \frac{1}{\sqrt{A}} \sum_{n}^{\mathbb{Z}} e^{-\pi(n-\xi)^2/A}. \quad (5.128)$$

Setting $A = L_y/(N_\phi L_x)$, $\xi = (k + q_y d)/M$, and defining

$$\beta = \frac{1}{d^2}\frac{\pi}{N_\phi}\frac{L_x}{L_y},$$

we get

$$\frac{1}{N_\phi} \sum_{q_x}^{\mathbb{Z}} \exp\left[-\frac{\pi}{N_\phi}\frac{L_y}{L_x} q_x^2 - i2\pi q_x \frac{k + q_y d}{M} \right] = \sqrt{\frac{L_x}{N_\phi L_y}} \sum_{n}^{\mathbb{Z}} e^{-\beta(k + q_y d - nM)^2}. \quad (5.129)$$

To handle $G_V(k, q_y)$ in Eq. (5.127), we need to be able to insert powers of q_x^2 into the q_x sum. This can be achieved by taking partial derivative with respect to $\frac{\pi L_y}{N_\phi L_x} = \beta d^2$ on Eq. (5.129). For the simple case of $V_{\mathbf{q}} = 4\pi l_B^2 [V_0 + V_1 \cdot (1 - \mathbf{q}^2 l_B^2)]$ as in Eq. (5.61), we find

$$G_V(k, q_y) = \sqrt{\frac{L_x}{N_\phi L_y}} \sum_{n}^{\mathbb{Z}} e^{-\beta(k + q_y d - nM)^2} \left\{ V_0 + 2\beta V_1 \left[(k + q_y d - nM)^2 - (q_y d)^2 \right] \right\}. \quad (5.130)$$

Plugging this back to Eq. (5.126), we get

$$H = C \sum_{q_y}^{\mathbb{Z}} e^{-\beta(q_y d)^2} \sum_{j_1}^{M\,\prime} \sum_{j_2}^{M\,\prime} \sum_{n}^{\mathbb{Z}} e^{-\beta(j_1 - j_2 + q_y d - nM)^2} \Big\{ V_0 + 2\beta V_1 \left[(j_1 - j_2 + q_y d - nM)^2 - (q_y d)^2 \right] \Big\} \sum_{s_1}^{S_{j_1}} \sum_{s_2}^{S_{j_2}} \psi^\dagger_{j_1,s_1} \psi^\dagger_{j_2,s_2} \psi_{j_2 - q_y d, s_2} \psi_{j_1 + q_y d, s_1}, \quad (5.131)$$

where $C = \sqrt{L_x/(N_\phi L_y)}$ is an inconsequential overall factor.

At last, recall from Eq. (5.59) that the range of summations over j_1 and j_2 each contain an arbitrary shift. We can keep the outer sum over j_1 general, while make a convenient choice for the inner sum over j_2. We define $\Delta = j_2 - j_1$ and rewrite the above equation as

$$H = C \sum_{q_y}^{\mathbb{Z}} e^{-\beta(q_y d)^2} \sum_{j}^{M\,\prime} \sum_{\Delta} \sum_{n}^{\mathbb{Z}} e^{-\beta(\Delta - q_y d + nM)^2} \Big\{ V_0 + 2\beta V_1 \left[(\Delta - q_y d + nM)^2 - (q_y d)^2 \right] \Big\} \sum_{s}^{S_j} \sum_{s'}^{S_{j+\Delta}} \psi^\dagger_{j,s} \psi^\dagger_{j+\Delta,s'} \psi_{j+\Delta - q_y d, s'} \psi_{j + q_y d, s}, \quad (5.132)$$

where Δ is summed over an interval of length M centered around $q_y d$,

$$\Delta \in \big[\, q_y d - \lfloor M/2 \rfloor \,..\, q_y d - \lfloor M/2 \rfloor + M \,\big). \quad (5.133)$$

We make this special choice for the Δ sum to facilitate later truncations in the thin-torus limit $\beta \gg 1$. This proves Eq. (5.65).

Bibliography

[1] E. Ardonne, J. Gukelberger, A. W. W. Ludwig, S. Trebst, and M. Troyer. Microscopic models of interacting Yang-Lee anyons. *New Journal of Physics*, 13:045006, 2011.

[2] E. Ardonne and N. Regnault. Structure of spinful quantum Hall states: A squeezing perspective. *Physical Review B*, 84(20):205134, 2011.

[3] E. Ardonne and K. Schoutens. Wavefunctions for topological quantum registers. *Annals of Physics*, 322(1):201–235, 2007.

[4] Eddy Ardonne and Kareljan Schoutens. New Class of Non-Abelian Spin-Singlet Quantum Hall States. *Phys. Rev. Lett.*, 82(25):5096–5099, 1999.

[5] Daniel Arovas, J. R. Schrieffer, and Frank Wilczek. Fractional Statistics and the Quantum Hall Effect. *Phys. Rev. Lett.*, 53(7):722–723, 1984.

[6] M. Baraban, G. Zikos, N. Bonesteel, and S. H. Simon. Numerical Analysis of Quasiholes of the Moore-Read Wave Function. *Phys. Rev. Lett.*, 103(7):076801, 2009.

[7] Maissam Barkeshli and Xiao-Liang Qi. Topological Nematic States and Non-Abelian Lattice Dislocations. *Physical Review X*, 2(3):031013, 2012.

[8] A. A. Belavin, A. M. Polyakov, and A. B. Zamolodchikov. Infinite conformal symmetry in two-dimensional quantum field theory. *Nuclear Physics B*, 241(2):333–380, 1984.

[9] E. J. Bergholtz and A. Karlhede. 'One-dimensional' theory of the quantum Hall system. *Journal of Statistical Mechanics: Theory and Experiment*, 4:L04001, 2006.

[10] E. J. Bergholtz and A. Karlhede. Quantum Hall system in Tao-Thouless limit. *Physical Review B*, 77(15):155308, 2008.

[11] Emil J. Bergholtz and Anders Karlhede. Half-Filled Lowest Landau Level on a Thin Torus. *Phys. Rev. Lett.*, 94(2):026802, 2005.

[12] B. A. Bernevig and F. D. M. Haldane. Model Fractional Quantum Hall States and Jack Polynomials. *Physical Review Letters*, 100(24):246802, 2008.

[13] B. A. Bernevig and F. D. M. Haldane. Properties of Non-Abelian Fractional Quantum Hall States at Filling ν=k/r. *Physical Review Letters*, 101(24):246806, 2008.

[14] B. A. Bernevig and N. Regnault. Thin-Torus Limit of Fractional Topological Insulators. *ArXiv e-prints*, 2012.

[15] B Andrei Bernevig, Taylor L Hughes, and Shou-Cheng Zhang. Quantum spin Hall effect and topological phase transition in HgTe quantum wells. *Science*, 314(5806):1757–61, 2006.

[16] B. Andrei Bernevig and N. Regnault. Emergent many-body translational symmetries of Abelian and non-Abelian fractionally filled topological insulators. *Physical Review B*, 85(7):075128, 2012.

[17] Parsa Bonderson. Splitting the Topological Degeneracy of Non-Abelian Anyons. *Phys. Rev. Lett.*, 103(11):110403, 2009.

[18] Parsa Bonderson, Victor Gurarie, and Chetan Nayak. Plasma analogy and non-Abelian statistics for Ising-type quantum Hall states. *Physical Review B*, 83(7):075303, 2011.

[19] Parsa Bonderson, Kirill Shtengel, and J. K. Slingerland. Probing Non-Abelian Statistics with Quasiparticle Interferometry. *Phys. Rev. Lett.*, 97(1):016401, 2006.

[20] Anushya Chandran, M. Hermanns, N. Regnault, and B. Andrei Bernevig. Bulk-edge correspondence in entanglement spectra. *Phys. Rev. B*, 84(20):205136, 2011.

[21] Meng Cheng, Roman M. Lutchyn, Victor Galitski, and S. Das Sarma. Splitting of Majorana-Fermion Modes due to Intervortex Tunneling in a $p_x + ip_y$ Superconductor. *Phys. Rev. Lett.*, 103(10):107001, 2009.

[22] Sankar Das Sarma, Michael Freedman, and Chetan Nayak. Topologically Protected Qubits from a Possible Non-Abelian Fractional Quantum Hall State. *Phys. Rev. Lett.*, 94(16):166802, 2005.

[23] Philippe Di Francesco, Pierre Mathieu, and David Sénéchal. *Conformal Field Theory*. Springer, 1999.

[24] J. Dubail, N. Read, and E. H. Rezayi. Edge-state inner products and real-space entanglement spectrum of trial quantum Hall states. *Physical Review B*, 86(24):245310, 2012.

[25] J. Eisert, M. Cramer, and M. B. Plenio. Area laws for the entanglement entropy. *Rev. Mod. Phys.*, 82(1):277–306, 2010.

[26] B. Estienne, Z. Papic, N. Regnault, and B. A.g Bernevig. Matrix product states for trial quantum Hall states. *Physical Review B*, 87(16):161112, 2013.

[27] B. Estienne, N. Regnault, and B. A. Bernevig. Fractional Quantum Hall Matrix Product States For Interacting Conformal Field Theories. *ArXiv e-prints*, 2013.

[28] Benoit Estienne and B. Andrei Bernevig. Spin-singlet quantum Hall states and Jack polynomials with a prescribed symmetry. *Nuclear Physics B*, 857(2):185, 2012.

[29] M. Fannes, B. Nachtergaele, and R. F. Werner. Finitely correlated states on quantum spin chains. *Communications in Mathematical Physics*, 144(3):443–490, 1992.

[30] Michael H. Freedman, Michael Larsen, and Zhenghan Wang. A Modular Functor Which is Universal for Quantum Computation. *Communications in Mathematical Physics*, 227(3):605–622, 2002.

[31] Michael H. Freedman, Michael J. Larsen, and Zhenghan Wang. The Two-Eigenvalue Problem and Density of Jones Representation of Braid Groups. *Communications in Mathematical Physics*, 228(1):177–199, 2002.

[32] Sergio Fubini. Vertex operators and quantum Hall effect. *Modern Physics Letters A*, 06(04):347–358, 1991.

[33] S. M. Girvin, A. H. MacDonald, and P. M. Platzman. Magneto-roton theory of collective excitations in the fractional quantum Hall effect. *Physical Review B*, 33(4):2481–2494, 1986.

[34] M. O. Goerbig. From fractional Chern insulators to a fractional quantum spin hall effect. *The European Physical Journal B*, 85(1):15, 2012.

[35] Martin Greiter, Xiao-Gang Wen, and Frank Wilczek. Paired Hall state at half filling. *Physical Review Letters*, 66(24):3205–3208, 1991.

[36] Adolfo G. Grushin, Titus Neupert, Claudio Chamon, and Christopher Mudry. Enhancing the stability of a fractional Chern insulator against competing phases. *Physical Review B*, 86(20):205125, 2012.

[37] Victor Gurarie and Chetan Nayak. A plasma analogy and Berry matrices for non-abelian quantum Hall states. *Nuclear Physics B*, 506(3):685–694, 1997.

[38] F. D. M. Haldane. Fractional Quantization of the Hall Effect: A Hierarchy of Incompressible Quantum Fluid States. *Phys. Rev. Lett.*, 51(7):605–608, 1983.

[39] F. D. M. Haldane. Many-Particle Translational Symmetries of Two-Dimensional Electrons at Rational Landau-Level Filling. *Phys. Rev. Lett.*, 55(20):2095–2098, 1985.

[40] F. D. M. Haldane. Model for a Quantum Hall Effect without Landau Levels: Condensed-Matter Realization of the "Parity Anomaly". *Physical Review Letters*, 61(18):2015–2018, 1988.

[41] B. I. Halperin. Theory of the quantized Hall conductance. *Helv. Phys. Acta*, 56:75–102, 1983.

[42] Masudul Haque, O S Zozulya, and K Schoutens. Entanglement between particle partitions in itinerant many-particle states. *Journal of Physics A: Mathematical and Theoretical*, 42(50):504012, 2009.

[43] Masudul Haque, Oleksandr Zozulya, and Kareljan Schoutens. Entanglement Entropy in Fermionic Laughlin States. *Physical Review Letters*, 98(6):060401, 2007.

[44] L. Hormozi, G. Zikos, N. E. Bonesteel, and S. H. Simon. Topological quantum compiling. *Phys. Rev. B*, 75(16):165310, 2007.

[45] Xiang Hu, Mehdi Kargarian, and Gregory A. Fiete. Topological insulators and fractional quantum Hall effect on the ruby lattice. *Physical Review B*, 84(15):155116, 2011.

[46] Sonika Johri, Z. Papić, R. N. Bhatt, and P. Schmitteckert. Quasiholes of $\frac{1}{3}$ and $\frac{7}{3}$ quantum Hall states: Size estimates via exact diagonalization and density-matrix renormalization group. *Phys. Rev. B*, 89(11):115124, 2014.

[47] A. Yu. Kitaev. Fault-tolerant quantum computation by anyons. *Annals of Physics*, 303(1):2–30, 2003.

[48] Alexei Kitaev. Anyons in an exactly solved model and beyond. *Annals of Physics*, 321(1):2–111, 2006.

[49] S. Kivelson. Wannier functions in one-dimensional disordered systems: Application to fractionally charged solitons. *Physical Review B*, 26(8):4269–4277, 1982.

[50] A. Kol and N. Read. Fractional quantum Hall effect in a periodic potential. *Phys. Rev. B*, 48(12):8890–8898, 1993.

[51] A. M. Läuchli, Zhao Liu, E. J. Bergholtz, and R. Moessner. Hierarchy of Fractional Chern Insulators and Competing Compressible States. *Phys. Rev. Lett.*, 111(12):126802, 2013.

[52] R. B. Laughlin. Anomalous Quantum Hall Effect: An Incompressible Quantum Fluid with Fractionally Charged Excitations. *Physical Review Letters*, 50(18):1395–1398, 1983.

[53] Hui Li and F. D. M. Haldane. Entanglement Spectrum as a Generalization of Entanglement Entropy: Identification of Topological Order in Non-Abelian Fractional Quantum Hall Effect States. *Physical Review Letters*, 101(1):010504, 2008.

[54] Zhao Liu and Emil J. Bergholtz. From fractional Chern insulators to Abelian and non-Abelian fractional quantum Hall states: Adiabatic continuity and orbital entanglement spectrum. *Physical Review B*, 87(3):035306, 2013.

[55] Zhao Liu, Emil J. Bergholtz, Heng Fan, and Andreas M. Läuchli. Fractional Chern Insulators in Topological Flat Bands with Higher Chern Number. *Physical Review Letters*, 109(18):186805, 2012.

[56] Yuan-Ming Lu and Ying Ran. Symmetry-protected fractional Chern insulators and fractional topological insulators. *Physical Review B*, 85(16):165134, 2012.

[57] Nicola Marzari and David Vanderbilt. Maximally localized generalized Wannier functions for composite energy bands. *Physical Review B*, 56(20):12847, 1997.

[58] John McGreevy, Brian Swingle, and Ky-Anh Tran. Wave functions for fractional Chern insulators. *Physical Review B*, 85(12):125105, 2012.

[59] G. Möller and N. R. Cooper. Composite Fermion Theory for Bosonic Quantum Hall States on Lattices. *Physical Review Letters*, 103(10):105303, 2009.

[60] Gregory Moore and Nicholas Read. Nonabelions in the fractional quantum hall effect. *Nuclear Physics B*, 360(2-3):362–396, 1991.

[61] Gregory Moore and Nathan Seiberg. Classical and quantum conformal field theory. *Communications in Mathematical Physics*, 123(2):177–254, 1989.

[62] G. Murthy and R. Shankar. Composite Fermions for Fractionally Filled Chern Bands. *ArXiv e-prints*, 2011.

[63] Chetan Nayak, Ady Stern, Michael Freedman, and Sankar Das Sarma. Non-Abelian anyons and topological quantum computation. *Reviews of Modern Physics*, 80(3):1083, 2008.

[64] Chetan Nayak and Frank Wilczek. $2n$-quasihole states realize $2n-1$-dimensional spinor braiding statistics in paired quantum Hall states. *Nuclear Physics B*, 479(3):529–553, 1996.

[65] Titus Neupert, Luiz Santos, Claudio Chamon, and Christopher Mudry. Fractional Quantum Hall States at Zero Magnetic Field. *Physical Review Letters*, 106(23):236804, 2011.

[66] W. Pan, J. S. Xia, V. Shvarts, D. E. Adams, H. L. Stormer, D. C. Tsui, L. N. Pfeiffer, K. W. Baldwin, and K. W. West. Exact Quantization of the Even-Denominator Fractional Quantum Hall State at $\nu = 5/2$ Landau Level Filling Factor. *Phys. Rev. Lett.*, 83(17):3530–3533, 1999.

[67] Zlatko Papic, Nicolas Regnault, and B. Andrei Bernevig. in preparation.

[68] S. A. Parameswaran, R. Roy, and S. L. Sondhi. Fractional Chern insulators and the W_∞ algebra. *Physical Review B*, 85(24):241308, 2012.

[69] D. Podolsky and J. Avron. private communication.

[70] Emil Prodan and F. D. M. Haldane. Mapping the braiding properties of the Moore-Read state. *Physical Review B*, 80(11):115121, 2009.

[71] Xiao-Liang Qi. Generic Wave-Function Description of Fractional Quantum Anomalous Hall States and Fractional Topological Insulators. *Physical Review Letters*, 107(12):126803, 2011.

[72] N. Read. Non-Abelian adiabatic statistics and Hall viscosity in quantum Hall states and $p_x + ip_y$ paired superfluids. *Phys. Rev. B*, 79(4):045308, 2009.

[73] N. Read and E. Rezayi. Beyond paired quantum Hall states: Parafermions and incompressible states in the first excited Landau level. *Physical Review B*, 59(12):8084–8092, 1999.

[74] N. Regnault and B. Andrei Bernevig. Fractional Chern Insulator. *Phys. Rev. X*, 1(2):021014, 2011.

[75] N. Regnault, B. Andrei Bernevig, and F. D. M. Haldane. Topological Entanglement and Clustering of Jain Hierarchy States. *Physical Review Letters*, 103(1):016801, 2009.

[76] B. Rosenow and Steven H. Simon. Telegraph noise and the Fabry-Perot quantum Hall interferometer. *Phys. Rev. B*, 85(20):201302, 2012.

[77] Thomas Scaffidi and Gunnar Möller. Adiabatic Continuation of Fractional Chern Insulators to Fractional Quantum Hall States. *Physical Review Letters*, 109(24):246805, 2012.

[78] Ulrich Schollwöck. The density-matrix renormalization group in the age of matrix product states. *Annals of Physics*, 326(1):96, 2011.

[79] Alexander Seidel and Dung-Hai Lee. Abelian and Non-Abelian Hall Liquids and Charge-Density Wave: Quantum Number Fractionalization in One and Two Dimensions. *Phys. Rev. Lett.*, 97(5):056804, 2006.

[80] D N Sheng, Zheng-Cheng Gu, Kai Sun, and L Sheng. Fractional quantum Hall effect in the absence of Landau levels. *Nature Communications*, 2:389, 2011.

[81] Steven H. Simon, E. H. Rezayi, N. R. Cooper, and I. Berdnikov. Construction of a paired wave function for spinless electrons at filling fraction ν=2/5. *Physical Review B*, 75(7):075317, 2007.

[82] Steven H. Simon, E. H. Rezayi, and Nigel R. Cooper. Pseudopotentials for multiparticle interactions in the quantum Hall regime. *Physical Review B*, 75(19):195306, 2007.

[83] A. Sterdyniak, N. Regnault, and B. A. Bernevig. Extracting Excitations from Model State Entanglement. *Physical Review Letters*, 106(10):100405, 2011.

[84] A. Sterdyniak, C. Repellin, B. Andrei Bernevig, and N. Regnault. Series of Abelian and non-Abelian states in $C > 1$ fractional Chern insulators. *Phys. Rev. B*, 87(20):205137, 2013.

[85] Ady Stern and Bertrand I. Halperin. Proposed Experiments to Probe the Non-Abelian $\nu = 5/2$ Quantum Hall State. *Phys. Rev. Lett.*, 96(1):016802, 2006.

[86] M. Storni and R. H. Morf. Localized quasiholes and the Majorana fermion in fractional quantum Hall state at $\nu = \frac{5}{2}$ via direct diagonalization. *Phys. Rev. B*, 83(19):195306, 2011.

[87] Kai Sun, Zhengcheng Gu, Hosho Katsura, and S. Das Sarma. Nearly Flatbands with Nontrivial Topology. *Physical Review Letters*, 106(23):236803, 2011.

[88] Evelyn Tang, Jia-Wei Mei, and Xiao-Gang Wen. High-Temperature Fractional Quantum Hall States. *Physical Review Letters*, 106(23):236802, 2011.

[89] R. Tao and D. J. Thouless. Fractional quantization of Hall conductance. *Phys. Rev. B*, 28(2):1142–1144, 1983.

[90] Maximilian Trescher and Emil J. Bergholtz. Flat bands with higher Chern number in pyrochlore slabs. *Physical Review B*, 86(24):241111, 2012.

[91] Yaroslav Tserkovnyak and Steven H. Simon. Monte Carlo Evaluation of Non-Abelian Statistics. *Phys. Rev. Lett.*, 90(1):016802, 2003.

[92] D. C. Tsui, H. L. Stormer, and A. C. Gossard. Two-Dimensional Magnetotransport in the Extreme Quantum Limit. *Phys. Rev. Lett.*, 48(22):1559–1562, 1982.

[93] A. Vaezi. Fractional quantum Hall effect at zero magnetic field. *ArXiv e-prints*, 2011.

[94] Yi-Fei Wang, Zheng-Cheng Gu, Chang-De Gong, and D. N. Sheng. Fractional Quantum Hall Effect of Hard-Core Bosons in Topological Flat Bands. *Physical Review Letters*, 107(14):146803, 2011.

[95] Yi-Fei Wang, Hong Yao, Chang-De Gong, and D. N. Sheng. Fractional quantum Hall effect in topological flat bands with Chern number two. *Physical Review B*, 86(20):201101, 2012.

[96] Yi-Fei Wang, Hong Yao, Zheng-Cheng Gu, Chang-De Gong, and D. N. Sheng. Non-Abelian Quantum Hall Effect in Topological Flat Bands. *Physical Review Letters*, 108(12):126805, 2012.

[97] R. Willett, J. P. Eisenstein, H. L. Störmer, D. C. Tsui, A. C. Gossard, and J. H. English. Observation of an even-denominator quantum number in the fractional quantum Hall effect. *Phys. Rev. Lett.*, 59(15):1776–1779, 1987.

[98] Y. L. Wu, B. Estienne, N. Regnault, and B. A. Bernevig. Braiding non-Abelian quasiholes in fractional quantum Hall states. *ArXiv e-prints*, 2014.

[99] Yang-Le Wu, B. Andrei Bernevig, and N. Regnault. Zoology of fractional Chern insulators. *Physical Review B*, 85(7):075116, 2012.

[100] Yang-Le Wu, N. Regnault, and B. Andrei Bernevig. Gauge-fixed Wannier wave functions for fractional topological insulators. *Physical Review B*, 86(8):085129, 2012.

[101] Yang-Le Wu, N. Regnault, and B. Andrei Bernevig. Bloch Model Wave Functions and Pseudopotentials for All Fractional Chern Insulators. *Physical Review Letters*, 110(10):106802, 2013.

[102] Yang-Le Wu, N. Regnault, and B. Andrei Bernevig. Haldane statistics for fractional Chern insulators with an arbitrary Chern number. *Phys. Rev. B*, 89(15):155113, 2014.

[103] J. S. Xia, W. Pan, C. L. Vicente, E. D. Adams, N. S. Sullivan, H. L. Stormer, D. C. Tsui, L. N. Pfeiffer, K. W. Baldwin, and K. W. West. Electron Correlation in the Second Landau Level: A Competition Between Many Nearly Degenerate Quantum Phases. *Phys. Rev. Lett.*, 93(17):176809, 2004.

[104] Shuo Yang, Zheng-Cheng Gu, Kai Sun, and S. Das Sarma. Topological flat band models with arbitrary Chern numbers. *Physical Review B*, 86(24):241112, 2012.

[105] Rui Yu, Xiao Liang Qi, Andrei Bernevig, Zhong Fang, and Xi Dai. Equivalent expression of Z_2 topological invariant for band insulators using the non-Abelian Berry connection. *Physical Review B*, 84(7):075119, 2011.

[106] V. P. Yurov and Al. B. Zamolodchikov. Truncated conformal space approach to scaling Lee-Yang model. *International Journal of Modern Physics A*, 05(16):3221–3245, 1990.

[107] Michael P. Zaletel and Roger S. K. Mong. Exact matrix product states for quantum Hall wave functions. *Physical Review B*, 86:245305, 2012.

[108] O. S. Zozulya, M. Haque, K. Schoutens, and E. H. Rezayi. Bipartite entanglement entropy in fractional quantum Hall states. *Physical Review B*, 76(12):125310, 2007.